BIOMEDICAL INSTRUMENTATION AND NANOTECHNOLOGY FOR IMAGE-GUIDED CANCER SURGERY

A Dissertation
Presented to
The Academic Faculty

by

Michael C. Mancini

In Partial Fulfillment
of the Requirements for the Degree
Doctor of Philosophy in the
Wallace H. Coulter Department of Biomedical Engineering

Georgia Institute of Technology
Emory University
May 2011

BIOMEDICAL INSTRUMENTATION AND NANOTECHNOLOGY FOR IMAGE-GUIDED CANCER SURGERY

Approved by:

Shuming Nie, Advisor
School of Biomedical Engineering
Georgia Institute of Technology and Emory University

Mostafa El-Sayed
School of Chemistry
Georgia Institute of Technology

James M. Provenzale
School of Medicine
Duke University and Emory University

Philip J. Santangelo
School of Biomedical Engineering
Georgia Institute of Technology and Emory University

W. Robert Taylor
School of Biomedical Engineering
Georgia Institute of Technology and Emory University

Date Approved: 3 March 2011

ACKNOWLEDGEMENTS

Sir Isaac Newton is famously remembered for, in a letter to his contemporary and sometimes rival Robert Hooke, writing "If I have seen a little further it is by standing on the shoulders of Giants." If I have succeeded in my time as a graduate student, it is only because of the immense support and assistance I have received throughout my graduate career.

First and foremost, I acknowledge and thank my advisor, Prof. Nie. He was the right advisor for me, at the right time in my academic career. When I first met him, he told me that he gives his students "the freedom to succeed and the freedom to fail." I didn't know much at the time, but I did know that I wanted to be able to make my own mistakes and work through them. Through success comes knowledge, through failures comes wisdom. Prof. Nie's love of academics and the academic process is plainly obvious to anyone who knows him, and it's reflected in the personal interest he invests in seeing his students succeed. I would also like to thank my committee for their participation in my graduate studies. I am grateful for their suggestions, criticisms, and guidance. Dr. Provenzale has been especially influential in my graduate career. Without the collaborations that he set up, this dissertation would look substantially different than it does now. I've learned quite a bit about human medicine from him, and through his collaborators, some about canine medicine too. Beyond research, I was a teaching assistant for Prof. Barbara Boyan for two years: I learned an incredible amount about teaching and interacting with students from her. Credit must also be given Profs. Michael King and Keigi Fujiwara, whose labs I worked in as an undergraduate student at the University of Rochester. I don't know that I would have pursued a graduate education if I had not had a wonderful experience working in their labs.

I am grateful for the many fellow graduate students and post-doctoral researchers with

whom I have collaborated and worked alongside. Matt Rhyner must be credited for recruiting me into the lab. He gave me two pieces of advice that to this day serve me well: "measure twice, cut once" and "always print a small poster." Amit Agrawal got me started in lab and helped acclimate me to the research environment. Brad Kairdolf and Andrew Smith are my partners in crime—we've published several manuscripts together, and I have learned quite a bit from both of them. Aaron Mohs and I have worked together quite a bit on intraoperative imaging, and without him, the intraoperative imaging project would not be where it is now. I have had many enjoyable conversations with Ximei Qian and Steven Emory, and I'm not sure that I could count the number of ideas that have sprung from my interactions with them. Kate Lee and Anthony Nicolini are both my classmates and friends, and we have supported each other throughout the graduate school process. If one ever hears a loud screeching sound emanating from the Emory campus, that would be the sound of the lab screeching to a halt because Michelle Denney and Cynthia Lewis-Webb aren't around to keep things running. No science can happen without their tireless efforts. Much credit must also be given to Ryan Jowers who kept the trains running on time for many years.

I think this dissertation (and my graduate student career) is greatly enhanced by an incredible collaboration with the University of Georgia College of Veterinary Medicine, started with Dr. Provenzale's efforts and through his recognition of the importance of comparative oncology. This is not a collaboration of one or two people but of an entire team: Drs. Corey Saba, Elizabeth Howerth, Karen Cornell, Chad Schmiedt and MaryAnn Radlinsky. I am lucky for having the opportunity to work with them, but their patients are even more fortunate to have such a skilled and caring team to look after them.

Last, I must thank my friends and family. The friendships I've made while in Atlanta have been wonderful and I'm so glad to have met everyone—I hope we continue to stay in touch. My father has a keen scientific mind that has been inspirational, and my mother, a pediatrician, has obviously had a clear influence on my scientific interest in medicine. Both got me started on this path, and it was through the love and support from my parents,

my sister Sarah, my half brother Dan, and my half sister Holly and her family that I have finished. I don't know what the future will bring, but I am grateful that my friends and family will be there with me.

TABLE OF CONTENTS

LIST OF TABLES

LIST OF FIGURES

LIST OF SYMBOLS OR ABBREVIATIONS

ABAH	4-aminobenzoic acid hydrazide.
API	application programming interface.
AUC	area under the curve.
BAEC	bovine aorta endothelial cell.
BSA	bovine serum albumin.
Bt	*Bos taurus* (bovine, cow).
Cat	catalase.
CCD	charge-coupled device.
Cd	cadmium.
·NO	nitric oxide.
·OH	hydroxyl radical.
$\cdot O_2^-$	superoxide.
CdS	cadmium sulfide.
CdSe	cadmium selenide.
CdSe/ZnS	cadmium selenide (core), zinc sulfide (shell).
CdTe	cadmium telluride.
CK18	cytokeratin-18.
Cl^-	chloride.
CV	Coefficient of variation.
CW	continuous wave.
DLS	dynamic light scattering.
DMEM	Dulbecco's modified Eagle's medium.
DMSO	dimethylsulfoxide.
DPPC	1,2-dipalmitoyl-glycero-3-phosphocholine.
DPPE-PEG	1,2-dipalmitoyl-*sn*-glycero-3-phospho -ethanolamine-*N*-methoxy(polyethylene-glycol)-2000.

DTTC	3-ethyl-2-[7-(3-ethyl-2(3H)-benzo -thiazolylidene)-1,3,5- heptatrienyl]-benzothiazolium iodide.
EM	electron microscopy.
FBS	fetal bovine serum.
FD	frequency domain.
FDA	Food and Drug Administration.
FITC	fluorescein isothiocyanate.
GSH	glutathione.
HeCd	helium cadmium.
HFO	hypofluorous acid.
HOBr	hypobromous acid.
HOCl	hypochlorous acid.
HOI	hypoiodous acid.
H_2O_2	hydrogen peroxide.
ICG	indocyanine green.
ICP-MS	inductively-coupled plasma mass spectrometry.
IHC	immunohistochemistry.
IMDM	Isocove's modification of Dulbecco's modified Eagle's medium.
LED	light-emitting diode.
LPS	lipopolysaccharides.
LSPR	localized surface plasmon resonance.
MAA	mercaptoacetic acid.
$(Me)_2Cd$	dimethylcadmium.
MgF_2	magnesium fluoride.
MPA	mercaptopropionic acid.
MPS	mononuclear phagocyte system.

MR	magnetic resonance.
NIR	near-infrared.
$ONOO^-$	peroxynitrite.
O_2	molecular oxygen.
PAA-*g*-DDA	polyacrylic acid *graft* dodecylamine.
PBS	phosphate-buffered saline.
PEG	polyethylene glycol.
PEG-SH	polyethylene glycol, thiol-terminated.
PEI	polyethyleneimine.
PEI-*g*-PEG	polyethyleneimine *graft* polyethylene glycol.
QD	semiconductor quantum dot.
QE	quantum efficiency.
QY	quantum yield.
ROC	receiver-operator characteristic.
S	sulfur.
Se	selenium.
SERS	surface-enhanced Raman scattering.
SHE	standard hydrogen electrode.
Si	silicon.
TD	time domain.
TOP	trioctylphosphine.
TOPO	trioctylphosphine oxide.
UGA-CVM	University of Georgia, College of Veterinary Medicine.
UV-vis	ultraviolet-visible.
VP	virtual phosphorescence.
Xe	xenon.
Zn	zinc.
ZnS	zinc sulfide.

SUMMARY

Once diagnosed, cancer is treated by surgical resection, chemotherapy, radiation therapy, or a combination of these therapies. It is intuitive that physically and completely removing a solid tumor would be an effective treatment. A complete resection of the tumor mass, defined by surgical margins that are clear of neoplasia, is prognostic for a decreased chance of cancer recurrence and an increased survival rate. In practice, complete resection is difficult. A surgeon primarily has only their senses of touch and sight to provide "real-time" guidance in the removal of a tumor while in the operating room. Preoperative imaging can guide a surgeon to a tumor but does not give a continuous update of surgical progress. Intraoperative pathology is limited to a few slides worth of samples: a product of its time-consuming nature and the limited time a patient can remain under general anesthesia. Technologies to guide a surgeon in effecting complete resection of a tumor mass during the surgical procedure would greatly increase cancer survival rates by lowering rates of cancer recurrence; such a technology would also reduce the need for follow-up chemotherapy or radiation therapy. Here, we describe a prototype instrumentation system that can provide intraoperative guidance with exogenous optical contrast agents. The instrumentation combines interactive point excitation, local spectroscopy, and widefield fluorescence imaging to enable low-cost surgical guidance using FDA-approved fluorescent dyes, semiconductor quantum dots (QDs), or surface-enhanced Raman scattering (SERS) nanoparticles. The utility of this surgical system is demonstrated in rodent tumor models using an FDA-approved fluorescent dye, indocyanine green (ICG), and is then more extensively demonstrated with a pre-clinical study of spontaneous tumors in companion canines. The pre-clinical studies show a high sensitivity in detecting a variety of canine tumors with a low false positive rate, as verified by pathology.

We also present a fundamental study on the behavior of quantum dots. QDs are a promising fluorophore for biological applications, including as a surgical contrast agent. To use QDs for *in vivo* human imaging, toxicity concerns must be addressed first. Although it is suspected that QDs may be toxic to an organism based on the heavy-metal elemental composition of QDs, overt organism toxicity is not seen in long-term animal model studies. We have found that some reactive oxygen species (ROS) generated by the host inflammatory response can rapidly degrade QDs; in the case of hypochlorous acid, optical changes to the QDs are suggestive of degradation occurring within seconds. It is well-known that QDs are sequestered by the immune system when used *in vivo*—we therefore believe that QD degradation through an inflammatory response may represent a realizable in vivo mechanism for QD degradation. We demonstrate in an *in vitro* cell culture model that immune cells can degrade QDs through ROS exposure. Knowledge of the degradative processes that QDs would be subject to when used *in vivo* informs on adaptations that can be made to the QDs to resist degradation. Such adaptations will be important in developing QD-based contrast agents for image guided surgery.

CHAPTER I

OPPORTUNITIES FOR IMPROVING CANCER THERAPY

1.1 Abstract

President Richard M. Nixon began the "War on Cancer" by signing the National Cancer Act of 1971. From this act sprang a considerable scientific effort to eradicate cancer. Despite scientific and medical efforts, the mortality rate attributed to cancer is largely unchanged over the last 50 years. Cancer is a complex and varied disease, and difficult to treat through drugs or radiation alone. Surgery is an effective treatment, but surgical technique has not changed since the beginnings of surgical oncology. Recent advancements in nanotechnology, the manipulation of materials and structures on the 1–100 nm scale, offer new tools for cancer research, diagnosis, and treatment.

1.2 Introduction

Every year, the American Cancer Society compiles and publishes a comprehensive statistical analysis describing the current state of cancer within the United States, drawing from numerous sources.[121] In 2010, 1.5 million patients in the U.S. were newly diagnosed with cancer. Forty-thousand of these patients lived in Georgia. In addition to these new cases, there are 11 million estimated people in the U.S. who have or have had cancer. Between 1975–1977, the 5 year relative survival rate for cancer was 50%. In 2005–2007, this 5 year relative survival rate increased to 68%. It is important to note that the relative survival rate compares the death rate of those with cancer to those without (matched for age, sex, *&c.*), it does not reflect on the "cure rate" for cancer, and does not inform as to what happens after the 5 year interval. Lung and bronchus cancer are the leading cause of cancer-related death in men and women, almost 160,000 individuals. Following lung

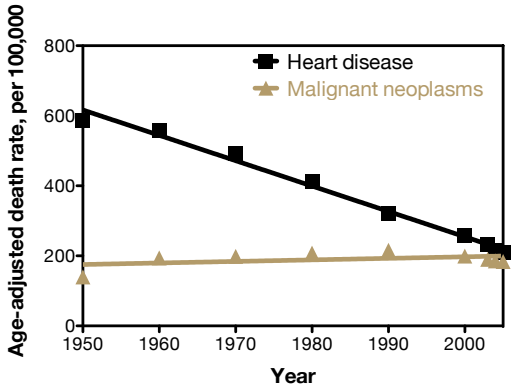

Figure 1: The age-adjusted mortality rates for cancer and heart disease, 1950–2005. Rates shown are for all persons. Lines are a linear regression shown as a visual guide. Data from statistics provided by the Centers for Disease Control.[176]

cancer is prostate and breast cancer in men and women, respectively. Cancer is still the number two cause of death in the U.S., behind heart disease. While great strides have been made in improving patient care for those with heart disease, less progress has been made for patients with cancer. A comparison of the mortality rates of cancer and heart disease are illuminating, as shown in Figure 1 on this page. The flat death rate of cancer relative to other diseases is not due to a lack of effort, but instead, is a reflection of the complexity of cancer biology and the heterogeneity inherent in cancer. The improvements made in cancer management (*e.g.,* anti-smoking campaigns for lung cancer) are offset by an increasingly aging population. In heart disease, the organs systems involved are constant, the disease pathogenesis is better understood, and there are defined prognostic biomarkers to inform on the disease state and best course of therapy (*e.g.,* LDL cholesterol levels). Many of these factors are not true with cancer.

1.3 Carcinogenesis and cancer biology

Cancer is largely a disease of aging. Genetic mutations accumulate throughout life, a result of ionizing radiation exposure, environmental exposure to mutagens, genetic replication errors, and viral infections. The varied pathogenesis inherent in cancer genesis means that

every cancer is to some degree unique. The incidence rate of many cancer types is age-dependent, suggesting the accumulation of cancer traits is a stochastic process.[205]

For cancer to present, a cell must first acquire a set of traits inherent to most if not all cancers. Hanahan and Weinberg enumerated these traits:[94]

Evading apoptosis: Cancer cells ignore programmed cell death, reducing the death rate of cancer cells.

Limitless replicative potential: The normal lifetime limit on cell division (the "Hayflick limit") is overridden, allowing cancer cells to replicate endlessly.

Self-sufficiency in growth signals: Cancer cells provide their own growth signals, leading to a positive feedback loop for cell proliferation.

Insensitivity to anti-growth signals: Cancer cells ignore anti-growth signals to stop proliferation.

Sustained angiogenesis: Cancer cells recruit new blood vessels to supply the nutrients needed for rapid growth.

Tissue invasion and metastasis: Cancer cells are able to undergo a transformation to a more mobile cell type, invade into a new area of the body, and grow in the new location.

These abilities do not need to be acquired in any specific order, as shown in Figure 2 on the next page. For example, a cell could have a telomerase mutation that allows it to have limitless replicative potential, but if the anti-growth signal pathways are still functional, the cell may not proliferate.

1.3.1 Cellular immortality

Apoptosis is orderly, programmed cell death. Cells signaled to undergo apoptosis decrease in volume, fragment their nucleus, and break down their nuclear contents and skeleton.

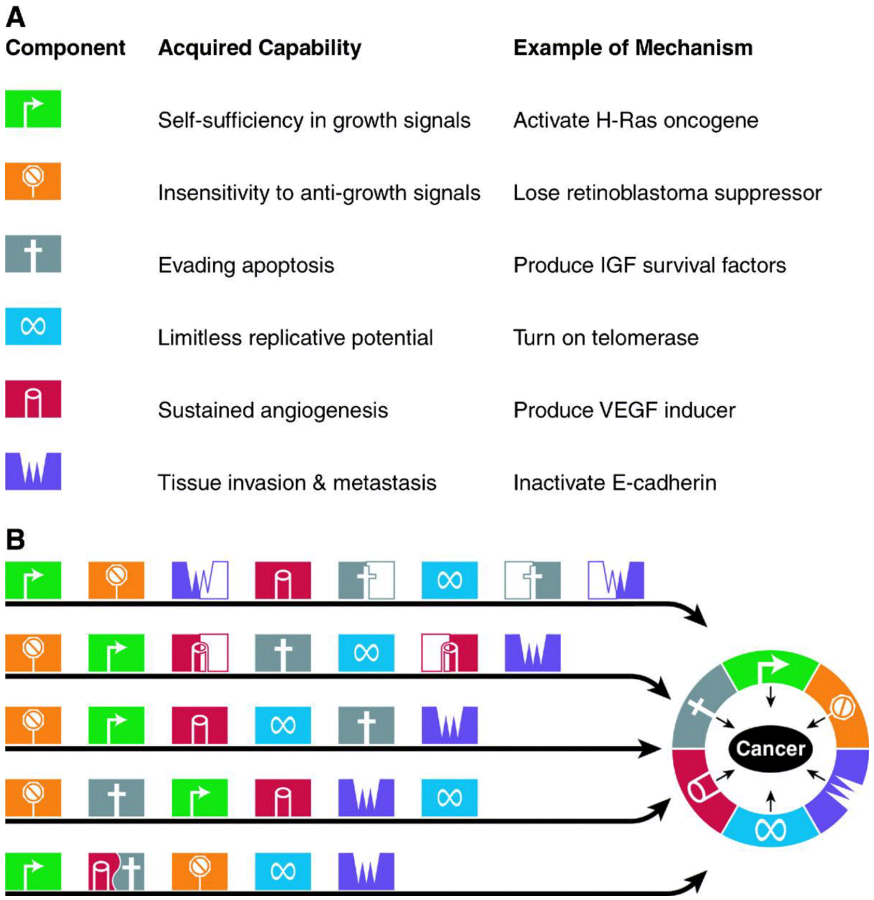

Figure 2: The hallmarks of cancer. (A) A listing of cancer characteristics that are acquired through genetic mutations. The characteristics can arise from numerous mechanisms, an example mechanism is given for each characteristic. (B) The chronological order that these mutations are acquired is not important to the development of cancer, it is the presence of all the characteristics that is the hallmark of cancer. Reprinted from Cell, vol. 100, Hanahan and Weinberg, "The Hallmarks of Cancer", pp. 57–70, Copyright 2000, with permission from Elsevier.[94]

They also express factors that signal phagocytic cells to engulf the apoptotic cell and remove it. This process is contrasted to necrosis, which results in the death of the cell and spillage of its contents into the surroundings (often with deleterious effects to the organism). Apoptosis is used to maintain homeostasis of tissue and organ size, among other roles. Apoptosis is suicide, and relies the cell to carry out the program—cancer cells have mutations in apoptosis regulation pathways that allow cancer cells to ignore pro-apoptotic signaling.[11] The p53 tumor suppressor gene is the best known example in this area: p53 triggers apoptosis if genetic damage is detected. Mutations in the p53 gene prevent p53 from activating the apoptosis pathway.[109] Genetic defects in the gene encoding p53 result in a predisposition to early cancer development, called Li-Fraumeni syndrome.[218, 238]

Cancer cells also have the ability for limitless proliferation. Differentiated primary cells obtained from an organism and grown in cell culture will cease proliferating after time, in contrast to cancer cells that will endlessly proliferate. The observation that differentiated primary cells can only undergo a finite number of cell divisions is now called the "Hayflick limit."[100, 99] This limit is linked to the length of non-protein coding regions at the end of chromosomes, the telomeres. Every time a cell replicates its chromosomes, the telomeres are shortened; if the telomeres become too short, the cell no longer is able to replicate its genetic material. Telomerase lengthens the telomeres. Cancer cells have upregulated levels of telomerase, reversing the shortening of telomeres after replication, and allowing them to replicate without limit.[46]

1.3.2 Alterations in growth signaling

Normal cells are quiescent until they receive a signal to proliferate, transmitted by growth signals. These growth signals bind to transmembrane receptors on the cell and induce signaling cascades that initiate cell replication. The need for growth factors is known to researchers whom use cell culture models: growth hormones must be added to the cell growth medium to propagate the cell culture. A cell that can self-stimulate proliferation

produces daughter cells with the same ability, setting up a positive feedback loop. Growth factor receptors involved in cancer are often receptor tyrosine kinases (RTKs). Mutations in the receptor could be truncations that result in receptors that are constitutively activated or increases in the copy number of the receptor (boosting the "gain" of the receptor pathway). A truncation mutant of epidermal growth factor receptor, EGFRvIII, is found in glioblastoma multiforme;[101] overexpression of a related member in the EGFR family, HER2/neu, is found in breast cancers.[275, 210] Mutations in the downstream signaling effectors of growth factor receptors is also common to many cancers. For example, mutations in the mitogen-activated protein kinase (MAPK) signaling pathway are associated with many cancers.[71, 188, 241, 258]

Cancerous cells also cease responding to signals to halt proliferation. Cells of the colon are continuously sloughed off and replaced from a pluripotent cell source at the base of the colonic crypts. A mutation in the adenomatous polyposis coli (APC) gene prevents the pluripotent cells from ceasing proliferation. Dysplastic nodules of cells then form, termed adenomatous polyps.[274, 108] These cells require a second mutation to become neoplastic, such as a mutation that decreases expression of Krüppel-like factor 4 (KLF4).[280] Patients with a hereditary condition, familial adenomatous polyposis (FAP), have an inherited genetic mutation in the APC gene that causes them to have a predisposition to polyp growth and eventual cancer development.

1.3.3 Increased nutrient supply and mobility

All cells require oxygen, nutrients, and waste removal to survive; as a consequence of diffusion, all cells must be in proximity to a capillary to survive. Solid-mass cancers without the ability to promote angiogenesis, the development of new blood vessels, are unable to grow beyond a small size. Only when solid cancers secrete the soluble factors which promote angiogenesis can cancers grow large—before acquiring this trait, premalignant lesions can be detected in otherwise healthy individuals.[80, 82, 20] Anti-angiogenesis chemotherapy

attempts to circumvent the ability of cancerous lesions to recruit new blood vessel development, in effect, starving the cancer.[87] This therapy is able to prevent further growth of cancer, but must be combined with other therapies to kill the existing disease.[81] A consequence of blood vessel recruitment is that solid-mass cancers are able to use the neovasculature in transporting itself to another area of the body. The metastasis process may involve an epithelial to mesenchymal transition (EMT), which produces a cancer cell with increased mobility.[98, 249] Metastasis is a complex and poorly understood process with many moving parts: the cancer must be able to "unroot" itself from the extracellular matrix (ECM), dodge the immune system and travel to a distant location, and then invade into the tissue of the new location. This requires the alteration of cell-surface receptors, like integrins and cadherins, and the production of proteases to break down the ECM.[5, 32, 145] Metastasis greatly complicates cancer treatment, since the metastatic disease tends to grow in not one distant site but many. Metastasis involves the lymphatic system (the body's "second circulatory system") during transport. The involvement of the lymphatics is why during cancer surgery, lymph nodes are removed during the surgery to stage (determine the extent of the spread of) the cancer. The lymph nodes are analogous to drains in the body's drainage system, and the closest drain to a solid-mass tumor will most likely be the first stop for metastatic disease. This lymph node is termed the sentinel lymph node (SLN), and is of great medical importance.

1.3.4 Tumor structure

The tumor structure is heterogenous. The cells found in a tumor have diverse phenotypes.[58] As discussed *supra*, the tumor has a vasculature to support it with nutrients, however, this vasculature tends to be "leaky."[117] There is also an interstitial pressure associated with the tumor that can make the tumor difficult to penetrate with small molecules and macromolecules.[102] The tumor cellular environment is also varied: there can be necrotic cores of dead cells and detritus distant from neovasculature mixed in with

the cancerous cells; the necrotic regions are generally apoxic and respond differently to anti-cancer therapy.[18] These heterogeneities present impediments to therapy. The intratumoral pressure alters the permeation of drugs into the tumor, and biopsies of tumors are challenging because it is difficult to ensure that the biopsy sample is representative of the cancer as a while. The heterogeneity also poses challenges in probing the cancer after surgical excision, since cost constraints prevent routine pathologic examination of the entire tumor mass. Tumor heterogeneity also poses problems in chemotherapy and radiation therapy because the distribution of cells in a tumor will respond to varying degrees to the treatment. Using one chemotherapeutic (*e.g.,* cisplatin) may kill most but a small subset of resistant cells. These cells will then form a new tumor with resistance to chemotherapeutics. The population distribution within cancer is why combination therapies are commonly used.

1.4 Dissertation Structure

This dissertation describes the development of biomedical instrumentation for intraoperative guidance during cancer surgery, as well as speculating on the biocompatibility of some nanoparticle contrast agents. The dissertation is roughly halved into one part describing instrumentation and the use of the instrumentation for cancer surgery, and one part exploring nanoparticle degradation. A short description of each chapter appears *infra*.

Chapter 1: In this, the introductory chapter, we define cancer as the medical area of interest and examine the impact of cancer on society.

Chapter 2: Here, we review the current field of biomedical imaging for cancer, including nanotechnology-based contrast agents compatible with the instrumentation described in Chapter 3.

Chapter 3: In this chapter we describe the design and current implementation of biomedical instrumentation for image-guided cancer surgery using exogenous contrast

agents.

Chapter 4: Using the instrumentation developed in Chapter 3, here we use the technology to guide surgery in animal models of cancer and lay the groundwork for translation of this instrumentation into the clinic.

Chapter 5: In this chapter, we describe how a class of nanoparticles can be rapidly degraded by reactive chemicals, and how the damaged particles can be partially repaired.

Chapter 6: Here, we describe how the process described in Chapter 5 is relevant in the *in vivo* milieu, and use *in vitro* assays to speculate on the *in vivo* fate of some nanoparticles.

Chapter 7: Finally, we predict the future development of the discoveries presented in this dissertation, including applying the technology to human diseases outside of cancer and making use of the degradation of nanoparticles for practical purposes.

Appendix A: A detailed listing of materials used throughout the dissertation, including software, instrumentation, chemicals, and consumables.

Appendix B: A detailed listing of the optical prescriptions of instrumentation developed in this dissertation.

Appendix C: A pseudocode outline of software developed for use in this dissertation.

1.5 Conclusions

As our understanding of cancer as a disease grows, the difficulty of the challenge of eradicating cancer becomes apparent. Cancer is truly a consequence of life as we know it. The mutations that allow evolutionary processes to happen in life are also responsible for causing the suffering that is cancer. Although one word is used to describe it, cancer exhibits the same individuality as the people it afflicts. The growing knowledge of the genetics

and biology of carcinogenesis are one development that will improve cancer diagnostics and prevention. Developments in nanotechnology, which offer fine-grained control over material properties in a way not possible otherwise, offers opportunities to improve cancer therapy.

CHAPTER II

NANOTECHNOLOGY FOR *IN VITRO* AND *IN VIVO* IMAGING

2.1 Abstract

Nanotechnology offers unprecedented control over the physical, chemical, and electronic properties of materials. Although it is relatively new as a field, nanotechnology has already found its way into consumer products (such as in cosmetics and sunscreens, stain-free clothing, and antimicrobial surface treatments). The potential for nanotechnology to transform human medicine is incredible. In this dissertation, we are concerned with nanotechnology applications in cancer, specifically imaging. The unique electronic and optical properties of nanoparticles prove to be especially useful for cancer imaging, and biological imaging in general.

2.2 Introduction

Nanotechnology was conceptually born as a talk, "There's Plenty of Room at the Bottom", given by physicist and Nobel laureate Richard Feynman in 1959.[74] In his talk, Feynman predicted the emergence of a multidiciplinary field that would focus on the manipulation of structures and materials at the atomic scale. As an example, he proposed how the entire *Encyclopedia Britannica* could be stored on the head of a pin; he (through the suggestion of an acquaintance and later student, Albert Hibbs) speculated on a "wild idea" that one could "swallow the doctor", a micromachine that could be remotely controlled and used for surgery; and he observed how the unique properties of the atomic scale (where quantum mechanics dominates) could lead to "a system using quantized energy levels".

Early definitions of nanotechnology described it as the manipulation of individual

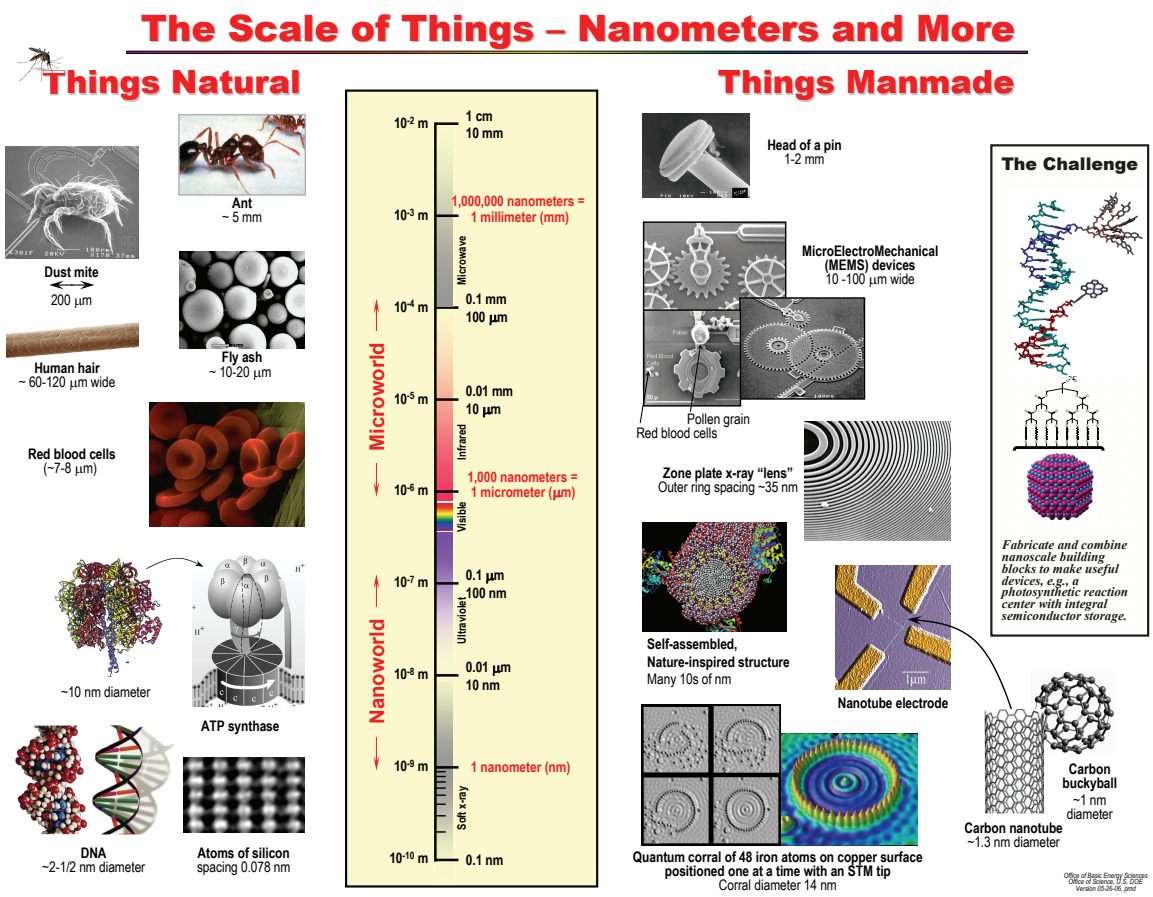

Figure 3: The scale of things, from macro to nano. The unique properties of nanoparticles emerge when the particle size decreases below 100 nm. This is below the wavelength of visible light, part of the reason for some of the interesting properties of nanoparticles. It is also the scale of biomolecules and proteins. Image courtesy of the U.S. Department of Energy, Office of Basic Energy Sciences.[254]

atoms or molecules, but a more modern definition is provided by the U.S. National Nanotechnology Initiative:[177]

> Nanotechnology is the understanding and control of matter at dimensions between approximately 1 and 100 nanometers, where unique phenomena enable novel applications. Encompassing nanoscale science, engineering, and technology, nanotechnology involves imaging, measuring, modeling, and manipulating matter at this length scale.

It is in the mesoscopic regime where the familiar properties of a bulk material are combined with the weird quantum behavior of atoms and molecules. True nanotechnology goes beyond being small: it is the control of matter to exploit properties not apparent in individual atoms or in bulk materials. Nanotechnology produces materials that are smaller than

the wavelength of visible light and on the same order of size as biomolecules, as illustrated in Figure 3 on the preceding page. This is in part why nanoparticles have optical properties not seen in bulk materials; it is also why nanoparticles can have toxicity effects not seen in bulk materials. This dissertation is in part concerned with the degradation of semiconductor quantum dots, and so they are discussed thoroughly. Gold colloid, used for enhancing Raman scattering, is useful as a contrast agent for the instrumentation presented and so is discussed but in less depth. We begin by discussing the challenges and considerations inherent to optical imaging *in vivo* before discussing useful optical nanoparticles.

2.3 Optical imaging in vivo

Fluorescence imaging has several inherent advantages over other imaging modalities: low instrumentation costs, a high spatial resolution, non-ionizing radiation, stable optical probes (*c.f.* radiodecay of radionuclides), facile multiplexing through multispectral imaging, and the opportunity to use switchable or activatable probes to increase sensitivity and specificity. Imaging with visible or near-infrared (NIR) light has unique difficulties not inherent to nuclear medicine, sonography, or x-rays. Optical imaging is mainly hampered by a limited penetration depth through tissues of the body due to Rayleigh scatter and absorption by endogenous chromophores.[195, 34, 184] As a result, optical imaging has seen wide use in research studies using rodent models where the light can penetrate deeply relative to the total size of the animal; In human medicine, optical imaging has been largely restricted to transparent organs (imaging the retina with optical coherence tomography, OCT) or surface imaging (*i.e.,* narrow-band imaging in colonoscopy). For some human medicine applications, the shallow penetration depth of light is not an issue. In surgery, for example, most areas of interest will be a surface (either intact or freshly cut). For surgical applications, the imaging will most likely be carried out with an epi-fluorescence scheme, as depicted in Figure 4 on the next page, because the excitation source and detector can be easily made into the same hand-held probe. The advantages of transillumination and

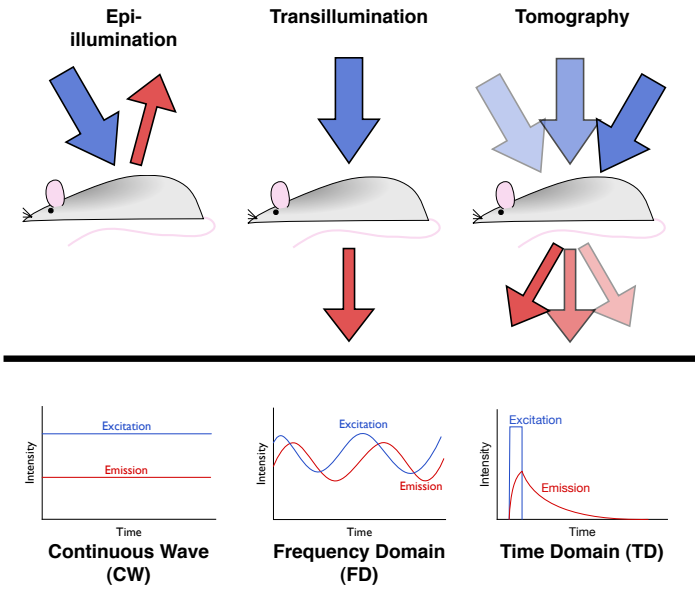

Figure 4: Fluorescence imaging *in vivo* commonly uses one of three imaging arrangements, epi-illumination, transillumination, or tomographic illumination. The excitation source can be a continuous wave, or can use a time- or frequency-varying signal. Continuous wave epi-illumination is the simplest to implement and is the most common strategy.

tomography to reduce the surface-weighting of fluorescence imaging are not outweighed by the increased instrumentation cost and complexity. There are several possible imaging domains that have been used for *in vivo* imaging, but continuous wave (CW) imaging is by far the most common. CW imaging offers higher sensitivities because the duty cycle for CW excitation is unity. The duty cycle for both frequency-domain (FD) and time-domain (TD) excitation sources is less than unity, reducing the amount of excitation light delivered and thus emission light that can be collected. The drawback to CW is an inability to measure fluorescence lifetime, which can be useful to reject unwanted signals. Acquiring spectrographic information with CW excitation offsets this drawback. FD excitation has some implementation advantages over TD excitation (namely, an insensitivity to ambient light); in terms of the data acquired, the two excitation modes are mathematically related through the Fourier transform.

2.3.1 The near-infrared window

There exists an optimal region of light for *in vivo* imaging, the so called "near-infrared window."[34, 262, 231] This is the observation that there are ranges of light where absorption due to endogenous chromophores is relatively low; selecting the most bathochromic of these ranges will result in the lowest scattering since Rayleigh scatter (scatter due to structures much smaller than the wavelength of light) is proportional to $\frac{1}{\lambda^4}$. Mie scatter also occurs in tissues, but is anisotropic (forward-biased) in contrast to the isotropic scatter of Rayleigh scatter. The sum of absorption and scatter is the total attenuation of light experienced in the tissues. The major chromophores of the body are water (in the NIR) and hemaglobin. As shown in Figure 5 on the following page, there is a clear range of imaging in the 650–1300 nm range; this window is split into two ranges based on the efficiencies of available imaging sensor materials. Imaging sensors based on silicon (Si) are by far the most common and economical, and so imaging in the NIR window tends to occur in the 700–850 nm range where the Si sensor efficiency is high and there are a large selection of fluorophores to use. Semiconductor quantum dots (QDs) are easily tuned to emit within the entire NIR window: one of many reasons why QDs are attractive for use as biological labels. Raman-scattering tags, such as those based on gold colloids, are another nanoparticle that can be used within the NIR window.

2.4 Semiconductor quantum dots

A semiconductor quantum dot (QD) is a structure in which an exciton, an excited electron and hole pair, is spatially confined in three dimensions. Such a structure exhibits many interesting optical effects as the magnitude of the spatial confinement is altered. If the structure is confined in two of three dimensions, it becomes a quantum wire; for one in three dimensions, a quantum well. It is important to note that the term "quantum dot" refers to the confined particle (in this case, exciton), and is not necessarily synonymous with a semiconductor QD, much less a colloidal quantum dot. The fine-grained control

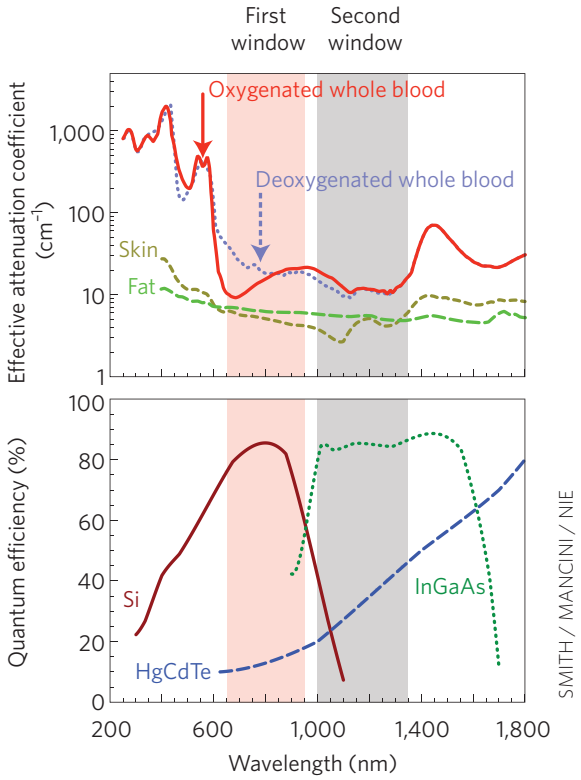

Figure 5: Biological imaging through the near-infrared window. The near-infrared (NIR) window is the range where endogenous chromophores (top) have an absorption minima. Using the most bathochromic range possible also reduces the impact of scatter. The window can be split into two ranges, based on the efficiencies of imaging sensors available (bottom). By far, silicon (Si) is the most common imaging sensor material. Reprinted from Smith *et al.* [231]

over the optical and physical properties of semiconductor QDs is why they are useful to a wide variety of fields and for applications to a variety of devices, such as light-emitting diodes (LEDs), photodetectors, solar panels, and biological labels.

The first theoretical framework for a semiconductor quantum dot was published in 1981 by Efros and Efros, and they were first synthesized and described by Ekimov and Onushchenko in the same year.[64, 65] The first reported QDs were copper chloride particles precipitated from a supersaturated solution in silica glass; it was found that the size of the particles could be controlled by varying the recondensation time. Interestingly, the glasses showed absorption spectra with features that would shift as a function of the average size of the copper chloride particles—these shifts were correctly attributed to quantum confinement. Quantum confinement is part of what makes quantum dots interesting; by merely altering the size of a quantum dot, but maintaining the same material composition, the emission wavelength can be drastically and predictably shifted as shown in Figure 6 on the next page. In comparison, a fluorescent dye requires alterations to the structure (*e.g.,* addition of electron withdrawing groups) and so tuning the fluorescence emission is much more difficult to predict and accomplish.

A rough conceptual framework for quantum confinement is given by the "particle in a box" thought experiment, where the energy available to a free particle of a given mass restricted in motion to one dimension is

$$E_n = \frac{h^2 n^2}{8ma^2} \tag{1}$$

where E_n is the sum of kinetic and potential energies (kinetic only in this case), h is Planck's constant, n is the quantum number, m is the mass of the particle, and a is the length of the dimension that the particle is restricted within.[158] It is readily apparent that by decreasing the size of the dimension that the particle is restricted within increases the energy available to the particle. This is a reflection of Heisenberg's uncertainty principle

$$\Delta x \Delta p \approx h \tag{2}$$

Figure 6: Colloidal quantum dots (QDs) have size-dependent emission color. A series of semiconductor quantum dots, emitting light between 447–665 nm can be simultaneously excited with a single UV hand lamp. The composition of the particles are the same, only the size differs. Reprinted by permission from Macmillan Publishers Ltd: Nature Biotechnology ref. [93], copyright 2001.

that as the uncertainty of the position, Δx, of the exciton becomes smaller (*i.e.,* better known by decreasing the size of the particle), the uncertainty of the exciton momentum, Δp, must increase (and so increase the energy of the now confined exciton).[158]

One year after Ekimov and Onushchenko's report, Rossetti and Brus described radiative recombination (*i.e.,* fluorescence emission) in cadmium sulfide (CdS) colloids (*i.e.,* fluorescence emission), and Henglein almost simultaneously reported the fluorescence emission and quenching of cadmium sulfide colloids.[213, 104] Numerous publications on the properties of various semiconductor colloids followed, in addition to theoretical frameworks advanced by Brus and Henglein, among others.[79, 134, 263, 223, 24, 23] In 1993, Murray, Norris, and Bawendi published a seminal paper on the synthesis of high quality cadmium chalcogenide (group 16 elements) nanoparticles in high temperature organic solvents, and this work has been the basis for creating high-quality semiconductor quantum dots since.[173] Cadmium chalcogenide QDs are probably the most commonly used QD in scientific research: much of this popularity can be attributed to the early publication of the

high quality synthesis method of Murray *et al.*, published when QDs first began attracting interest from the wider scientific community.

2.4.1 Structure and synthesis

Colloidal semiconductor quantum dots can be made from a range of semiconductor materials, most commonly group IV-VI and group III-IV materials. As mentioned *supra*, an early method for producing high-quality group IV-VI QDs was published by Murray *et al.* in 1993, and this method or adaptations of this method are arguably the method used to produce most QDs for applications in biology. As such, we summarize the procedure of Murray *et al.* in detail. The synthesis is based on injecting precursor solutions into a hot bath (190–300 C, depending on the chalcogen and precursor stock solution, and coordinating solvent used) of a coordinating solvent. In the original procedure, trioctylphosphine oxide (TOPO) was heated to 300 C under oxygen-free conditions. Cold precursor solutions of dimethylcadmium ($(Me)_2Cd$) in trioctylphosphine (TOP) and selenium in TOP (TOP-Se) are mixed and rapidly injected into the hot TOPO bath. The injection of the cold precursor creates a supersaturated solution and initiates an immediate nucleation and formation of small crystals. The cold precursor also cools the coordinating solvent bath that the reaction occurs in; the lower temperature, combined with depletion of precursors due to nucleation, arrests nucleation of new particles and promotes addition of material onto the already formed crystals. By controlling the temperature of the coordinating solvent, the growth rate of the already formed crystals can be controlled. The crude reaction mixture is monitored by optical spectroscopy to estimate the size and distribution of the particles produced. Once grown to the desired size, the particles are purified from the crude reaction mix by precipitation in methanol, centrifugation, and resuspension in 1-butanol ("washing"). The particles are then further purified by size-selective purification, where the bare minimum of methanol is added to cause the QD solution to become turbid due to flocculation of the largest particles. These large particles are then isolated by centrifugation,

leaving the smaller particles dispersed in the supernatant. This size-selective precipitation method can produce a population with a narrow size distribution (less than 5% RMS in diameter); other solvent systems (*e.g.,* methanol/chloroform) can be used so long as one solvent is a non-solvent that causes flocculation, and the other solvent is able to disperse the QDs. In the methanol/1-butanol example, methanol alters the polarity of the solvent, promoting flocculation through van der Waals forces. Surfactants other than TOPO might call for a different solvent system for purification and size-selective precipitation.

The isolated and purified particles are then characterized, usually by a combination of absorption spectroscopy, fluorescence spectroscopy, dynamic light scattering (DLS), and electron microscopy (EM). Absorption spectroscopy offers a wealth of information on the electronic structures of the synthesized particles. For example, differences in the crystal lattice type (zinc blende vs. wurtzite) can be detected through absorption spectroscopy. Fluorescence spectroscopy informs on the purity of the particle population: highly monodisperse samples will have a narrow band-edge emission peak. The lack of "deep trap" emission (broad, featureless emission bathochromic to the band-edge fluorescence peak) is indicative of good surface passivation by solubilizing surfactants. Dynamic light scattering can be used to estimate the size of the particles and polydispersity of the particle population. Finally, electron microscopy can confirm size estimates from dynamic light scattering measurements, and also inform on the lattice structure of the particles (provided the resolution of the microscope is high enough) and the presence of stacking faults in the crystals. Some electron microscope modalities can also provide chemical analysis, *e.g.,* energy dispersive x-ray (EDX). Electron microscopy of QDs is hindered slightly in that the particles will tend to orient with the long axis on the microscopy substrate.

Colloidal QDs may also be generated with a core/shell structure, each having a different material composition. Hines and Guyot-Sionnest reported a simple procedure to grow a zinc sulfide (ZnS) shell on CdSe particles (CdSe/ZnS) that has inspired numerous refinements to the procedure.[107] As noted by the authors, growing layers of materials with a

wider bandgap on top of materials with a narrower bandgap insulates the core from the surrounding solvent, reducing the influence of the shell and surface passivation on the optical properties of the QD. The result are particles with superior quantum yields and increased resistance to photooxidation. The synthesis itself begins with a variant of the procedure used by Murray *et al.*, and then adds dimethylzinc and bis(trimethylsilyl)sulfide precursor solutions in TOP to the freshly synthesized monodisperse CdSe population.[127] The Zn/S precursors are added in several steps to promote epitaxial growth of ZnS on the existing CdSe particles. After synthesis, the particles are purified and characterized in the same fashion as the CdSe cores.

2.4.2 Water solubilization strategies

The QDs synthesized in high-temperature organic solvents are left with a passivating surfactant layer that is in most cases insoluble in water. The Nie group has recently published methods (applicable to other particles in addition to QDs) that can produce particles that are both good-quality and directly soluble in water.[233, 125] To make the particles usable for biological applications, they must be made water soluble. Smith *et al.* reviewed a number of water solubilization strategies for QDs, exploring the optical and physical properties, resistance to oxidation, and behavior in live cell cultures.[229] Water solubilization strategies can be divided into methods which replace the hydrophobic surfactants from QD synthesis with a water-soluble surfactant (ligand exchange); the other major method is to overcoat the particles with a layer that interfaces with the existing hydrophobic surfactants and also presents a water-soluble moiety (encapsulation). A comparison of the physical parameters of QDs with different surface coatings appears in Figure 7 on the following page.

In general, ligand exchange procedures are easy to carry out and can be done quickly. Many times, the ligand used is a alkane thiol; mercaptoacetic acid (MAA) and mercaptopropionic acid (MPA) are common monodentate thiol ligands used in exchange. The

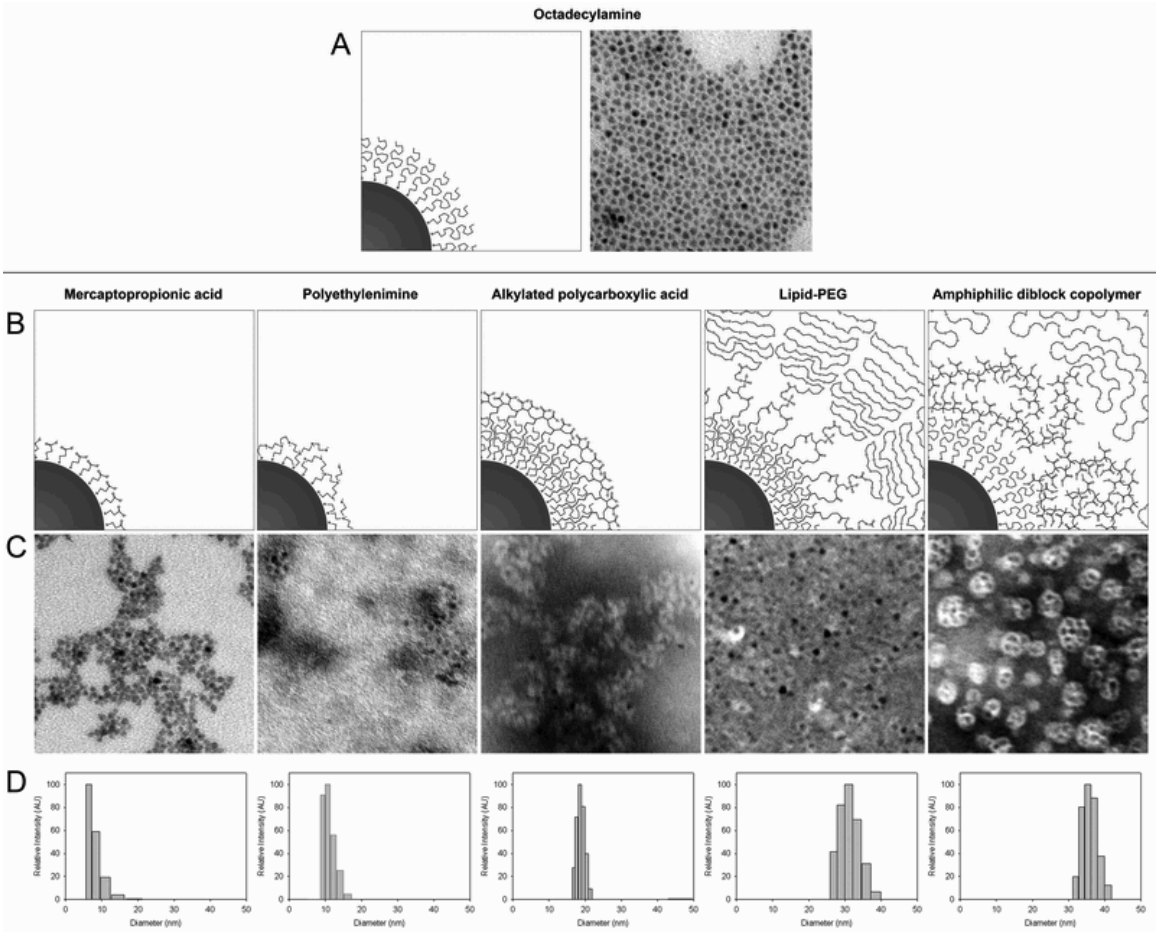

Figure 7: A comparison of quantum dot (QD) surface coatings. Semiconductor quantum dots (QDs) synthesized in organic solvents (shown in A) can be made water soluble by a number of different surface chemistries (shown in B–D). The different surfaces produce QDs of different hydrodynamic sizes (represented in the cartoon figures of B and the dynamic light scattering data shown in D). The bulkiness of the polymer coatings can be seen as the white ring around the dark QD crystals in the transmission electron microscopy figures of C. Adapted in part from ref. [229]—Reproduced by permission of the PCCP Owner Societies.

downside of ligand exchange as a surface coating is that in many cases, it produces particles that are unstable beyond a few days following the exchange procedure. This instability is attributed to the labile nature of the dative metal–thiol bond. Aldana *et al.* showed that CdSe QDs promote photocatalytic oxidation of thiol ligands (into dithiols), and that these oxidized thiols are less able to keep QDs dispersed in solution.[7] Aldana *et al.* also showed that the bidentate thiol, dihydrolipoic acid, had no greater resistance to the photocatalyzed oxidation process than the monodentate thiol ligands, but this later point is contested.[194, 153] These thiol ligand exchange QDs, in addition to having poor long-term stability, also tend to have lower quantum yields than encapsulated QDs. Thiol ligand exchange QDs are also difficult to functionalize through common carbodiimide chemistry, reducing their ultimate utility for biological applications.[153] Different from the thiol ligand exchange methods, Duan and Nie reported a coating made from polyethyleineimine (PEI), a hyperbranched amine.[62] This coating was reported to be very stable had have good optical properties. Later, it was reported that this coating also had unusually high acid stability.[165] Finally, Smith and Nie have recently introduced a multidentate ligand with combining multiple thiol and amine ligands, with superior stability and brightness in comparison to thiol ligands.[232]

Encapsulation procedures, in contrast to ligand exchange procedures, require more time, more reagents, and more skill. The encapsulated QDs produced are however more photostable, more colloidally stable, and tend to have better optical properties than ligand-exchange QDs. Much of the improvement in behavior is because the hydrophobic surfactant layer from QD synthesis is maintained, and the hydrophobic layer better protects the QDs from the deleterious effects of molecular oxygen (O_2) in the environment. Alkylated polymers are a common encapsulation compound because the QDs that result are colloidally very stable (years in aqueous solution without special storage considerations), optically very bright, resistant to photooxidation, overall small, and permit facile bioconjugation through carbodiimide chemistry.[269, 9] PEGylated lipids are another common

encapsulation compound: they produce larger particles, but are otherwise similar to the alkylated polymer QDs with a slightly simpler and faster encapsulation procedure.[63] Finally, QDs can be encapsulated in a silica shell as was done in one of the original biological application papers.[22] These particles are chemically very stable, but the overall quantum yield tends to be low, and the particle size is very large. Commercially, only alkylated polymer and lipid micelle QDs are found for general sale.

2.4.3 Mechanism of operation

The innerworkings of QDs have been extensively reviewed in the literature.[159, 235, 160, 68, 239, 15, 183] A bulk semiconductor material has a band gap energy dependent on the material composition. The band gap is the minimum energy required to promote an electron from the ground state energy level (valence band) into a higher, unoccupied energy level (conduction band). If a photon with energy greater than the band gap is absorbed by the bulk semiconductor material, it will result in an electron leaving the valence band and entering the conduction band. This leaves behind a positively charged hole in the valence band. The lowest energy configuration is for the electron to remain bound to the hole through Coulombic attraction, and this quasiparticle atom pair is known as an exciton. The exciton can later recombine, releasing the energy as a lower energy photon than the excitation photon—a radiative recombination event. The exciton can also cease existence through non-radiative pathways such as the ejection of an Auger electron (leaving behind a charged and non-emitting "dark" QD) or though lattice vibrations (heat). The lifetime of the exciton is controlled in part by the spacial overlap of the electron and hole wavefunctions, and is illustrated in Figure 8 on the next page. In this figure, the band gap is depicted as the vertical distance between the hole and electron wavefunctions.

In a semiconductor quantum dot, the size of the bulk material is reduced below the size of the exciton (defined as the Bohr exciton diameter). Below the Bohr exciton diameter, the confinement of the electron and hole wavefunctions increases the energy associated with

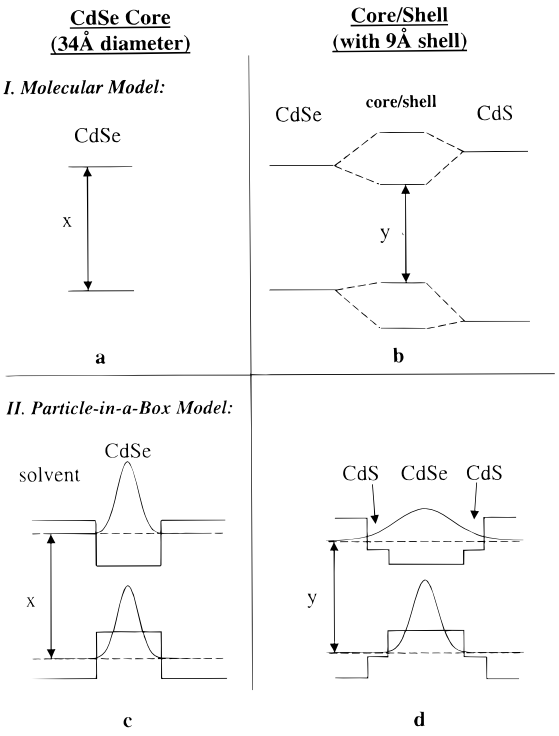

Figure 8: A schematic of the electronic configuration of two quantum dot (QD) structures. The electronic states available to a homogenous quantum dot (left) are compared to a core/shell quantum dot (right), modeled with both a molecular orbital framework (top) or a particle-in-a-box framework (bottom). The particle-in-a-box framework depicts the differences in wavefunction overlap between the hole and electron in an heterogenous core/shell structure. Reprinted with permission from ref. [197]. Copyright 1997 American Chemical Society.

this state—the band gap of semiconductor becomes quantized, and the optical properties of the resulting QD become size-dependent. The confinement of the electron and hole wavefunctions also has implications for the excited state lifetime of the QD (since exciton lifetime is in part controlled by the spacial overlap of the wavefunctions). In a homogenous material, the overlap is solely controlled by the size of the QD; in a core/shell or other heterostructure, the electron and hole can be made to occupy discrete regions of the particle. A long excited-state lifetime can be useful in biological imaging to discriminate signals from fluorophores from endogenous fluorophores and the biological background.

Nanoparticles have a large surface area to volume ratio. The optical properties of a QD are therefore influenced by the state of the QD surface. Preventing the exciton from interacting with the surroundings is critical in producing particles with high quantum yield (QY, the rate of photons emitted versus photons absorbed). Growing an insulating shell on the QD is one way the exciton can be isolated from the surroundings, and this is why a core/shell structure can have improved brightness relative to the core alone. Fully occupying the orbitals of the atoms on the surface of the QD is also critical: unbonded orbitals with energy within the band gap can act as traps for the excited electron or hole, resulting in non-radiative recombination (*i.e.,* no fluorescence), or alternatively, a "deep trap" recombination pathway. The effects of the surface chemistry on QD optical emission are diagrammed in Figure 9 on the following page. Deep trap emission is undesirable because it is broad (due to the presence of many trap sites on the QD of varying energy levels) and has an overall low QY. The need to fully occupy the surface orbitals is why the QD surface coating has such a great influence on the QD optical properties. Small-molecule thiol ligand coatings, which are easily oxidized and lost, tend to result in QDs with lower QY because they leave behind unoccupied orbitals when they become oxidized. Encapsulated QDs, which preserve the thick organic surfactants from QD synthesis, provide a steric and non-polar barrier that better protects the surface of QDs. These encapsulated particles thus tend to have a higher QY.

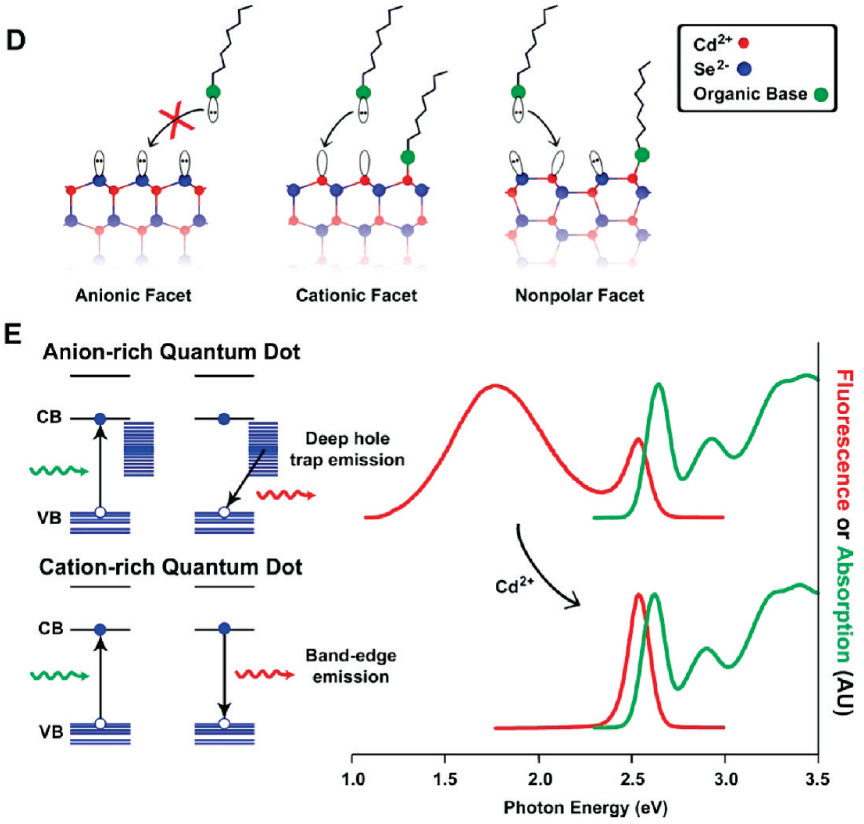

Figure 9: The surface state of a quantum dot (QD) greatly influences its optical properties. The surface chemistry of a quantum dot greatly influences the optical properties because of the large surface area to volume ratio of nanoparticles. (E, left) A depiction of the energy states within two quantum dots, one with a anion-rich surface (*i.e.,* selenium-rich), and one with a cation-rich surface (*i.e.,* cadmium-rich). The dangling orbitals of the surface anions can act as exciton traps, altering the radiative recombination pathway and resulting in a broad emission profile bathochromic from the band edge emission. (D) The orbitals can be passivated in a cation-rich surface by surface ligands, removing the surface trap states, enhancing band edge emission efficiency, and eliminating the undesirable trap emission as depicted in (E, right). Adapted in part with permission from ref. [234]. Copyright 2009 American Chemical Society.

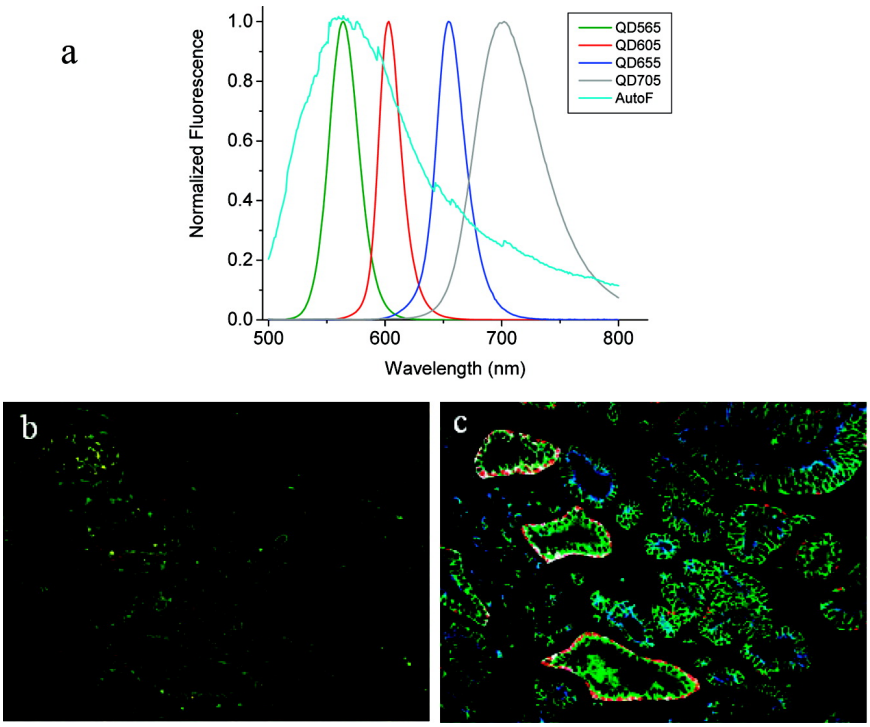

Figure 10: Semiconductor quantum dots (QDs) offer brighter, multiplexed immunofluorescence over fluorescent dyes. Immunofluorescence was performed with QD-antibody conjugates on prostate tissue. The symmetrical band edge fluorescence emission of quantum dots is distinct from tissue autofluorescence, and the narrow fluorescence bandwidth allows many colors of quantum dots to be imaged simultaneously without overlap, as shown in (A). This allows the raw tissue image, (B), to be easily computer-enhanced to show QDs without background signal, (C). Reprinted with permission from ref. [144]. Copyright 2010 American Chemical Society.

2.4.4 Applications in biology

QDs were first applied in biology by a pair of research teams, simultaneously publishing in *Science* in 1998.[22, 33] The number of groups investigating and applying QDs to problems in biology grew exponentially. QDs are interesting as optical tags for biology applications because of their numerous advantageous optical properties when compared to more conventional fluorescent dyes. Many early applications of QDs have focused on *in vitro* diagnostics. QDs can be directly substituted for the organic dye fluorophore in immunofluorescence assays, as is shown in Figure 10 on the current page.[271] Using QD-antibody conjugates, instead of dyes, has three major advantages, some of which are related to the

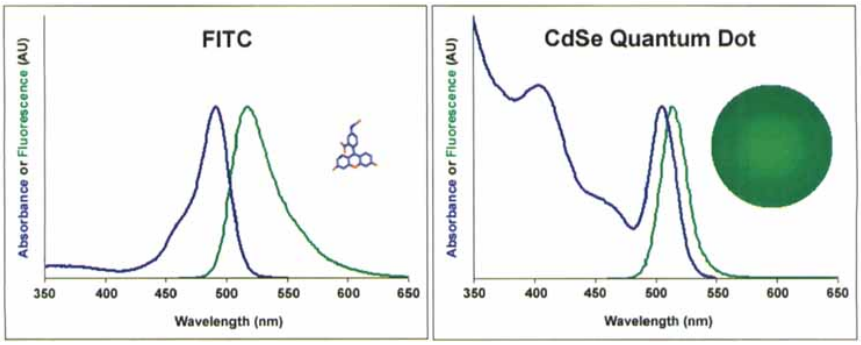

Figure 11: A comparison of the absorption and fluorescence spectra of fluorescein isothiocyanate (FITC) and a semiconductor quantum dot (QD). The absorption and fluorescence spectra of a standard fluorescent dye, FITC, are shown on the left. The absorption peak is near the emission peak, and the emission peak is broad and asymmetric. The absorption and fluorescence spectra of a quantum dot are shown on the right. In comparison to FITC, the QD absorption spectra is broad, increasing in the blue and ultraviolet range, and the QD emission spectra is narrow and near Gaussian. Reprinted with permission from ref. [230]. Copyright 2004 John Wiley and Sons.

absorption and emission spectra as shown in Figure 11 on this page. QDs have a broad absorption range below the band gap, whereas a fluorescent dye has a narrower absorption peak. The broad absorption band of QDs allows QDs with different emission colors to be simultaneously excited by a single band of light (*e.g.,* from a HeCd laser), leading to facile multiplexing. Multiplexing with fluorescent dyes requires a unique and appropriate band of light for every dye used. Further complicating multiplexing with dyes is that the Stokes shift (difference in excitation and emission wavelength) is much less for dyes than QDs, necessitating sharper optical filters for dyes than for QDs. Another advantage of QDs that leads to facile multiplexing is that the emission from a QD is narrow and roughly symmetric (Gaussian), whereas for a dye is broader and asymmetric. The symmetric fluorescence spectra of QDs is computationally simple to isolate from both background light and from other fluorophores. QDs are also much more photostable than fluorescent dyes, in part because the polymer-encapsulated QDs used for immunofluorescence are well-isolated from the surrounding solvent by the thick surfactant and polymer coating. Finally, QDs are also substantially brighter than many fluorescent dyes, in part because of high absorption cross-sections in the blue-UV light range. The advantages of QDs over fluorescent dyes for

immunofluorescence applications has been one of the clear successful applications of QDs.

There are numerous examples of cell culture imaging studies where the superior brightness, resistance to photobleaching, and facile multiplexing inherent to QDs have permitted studies that would not be practical with conventional dyes. For example, in an early *in vivo* application, "inert" lipid-encapsulated QDs were injected into individual *Xenopus* blastomeres and the tissues derived from the injected cell could then be tracked over the development of the embryo.[63] This concept of tracking cell lineage was later applied to stem cell tracking, in which parent stem cells were loaded with inert QDs and the differentiated daughter cells could then be tracked.[142, 211, 215] In these examples, the resistance to photobleaching was a prerequisite to make the long-term tracking study possible. It is true that similar studies could be done with green fluorescent protein (GFP) or a similar expressed fluorochrome, but this would necessitate genetic manipulation and could have undesired side effects. Fluorescent proteins are also less photostable than QDs, although they are constantly replenished if constitutively expressed. QDs have also seen success for receptor trafficking studies. In these studies, the superior photostability and ability to track a single QD (based on the observation of "blinking", intermittent photoluminescence inherent to isolated QDs) made the studies possible. In an early report, Dahan *et al.* followed single glycine receptors in neurons in a cell culture system.[48] Dahan and coworkers, in a later study, also measured the mobility of kinesis motors inside a cell by functionalizing QDs with kinesin motor proteins, and then delivering these QD-kinesin probes into the cell cytoplasm.[47] More recently, the receptor-ligand interaction of neurexin and neuroligin was studied using QDs functionalized with engineered neuroligin constructs and sophisticated computer modeling. [217]

In another proof-of-concept example illustrating the utility of multiplexing in *in vivo* imaging, Kobayashi and colleagues injected mice with several dendrimer solutions labelled with different dyes in spatially separated areas around the neck so that the lymph drainage could then be mapped to the specific node responsible for the area, as shown

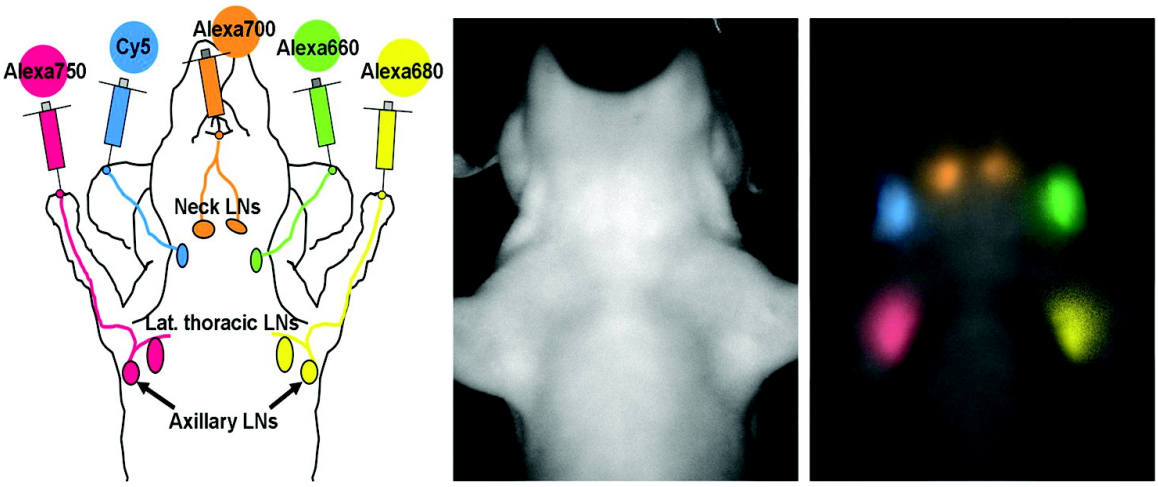

Figure 12: A mouse was injected at different sites around the neck (shown on left diagram) with differently colored fluorescent dyes, and the lymph drainage for the injection site could then be tracked to the draining lymph node. Reprinted with permission from ref. [132]. Copyright 2009 American Chemical Society.

in Figure 12.[133, 132] A limitation that was brought up in this study was that the number of dyes that could simultaneously be used (for near-infrared imaging) was about five; using QDs with narrower near-Gaussian emission profiles would allow for greater throughput multiplexing. Gao and colleagues showed that through hyperspectral imaging, QDs injected into a mouse could be resolved from the background autofluorescence;[86] hyperspectral imaging is used in the same way for multiplexed QD imaging.

2.5 Noble metal colloids

Noble metal colloids have a long history of use, predating the concept of nanotechnology. Early scientific observations of gold and other metal colloids were made by Michael Faraday. Faraday observed in 1857 that when a dilute gold solution is mixed with phosphorous, "a beautiful ruby or amethystene fluid is immediately produced".[72] Faraday theorized that the color was due to small gold particles formed by the transfer of chloride from chloroaurate to phosphorous. He also observed that the gold colloids would appear different, depending on if light were being transmitted or reflected by the solution: a solution transmitting daylight might appear amethystine, yet appear brown and hazy when reflecting

the same daylight. Gustav Mie later, in 1908, provided an analytical solution that would explain Faraday's observation.[161] Finally, Faraday noted that minute quantities of salt would cause a normally ruby colored gold solution to become blue or even transparent, and attributed this color change to the aggregation of the gold particles. Other early experiences with gold nanoparticles are ruby glasses, made since Roman times, and as a treatment for rheumatoid arthritis.[259, 172]

Noble metal colloids, especially gold, have been attractive for biological applications because of unique properties that emerge on the nanoscale. Much of the utility of nanoscale noble metals is due to localized surface plasmon resonance (LSPR).[116] The LSPR is the resonant, coherent oscillation of the electrons of a noble metal nanoparticle, in response to an oscillating electromagnetic (EM) field (*i.e.,* incident light). For both gold and silver, the LSPR occurs in the visual to near-infrared range; since silver has known toxicities and rapidly oxidizes in aqueous environments, gold is the preferred noble metal for biological applications. Noble metal nanoparticles are efficient light scatterers, and so are useful as a contrast agent by itself. A simple dark-field microscope (similar to a standard microscope, but with an obstruction in the light path that allows only scattered light to be observed) is all that is necessary for imaging, and since the imaging is based on scattering, the probes never photobleach.[66] Non-radiative relaxation of plasmon oscillations results in absorption of the incident light, and this absorption leads to heating. This local heating effect has been used by many groups for photothermal ablation as a medical therapy.[67, 190, 189, 113] Colloidal gold has also seen interest for use as a drug delivery carrier, sometimes in conjunction with photothermal therapy for triggered release of drugs or simply as an adjuvant. The high EM fields surrounding the noble metal particles also can be used for enhancement of Raman scattering.

2.5.1 Gold colloid synthesis

Gold colloid synthesis is well-described in the literature and simple to execute using common laboratory equipment.[49] For larger particles (such as the size useful for Raman scattering enhancement), Frens' method (itself a modification of Turkevich's method) of citrate reduction of auroperchlorate is commonly used.[84, 253] In this process, auroperchorate is refluxed after the addition of a controlled quantity of citrate; the amount of citrate controls the size of the particle produced. This produces a good yield of gold particles with acceptable uniformity and in an aqueous solvent. For very small particles (less than 15 nm), the Brust-Schiffrin method is more common because of the lower polydispersity and better control over the reaction than Frens' method.[25] The downside of the Brust method is that the particles are synthesized in organic solvent, and so must be somehow phase-transferred into water. The general framework for water solubilizing hydrophobic gold particles is much the same as it is for QDs.

2.5.2 Raman scattering and enhancement

Raman scattering is the inelastic scattering of light by molecules. Incident light causes the molecule to enter a virtual energy state corresponding to a vibrational mode, from which it later returns to a lower energy state. If the molecule returns to the original state, the scattered light will have the same energy as the incident light (Rayleigh scatter). If the molecule returns to a higher or lower energy state, then the scattered light will have lower or higher energy than the incident light (anti-Stokes and Stokes scatter, respectively). Raman scatter differs from fluorescence in that it involves a virtual energy state (and so does not require a specific wavelength of excitation light) and is a coherent process. The Raman effect is named for its discoverer, Chandrasekhara Venkata Raman, who in 1928 measured it in sea water with the assistance of Kariamanickam Srinivasa Krishnan.[203] Raman scattering is

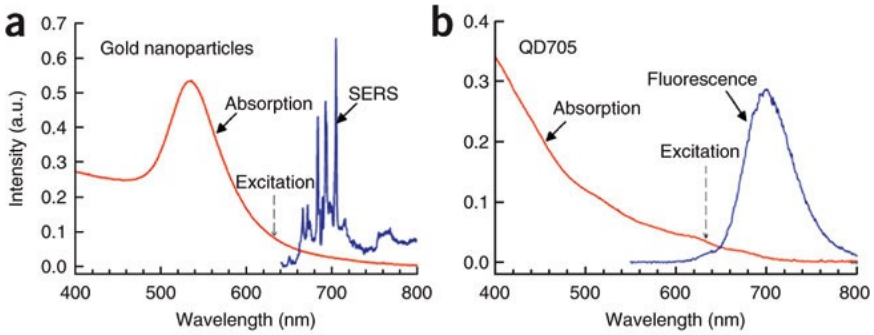

Figure 13: The Raman emission spectrum is feature-rich in comparison to the Gaussian-like emission of quantum dots (QDs). The absorption and emission spectra of Raman-active gold nanoparticles (A) and QDs (B) are shown. The Raman-active particles have a feature-rich spectrum compared to the broad emission spectra of QDs (which are themselves narrower than comparable fluorescent dyes). The gold nanoparticles also have a surface plasmon resonance absorption peak closer to the near-infrared window, a spectral region desirable for *in vivo* imaging. Reprinted by permission from Macmillan Publishers Ltd: Nature Biotechnology ref. [202], copyright 2008.

"feeble" (in Raman's words) and is difficult to detect.[1] Powerful monochromatic lasers, sharp optical filters, and amplified detectors have made Raman spectroscopy possible with small bench-top instruments. Raman spectroscopy has numerous applications in molecular fingerprinting because it elucidates molecular structure. The discovery of surface-enhanced Raman scattering (SERS) made Raman even more practical and introduced new applications of Raman spectroscopy.

SERS was discovered by Fleischman *et al.* in 1974 in an electrochemical cell experiment; they discovered that the Raman scatter from pyridine was greatly enhanced on roughened silver electrodes.[78] Later, in 1977, two competing theories were advanced to explain the SERS enhancement: Jeanmaire and Van Duyne proposed an electromagnetic enhancement (arising from plasmon oscillations on the roughened surface);[120] Albrecht and Creighton proposed an enhancement arising from charge-transfer complexes.[6] Both theories are still debated today. In 1997, Emory and Nie showed that the enhancement

[1]The Raman effect is so weak that in Raman's original experiment, sunlight focused with an 18 cm diameter telescope required multiple hour exposures on photographic plates to detect the Raman-scattered light.

factor for SERS using silver nanoparticles could be as high as 10^{14}–10^{15}![182] Such an enhancement factor is sufficient to detect the Raman scatter of a single molecule. Porter and coworkers later used SERS enhancement from gold particles with an adsorbed Raman reporter in an immunoassay;[143] Qian *et al.* described a superior strategy featuring a heavily PEGylated gold nanoparticle, functionalized with Raman reporters, that is highly stable in biological fluids and bright enough to be observed through the skin of an animal.[202] The greatest advantage of SERS particles for biological applications is that the Raman effect works on any wavelength of light, so deeply-penetrating NIR light can be used for excitation and the Stokes-scattered light will also be within the NIR range. SERS particles are also extremely bright and photostable when using NIR excitation (more so than QDs, as reported by Qian *et al.*). Finally, gold nanoparticles are regarded as "non-toxic", having a history of medicinal use to relieve symptoms of rheumatoid arthritis. As shown in Figure 13 on the previous page, SERS particles have a feature-rich emission spectrum when compared to the near-Gaussian emission of QDs or the broad emission of fluorescent dyes—the feature-rich spectrum can be advantageous for multiplexing.

2.6 Application of nanotechnology to cancer imaging and therapy

The U.S. National Institutes of Health, recognizing the potential of nanotechnology for cancer diagnostics and therapy, launched an "Alliance for Nanotechnology in Cancer" through the National Cancer Institute in 2004. This effort has catalyzed the development of a wide variety and number of nanotechnologies targeting cancer (including supporting some of the work appearing in this dissertation).

For diagnostics, nanotechnology can provide improved imaging agents that have greater sensitivity and specificity than conventional agents. For example, iron oxide becomes superparamagnetic (magnetic only in the presence of an applied magnetic field) when reduced in size down to a single magnetic domain. These iron oxide nanoparticles (called SPIONs, MIONs, CLIO, *&c.*) are useful as a magnetic resonance (MR) imaging contrast agent.

They can also be functionalized with fluorescent dyes or chelating functional groups: such dual-functionality particles can be used for combined MR/fluorescence and MR/positron emission tomography.[130, 124, 89] QDs and colloidal gold (both for LSPR imaging and SERS imaging) are useful for sensitive immunohistochemistry of tissue samples. Since cancer is a heterogenous disease, the ability to probe multiple cancer markers simultaneously is important. As discussed *supra*, both QDs and SERS nanoparticles are useful for multiplexed imaging. Nanoscale gold is also more reactive than bulk gold—this reactivity can be combined with silver enhancement for sensitive diagnostic assays.[246]

Nanotechnology is useful for cancer therapy as well. Standard chemotherapeutics like paclitaxel and doxorubicin have a number of undesirable side effects, some due the excipients needed to solubilize the chemotherapeutic (*e.g.,* the ethanol and polyethoxylated castor oil used for taxanes), some due to the compound mode of action itself (*e.g.,* cardiomyopathy for doxorubicin, ototoxicity for cisplatin). Using nanotechnology to create carriers for chemotherapeutics can overcome these problems. Nanocarriers can be targeted such that the carriers preferentially accumulate within tumors. The circulation time of the drug and release of the cargo can also be carefully tailored so that the drug is more likely to release inside a cancer cell. Already, several nano drugs are FDA-approved (*e.g.,* Doxil, liposomal doxorubicin; Abraxane, albumin-encapsulated taxol) and many more are in clinical trials (24 reported in 2008).[277] These first-generation drugs rely on a passive accumulation mechanism described *infra*. Abraxane is also reported to take advantage of active albumin transport.[97] A large research effort is also in developing "active targeting" drugs that bind to specific cancer targets, further increasing specificity of the drug and reducing off-target effects.[250, 251] Finally, nanotechnology can be used to destroy cancer without using chemotherapeutics, overcoming drug resistence. As noted earlier, colloidal gold can be used as a photothermal sensitizer, causing localized heating that destroys cancer. Likewise, magnetic nanoparticles can be used as a radiofrequency ablation sensitizer, which also produces localized heating.[155, 105]

2.6.1 The enhanced permeability and retention effect

The "enhanced permeability and retention" (EPR) effect is the observation that tumors tend to have a poorly-defined vascular support network and that colloids will tend to extravasate and accumulate in these areas more so than in normal tissue.[152, 117, 276, 119, 118, 85] As was discussed in Chapter 1, one of the hallmarks of cancer is the ability to promote the formation of neovasculature (angiogenesis). This neovascultare is required to supply the rapidly growing tumor with nutrients—without the neovasculature, the tumor cannot grow larger than a few hundred microns in diameter. The rapid and disorderly growth of tumors prevents the development of a proper and mature vasculature and lymphatics within the tumor. As a result, the tumor has a "leaky" vasculature that permits extravasation of macromolecules combined with poor lymphatic drainage that can clear these macromolecules out of the tumor. This is the mechanism behind the EPR effect. Particles in the 20–200 nm size range are well-positioned to exploit the EPR effect to accumulate within tumors more than within normal tissue. The leakiness of tumor vasculature is not unique in the body: inflamed tissues also have increased vascular permeability (of course, an inflammatory component is also associated with tumors), as do recently injured areas (*e.g.,* an incisional biopsy site). These areas would also be expected to accumulate macromolecules by the EPR effect.

2.7 Toxicity associated with nanoparticles

Toxicity associated with nanoparticles is a concern.[185, 75, 260, 240, 156, 282, 61] It is important to note that while the nanoparticles discussed in this work are man-made, there are many examples of naturally-occurring nanoparticles. For example, the soot from a dirty fire has a mixture of carbon fullerenes, and fullerenes have been found in prehistoric mineral deposits.[35, 26] Since nanoparticles can be found in nature, it is reasonable to assume that there are some biological responses evolved to handle nanoparticle exposure. There have been numerous studies of the toxicity associated with particulate inhalation,

some of which examined particles in the submicron regime.[136, 61] Nanotoxicology examines many effects that can cause toxicity: colloidal toxicity, the toxicity of the particles themselves (often linked to the relatively high surface area of nanoparticles); elemental toxicity, the toxicity associated with the material making up the particle; and also considering biopersistence, the tendency of the particles to remain in the organism. The exposure route is also important: nanoparticles have been shown to cross the skin, lung endothelium, intestinal tract, and even translocate along neural tracts.[106, 167, 214, 31, 186, 69]

Of the nanoparticles addressed in this dissertation, QDs receive the greater scrutiny for toxicity. Much of the discussion centers on the elemental composition of the QDs. As discussed *supra*, the utility of a QD is that the band gap of the particle, and so the fluorescence emission wavelength, can be tuned by altering the size of the structure. Additionally, the composition of the structure can also be altered to change the band gap. The problem is that the materials with a band gap that results in useful biological imaging (visual to NIR range) are toxic in elemental form. The group IV-VI QDs used for biological imaging are commonly made from cadmium, selenium, and tellurium; cadmium and tellurium are both highly toxic, and selenium, while a necessary trace element, is toxic in the moderate quantities. Other materials commonly used for QDs include lead, mercury, arsenic, and indium. All of these elements cause nephrotoxicity, among other problems.[14, 59] There have been efforts to make "doped dots", zinc-based quantum dots that use a dopant of manganese or copper as a fluorescence recombination site, but these QDs have inferior optical properties in comparison to the traditional, heavy-metal containing QDs.[270, 200] The toxic composition of QDs may not directly translate to organism toxicity: while the components are known toxins, the toxicity of the elements in the form of a nanocrystal are unknown. Many studies have attempted to find out if QDs will degrade in biological systems, leading to exposure to heavy metal ions. Hardman reviewed the toxicology literature pertaining to QDs in 2006 and found that there was no clear consensus on the toxicity of QDs.[95] Partly, this is because of the lack of the differences in QDs used by the laboratories doing toxicity

research. Some cell model studies have shown some signs of short-term toxicity, but in these cases the particles tend to be types known to be colloidally and chemically unstable during the time course of the experiment (oftentimes CdTe nanoparticles synthesized in aqueous solution).[226, 279, 147, 278] Cellular studies using more stable core/shell QDs with thick polymer shells, the type more likely to be used *in vivo*, do not show short-term toxicity.[56] More recent long-term studies of QDs in animal models has shown no overt toxicity effects.[77, 96, 141] Biopersistence is also problematic: heavy metal-containing QDs that remain in the mononuclear phagocyte system (MPS) (liver, spleen, kidneys) for years are more of a concern than QDs that are rapidly eliminated from the body. In general, QDs (and nanoparticles in general) that are systemically injected are found in the MPS and persist.[199, 4, 39, 221, 137, 138, 76, 13] Designing QDs to be rapidly eliminated from the body is one way to address issues of toxicity. Choi *et al.* designed QDs to be efficiently excreted in the urine, addressing this problem.[40]

Gold colloids do not share the toxicity concerns of QDs, and this is known in part because of a history of use in human medicine as an anti-inflammatory therapy. Gold leaf is used as a decoration on foods and in drinks, and can be consumed without deleterious effects (*e.g.,* gold flakes in Goldschläger). The response of cells to gold nanoparticles is known to be size and surface-coating dependent.[122] Small gold clusters (*i.e.,* 1.4 nm in diameter) show severe toxicity effects, presumably due to the reactive nature of gold at that scale;[191] in contrast, the size and particle coating used for SERS tags (approximately 60 nm gold core diameter, 80 nm total hydrodynamic radius) shows no obvious toxicity problems.[202, 236, 53] Bulk gold is known for corrosion resistance (famously requiring *aqua regia*, “royal water”, for dissolution), and so it is unlikely that the body can degrade gold colloid. Small gold particles, below the renal excretion threshold, are eliminated in the urine; there are also reports that larger particles can be eliminated through the feces.[38, 216]

2.8 Conclusions

Nanotechnology is a disruptive and transformative technology because it permits fine-grained control over materials to expose properties that are unavailable in bulk form. The application of nanotechnology to cancer diagnostics and therapy is but one promising area where nanotechnology can make drastic improvements. Semiconductor quantum dots as a class of nanoparticles received early attention as biological labels primarily because of the superior optical properties when compared to existing fluorescent labels. There are many applications where the superior photobrightness and photostability of quantum dots, in addition to facile multiplexing, have enabled scientific investigations that would not be possible or practical with conventional fluorophores. Gold nanoparticles have also shown promise as labels (both through light scattering and as enhancers of Raman scattering) and photothermal sensitizers. For both of these types of nanoparticles, toxicity has been a concern (as with all nanotechnology). Early nanotoxicology studies have in some cases provided conflicting results, but as nanotoxicology as a field becomes mature, a consistent picture will emerge.

CHAPTER III

INSTRUMENTATION FOR GUIDING CANCER SURGERY

3.1 Abstract

Surgery is an effective treatment for a wide range of tumors. Generally speaking, complete removal of a tumor produces a cure. Producing "clean" surgical margins (i.e., no residual tumor within the surgical cavity) requires removal of small adjacent sites of tumor and nearby metastatic lymph nodes. Complete tumor removal as confirmed by post-operative pathology is prognostic of a good surgical outcome. Nevertheless, in a large number of cases, the surgeon cannot establish during the surgical procedure whether complete tumor removal has been accomplished. Technology to improve the ability of a surgeon to intraoperatively and in real-time determine the extent of a tumor and the status of tumor removal would be expected to dramatically improve patient care. In this chapter, we describe an instrumentation platform technology that combines point spectroscopy and widefield imaging for intraoperative surgical guidance using exogenous contrast agents. This platform has been implemented as a prototype and is presented here for characterization and validation.

3.2 Introduction

Surgery is an effective tool in treating cancer. It is intuitive that if a tumor could be resected (physically removed), leaving no tumor behind, that the patient could be cured. It has been reported that surgery alone can, in fact, be curative in approximately 45% of cases.[52] In practice, effecting a complete cure through surgery alone is challenging. While in the operating theater, a practicing surgeon is guided primarily by sight and palpation in locating and removing a tumor. Preoperative imaging is used for diagnosing a tumor, but preoperative

imaging is not useful during the surgical procedure. The surgical procedure itself distorts the body, due to differences in tissue locations (*e.g.,* deflating a lung, moving organs while searching the mesenteries for a lymph node) between preoperative imaging and surgical procedures, as well as the distortion of removing tissue! Tumor boundaries are often ill defined, both in gross appearance and histologically. Simply finding the tumor boundaries in these cases can pose a challenge, especially if the tumor is small or invasive. Relying on senses alone also limits the size of the tumor that can be located. If the tumor is not completely resected, either because the surgical margin (resection boundary) contains tumor or because there were undetected small satellite tumors not contiguous with the main mass, then the patient's prognosis worsens.[242, 1] Following surgery, the area operated on will develop scar tissue because of the local trauma delivered during the surgical procedure. This scar tissue is dense and fibrotic, and makes it difficult or impossible to differentiate from residual tumor on palpation or visual inspection. Because it is difficult to determine the extent of neoplasia in a scarred area, a scar revision surgery (a follow up surgery to remove residual disease) removes the entire scarred area. As can be imagined, this is not always practical because would closure requires a minimum amount of tissue. The difficulty in effecting a complete cure through surgery is why surgery is usually combined with postoperative chemotherapy or radiation therapy.[283, 42, 123, 237, 110, 228, 266]

The desire to effect a complete cure through surgery (and thus avoid chemotherapy or radiation therapy) drives interest in intraoperative guidance. Previously, both MR imaging and sonography have been investigated for providing intraoperative guidance.[204, 179] Intraoperative MR is cost-prohibitive, bulky, time-consuming, and technically involved to use in the operating room. In addition to precluding the use of metallic tools, the patient must be physically moved to the MR scanner while making sure that the patient remains intubated, intravenous lines remain in place, and sterility is maintained. Once at the MR scanner, the patient must then undergo a lengthy imaging sequence, at which point the patient is moved back to the procedure area. Any time added to the surgical procedure

greatly increases costs and risk to the patient due to anesthesia. Intraoperative sonography is promising, but it has limited spatial sensitivity and the ultrasound beam can be blocked by bone. Both scintigraphy and intraoperative computed tomography (CT) are available for intraoperative guidance, but both expose the patient and operators to radiation. The radiation dose from CT scans of patients through conventional medical practices is already a concern;[51] increasing the dose through repeated intraoperative imaging scans is obviously undesirable and would be avoided if an alternative existed. It can also be argued at both MR and CT are not real-time technologies since the patient cannot be worked on during the imaging sequence. Beyond imaging, there is a limited time window in which to conduct intraoperative pathology, limited again by the time the patient must be under general anesthesia and by the availability of attending pathologists. Intraoperative pathology is done by frozen sectioning, which is labor intensive, or by touch preparation, which is insensitive and operator dependent. A technique that avoids using ionizing radiation and is real-time, has good spatial sensitivity, and uses compact equipment, would be welcomed in the operating room.

In this chapter, we describe intraoperative imaging instrumentation that can be combined into an integrated system. One instrument, the "SpectroPen", is a hand-held spectrometer; the other instrument is a widefield imaging head designed to sit overtop the surgical field. Spectroscopy systems for medical applications have been described previously, but these systems typically rely on intrinsic biological signals (*e.g.,* intrinsic Raman or cellular organelle scattering).[150, 170, 171, 281] Normal patient-to-patient variability means that the intrinsic signals between normal and abnormal will vary between patients.[140] Using an exogenous agent that preferentially accumulates within abnormal tissue to provide contrast overcomes patient-to-patient variability. Thus, we have optimized this instrumentation to work with fluorescent dyes (one of which is FDA-approved for human use) and SERS nanoparticles. Widefield imaging has been applied to intraoperative surgical guidance, but previous schemes have used wide area illumination.[252, 224, 225, 206, 52, 180]

Using wide area illumination requires powerful illumination sources to provide sufficient excitation irradiance.[88] These high power light sources raise safety concerns (*e.g.,* high power lasers, high voltage sources) and color the operative field, distracting the surgeon.[252] In contrast, we use the local excitation from the SpectroPen for widefield imaging, overcoming the limitations of wide area illumination. While each individual instrument has been described in the literature previously, combining the two is novel. In this chapter, we describe the design and validation of the instruments; in Chapter 4, we provide examples of the system in use for intraoperative guidance.

3.3 Methods

3.3.1 Contrast agents

Indocyanine green (ICG) was diluted into phosphate-buffered saline (PBS) containing 4% (w/v) of bovine serum albumin (BSA), similar to the concentration of serum albumins in human blood.

Surface-enhanced Raman scattering (SERS) nanoparticles were encoded with the Raman reporting dye 3,3'-diethylthiatricarbocyanine (DTTC), and the resulting particle was called DTTC-SERS. The procedure used was from Qian *et al.*[202] DTTC at 4 μmol/L in PBS was added to 60 nm gold colloid from a commercial supplier such that there were approximately 2×10^4 DTTC molecules per gold nanoparticle. Gold nanoparticle concentration was estimated from ultraviolet-visible (UV-vis) spectroscopy of the surface plasmon resonance peak.[91] Once encoded with DTTC, the gold particles were mixed with an excess of a 10 μmol/L solution of 5k PEG-SH (5000 MW polyethylene glycol-thiol) solution and purified by repeated centrifugation and resuspension in a bench top microcentrifuge.

3.3.2 Local excitation and spectroscopy ("SpectroPen")

3.3.2.1 Design and construction

A commercial off-the-shelf fiber-coupled Raman spectrometer remote head was coupled to a commercial off-the-shelf bench-top Raman spectrograph. The excitation fiber to the

remote head was directly coupled to a pig-tailed laser diode in the spectrograph. The collection fiber from the remote head was placed at the entrance to the spectrograph.

3.3.2.2 Validation

Unless otherwise noted, all experiments placed the SpectroPen head 1 cm from the inspected area.

The SpectroPen was compared to a commercial bench-top Raman spectrograph by recording the Raman spectra of polystyrene without background subtraction. The spectra were normalized to the 1001.4 cm^{-1}peak for comparison.

To test the the detection of ICG and DTTC-SERS in porcine fat, the contrast agents were diluted to 2 nmol/L and 20 pmol/L respectively to record pure spectra in PBS. Porcine fat was then incubated in ICG at 650 nmol/L and DTTC-SERS at 300 pmol/L, both in PBS, to saturate with contrast agent for the mixed signal case. The background signal was recorded from porcine fat not mixed with contrast agent. To generate a reference background spectra for subtraction, a spectra of 4 points was acquired from normal tissue and averaged. The background averaged spectra was linearly subtracted from the mixed contrast agent and fat signal or background signal to recover the contrast agent or background signals, respectively.

To measure the limit of detection for the SpectroPen, ICG or DTTC-SERS were diluted in a black 96-well microtiter plate. ICG was diluted within the range of 0.05–25 nmol/L, DTTC-SERS nanoparticles were diluted within the range of 0.2–37.6 pmol/L. 4 samples were measured for each indicated concentration. Lines of fit were a least-squares linear regression.

The depth of penetration for the SpectroPen in detecting contrast agents was measured by soaking 8 mm^3 tissue in the contrast agent, either 650 nmol/L ICG or 300 pmol/L DTTC-SERS in PBS. The tissue was placed underneath the SpectroPen and covered with a layer of polyvinylidine chloride “plastic wrap”. Thin slices of tissue were then overlain

on top. The distance between the SpectroPen and top-most tissue surface was maintained at 1 cm.

3.3.3 Widefield imaging head

3.3.3.1 Design and construction

A commercial off-the-shelf C-mount lens designed for broadband imaging between 400–1000 nm with a 35 mm focal length and $f/1.9$ maximum aperture was used as a common objective. Lens layout to extend the focal length and collimate the light from the common objective was done through a commercial computer software package. The commercial objective was modeled as a perfect lens as no lens prescription was available. Design goals were for a 45 cm object distance, 5 cm object height, a 1/2 inch diagonal camera sensor for the imaging plane, and a collimated light path for filtering. The optimized field lens design to extend the objective lens used a convex lens with focal length of 60 mm, a positive meniscus lens with focal length 100mm, and a biconcave lens with focal length of -50 mm; an achromatic doublet with focal length of 45 mm was used for collimation. The field lens group and collimating lens were coated with a magnesium fluoride (MgF_2) antireflection layer optimized for 700–1000 nm. The common objective, field lenses, and collimating lens were mounted in a single lens tube, in that order. The light from the objective lens group was then folded 90 degrees by a protected silver mirror. Two dichroic mirrors were mounted sequentially in the collimated light path using kinetic mirror mounts. The first dichroic encountered is a short-pass dichroic mirror with a center wavelength cut-on of 800 nm and mounted at a 45 degree angle to the collimated light path. The reflected light is filtered through a rugate notch filter centered at 785 nm to reject Rayleigh scattered laser light and a bandpass filter with center wavelength of 820 nm and a 25 nm bandwidth. The light is then focused onto the 1/2 inch camera sensor. This is the NIR channel. The filters, lens, and camera were mounted onto a common lens tube in that order. The next dichroic mirror encountered is a short-pass with a center wavelength of 700 nm and mounted at a 45

degree angle to the collimated light path, and 90 degrees relative to the first dichroic. The reflected light from this dichroic is filtered through an absorptive neutral density filter with optical density 2 and coated with an MgF_2 antireflection layer optimized for 700–1000 nm. The attenuated light is then focused onto the 1/2 inch camera sensor. The filter, lens, and camera were mounted onto a common lens tube in that order. This is the laser tracking channel. The remaining collimated light transmitted through both dichroics is the color anatomic view, and is directly used for the color camera. For all 3 channels, the light is focused onto the camera sensor using an achromatic doublet with a focal length of 45 mm; the NIR and laser channels have lenses coated with an MgF_2 antireflection layer optimized for 700–1000 nm, the color channel is coated with an MgF_2 antireflection layer optimized for 400–700 nm. A detailed listing of the optical prescription appears in Appendix B. All lenses, mirrors, and filters are 25.4 mm in diameter. All lens tubes (containing the lenses and attached cameras) were mounted in slip rings, and these and the other optical parts were mounted onto a breadboard using standard opto-mechanics parts. The cameras selected are 1/2 inch uncooled and interlaced silicon CCD sensors with good NIR quantum efficiency (QE). The cameras are connected by Firewire 400 interface to the computer. Sensor resolution is 768×492, with a pixel size of $8.4\ \mu m \times 9.8\ \mu m$. The sensors used for each channel are the same, however the color channel has a Bayer mosaic filter to provide color imaging, and the NIR and laser channel cameras have no NIR light filter in place. Overall QE is reported to be 47% at 800 nm for the camera sensor, as reported by the manufacturer. Illumination of the surgical field was provided by two consumer white-LED lamps, 40 W each.

The widefield imaging software was written in the C-sharp programming language. The program uses an application programming interface (API) provided by the camera vendor. The program is multithreaded: each camera channel acquires frames in a separate programming thread. The acquisition thread for the NIR frame thresholds the image at a user-specified level to create a binary mask of NIR probe signal each time a frame is

acquired. The acquisition thread for the laser tracking channel thresholds the image at a user-specified level to create a binary mask of the laser position. This centroid of the positive area in the mask is then calculated, along with the diameter of the area. The NIR probe mask frame, as well as the laser position information, are acquired by the color channel thread each frame of the color channel to create the composite view. The composite frame is the sum of the NIR frame mask (with a cyan false-color applied) and a circle at the laser centroid and with the laser diameter overlain using the camera vendor API. Additional video signal processing can be enabled by the system operator and is processed during the overlay generation. One processing mode, called "virtual phosphorescence" (VP), adds a delay time to any NIR signal selected for video overlay. When the user elects to use the VP filter, an accumulation buffer is initialized. As each new frame is acquired by the NIR camera process, the accumulation buffer is multiplied by a decaying exponential function. The decay constant is user set, and is defined by the amount of time the user would like the display to persist. The decay constant is found by solving the equation

$$I(t) = I(0) \cdot e^{-D \cdot t} \tag{3}$$

where I is the pixel intensity in the frame, $I(t)$ is the new pixel intensity at the given time index, e is the base of the natural logarithms, D is the decay constant, and t is the time index. The equation is solved for D and parameterized for the decay time $\tau = t$, using 255 and 1 as the values for $I(0)$ and $I(\tau)$, respectively,

$$D(\tau) = -\frac{\ln[I(\tau)/I(0)]}{\tau} = -\frac{\ln[1/255]}{\tau} \tag{4}$$

Applying the decay ("aging" the accumulation buffer) is then done by multiplying every pixel in the accumulation buffer by

$$I(s+1) = I(s) * \exp(-D(\tau) * \Delta s) \tag{5}$$

where s is discrete time (between frames), $I(s+1)$ and $I(s)$ are respectively the new and old values of the intensity at the given pixel, exp() is the exponential function, $D(\tau)$ is the decay constant calculated in Eq. (4), and Δs is the time between frames (*i.e.,* frame interval).

The software is able to record still images or live video (with MPEG-4 compression) for documentation (without the effects of overlays or video filters applied), as well as metadata about the experiment (*e.g.,* mouse tumor model used, contrast agent dose and type) in a plain text file. A pseudocode description of the software appears in Appendix C.

3.3.3.2 Validation

The minimum resolvable contrast of the imaging head was measured using the USAF-1951 test pattern, finding the smallest line pairing that could be resolved by line profile measurement compared to half the value of the square target. Each element, E, of each group, G, of the USAF-1951 chart has an associated resolution of

$$\text{Resolution (lp/mm)} = 2^{G+(E-1)/6} \tag{6}$$

Eq. (6) was used to find the resolution of the smallest element with line pairs that could still be resolved based on visual inspection.

The modulation transfer function (MTF) of the optical system was calculated from an image of a slanted knife-edge at a 5 degree angle. The image of the knife-edge was profiled to create a line spread function. The line spread function was transformed to the frequency domain through a discrete Fourier transform to generate the MTF.

For limit of detection test, ICG was diluted into a 5% (w/v) tissue homogenate of a murine tumor model (described further in Chapter 4, Section 4.3.2.1). The ICG fluorescence was recorded by placing the SpectroPen at an angle such that the sample, in a glass vial, was visible by the widefield imaging head. The NIR images recorded of the sample vial were analyzed by dosimetry: the area of the vial was selected, and the sum of values in the image was recorded to find the integrated fluorescence over the sample volume. 3 samples were recorded for each data point, ranging from 0.15 nmol/L ICG to 15 nmol/L ICG. The data were analyzed by linear regression.

3.4 Results and discussion

3.4.1 Local excitation and spectroscopy ("SpectroPen")

3.4.1.1 Design and construction

To make spectroscopic readings possible in an operating room environment, the spectrometer needs to be rugged, compact, ergonomic, and simple to use. The hand-held spectrograph our group has designed, which we call the "SpectroPen", is based off of commercially available parts and meets the above requirements and is pictured in Figure 14 on the following page. The imaging head is a hand-held probe designed for Raman spectroscopy. Although compact, is is a sophisticated design. The body is stainless steel, 12.7 mm in diameter, and 76 mm long. The hand-held unit is fiber-coupled to a spectrometer by a co-linear fiber design. The excitation fiber light is collimated before passing through a band-pass filter for cleanup and through a dichroic mirror into a common focusing lens. Emitted light from the sample is collected by the common focusing lens, reflected by the dichroic mirror and passes through a long-pass filter to reject reflected laser light. The emitted light is then focused into a return emission fiber. The co-linear fiber arrangement attenuates Rayleigh scatter return by 10^8 because it filters light in both the excitation light before it is directed to the sample and the emission light before it enters the collection fiber.[29, 30] The current head unit has a focal length of 0.5 cm with a 100 micron diameter spot size and is designed for 785 nm excitation light. The head unit is fiber-coupled through a 5 m fiber-optic cable into a commercial bench top Raman spectrograph. Excitation light is provided by a 100 mW pig-tailed laser diode in the spectrograph, and the emission fiber is coupled to the instrument at the entrance to the spectrograph. The spectrograph design uses a fixed grating. The SpectroPen was compared against a commercial bench-top spectrograph of the same type used as the basis for the SpectroPen in Figure 15 on page 52. The performance of the two instruments at equal integration times is similar. Both instruments perform well in distinguishing between the close polystyrene peaks at 1001.4 and 1031.8 cm^{-1}. The SpectroPen shows slight attenuation in the higher wavenumber region, but this is balanced

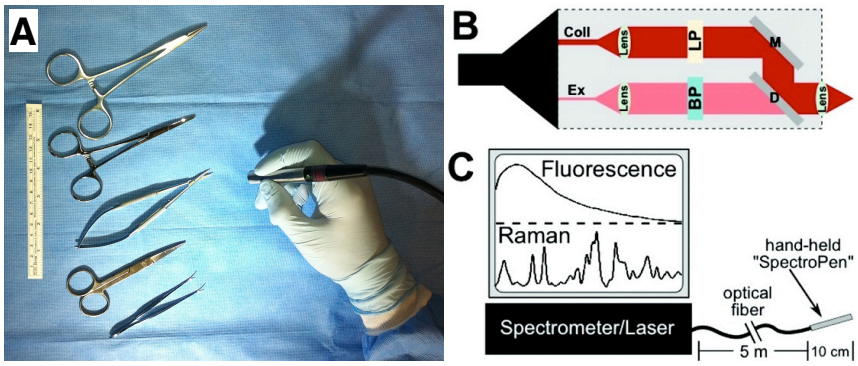

Figure 14: The "SpectroPen" hand-held Raman spectrometer. (A) The SpectroPen being held next to common surgical tools. (B) The optical layout inside the SpectroPen head unit: there are two fibers, one for excitation (Ex) and one for collected emission light (Em), coupled through a series of band-pass filters (BP), long-pass filters (LP), dichroic mirrors (D), and reflective mirrors (M). The current implementation couples the SpectroPen head unit through 5 m of cable, terminating in the spectrometer proper as shown in (C). Panels (B) and (C) are adapted in part with permission from ref. [166]. Copyright 2010 American Chemical Society.

by slightly greater sensitivity in the lower wavenumber region. For fluorescence, the lower wavenumber region closer to the excitation light is more important, whereas for Raman, the higher wavenumber region (the fingerprint region) is more important.

3.4.1.2 Validation

We next measured the ability of the SpectroPen to measure indocyanine green (ICG), a Food and Drug Administration (FDA) approved contrast agent. The ICG optical properties change greatly depending on solvent and the presence of solutes, but the properties have been exhaustively characterized.[198] In pure water, the absorption and emission maxima of ICG (780 nm/800 nm) are well matched to the SpectroPen excitation laser and spectrograph operating range (800–930 nm). When bound to albumin (as would happen on systemic injection of ICG), both values redshift by approximately 10 nm. Since the SpectroPen is designed for *in vivo* applications, we tested the ability of the SpectroPen to detect ICG fluorescence or Raman scattering from surface-enhanced Raman scattering gold nanoparticles, encoded with 3,3'-diethylthiatricarbocyanine (DTTC) as a Raman reporter.

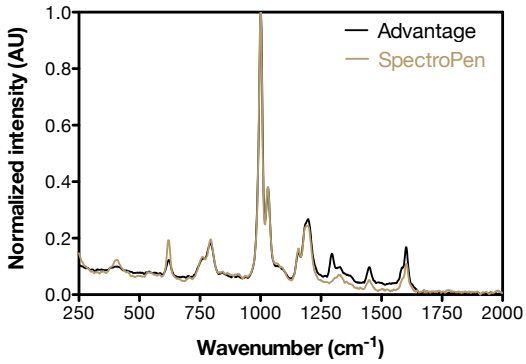

Figure 15: The "SpectroPen" recorded spectra match with those recorded by conventional spectrometers. Raw Raman spectra from polystyrene were recorded on both the SpectroPen and a standard, commercial bench-top Raman spectrograph. The spectra were normalized to the major peak of polystyrene at 1001.4 cm^{-1}. The spectra recorded are similar, with only slight differences in recorded intensity but identical peak locations.

As shown in Figure 16 on the following page, both ICG and DTTC-SERS are readily detectable by the SpectroPen when in pure solution or when mixed with porcine fat. Interestingly, fat itself has Raman features that are easy to detect. Simple linear subtraction of an averaged background signal are able in this experiment to restore the original spectra of ICG and DTTC-SERS. Subtracting the averaged background signal from pure porcine fat results in what is essentially noise, validating this background subtraction method.

We then tested the linearity of the SpectroPen in measuring both ICG and DTTC-SERS nanoparticles in pure solution at two integration times (0.1 and 1 second) that are clinically useful. The SpectroPen is able to detect both ICG and DTTC-SERS, at both integration times, with a linear response as shown in Figure 17 on page 54. The response encompasses a 50–60 fold dynamic range. Typically for imaging contrast agents, there is a contrast ratio of less than 5 between the background and contrast-enhanced regions.[83] Thus, the instrument is well-positioned to detect both normal tissue background and any contrast agent likely to be used in the near future under the same instrument settings.

A difficulty in using light for medical imaging is that the penetration depth in tissue is limited due to absorption and scatter. Using NIR light mitigates these problems. For

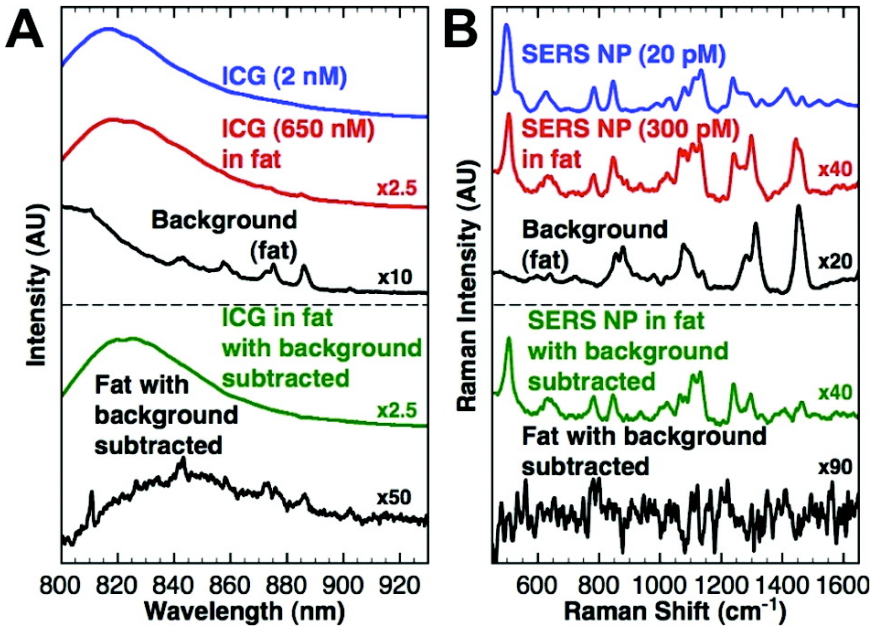

Figure 16: Indocyanine green (ICG) and Raman (SERS) nanoparticles can be distinguished from the biological background. Spectra of ICG (A) or SERS nanoparticles (B) were recorded alone or mixed with porcine fat. Using the pure porcine fat spectra, the original probe spectra could be recovered. Spectra are scaled by the noted scaling factors. Reprinted with permission from ref. [166]. Copyright 2010 American Chemical Society.

surgical applications, surface imaging is tolerable because organs and tissues can be mechanically moved out of the way to image deeper, and for surgical oncology, it is the margin status (by definition on the surface) that is of concern. We quantified the ability of the SpectroPen to detect both ICG and DTTC-SERS contrast agents underneath porcine fat, liver, and lung. As shown in Figure 18 on page 55, for all cases DTTC-SERS nanoparticles can be detected deeper in tissue than ICG. One reason the DTTC-SERS nanoparticles can be detected deeper in tissue might be because DTTC has strong Raman peaks Stokes-shifted from the laser excitation line, whereas the ICG emission peak is close to the laser excitation line. The bathochromic infrared light of the DTTC Raman peaks relative to ICG will scatter less in tissue and so will be slightly deeper penetrating. The feature-rich emission from SERS tags also increases the ability to pick out the Raman signature from the background. These data show ICG has a detection depth limit of 1–3 mm in tissue, whereas DTTC-SERS nanoparticles have a detection depth limit of approximately 5–7 mm

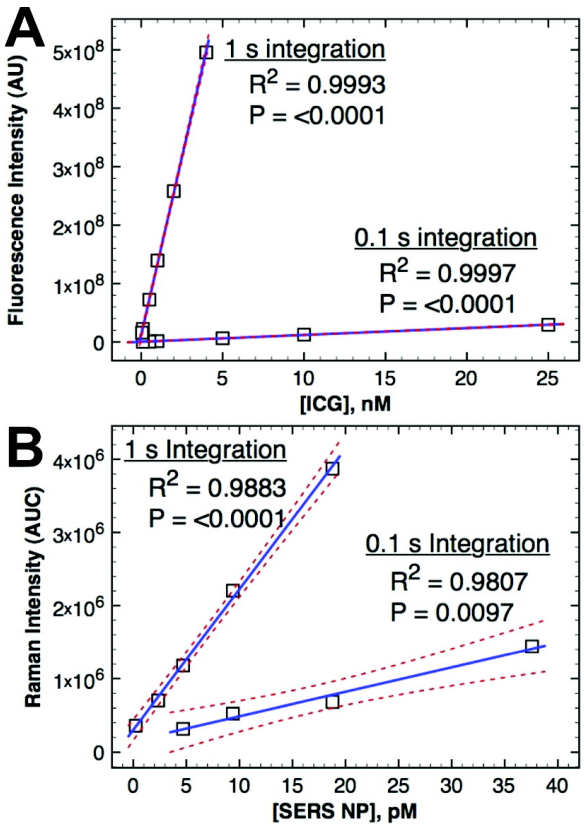

Figure 17: Limit of detection for the "SpectroPen"for both indocyanine green (ICG) and surface-enhanced Raman scattering (SERS) particles. For the tested integration times of 0.1 or 1 second, the SpectroPen response is linear. Regression lines are a linear model, with the 95% confidence interval for the fit shown in flanking red dashed lines. Reprinted with permission from ref. [166]. Copyright 2010 American Chemical Society.

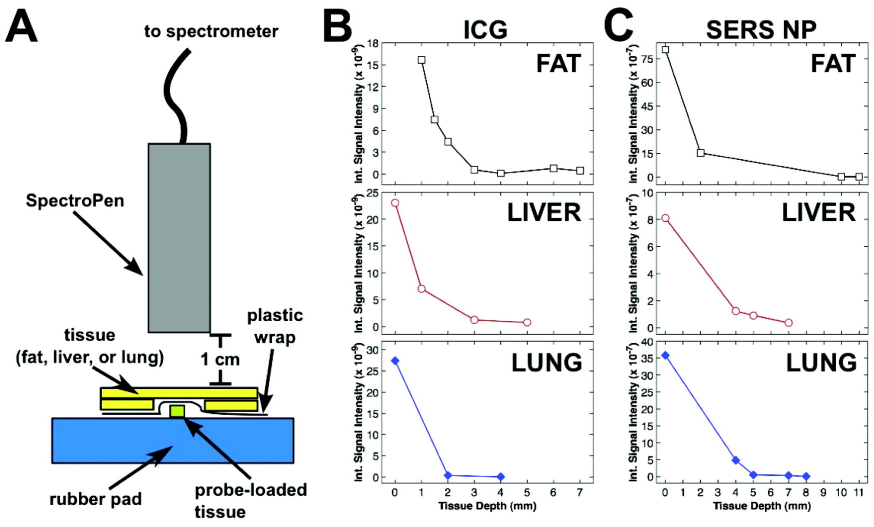

Figure 18: Depth of penetration of "SpectroPen" for detecting indocyanine green (ICG) and Raman (SERS) nanoparticles underneath tissue. (A) The experimental setup for determining the depth of penetration for the SpectroPen to detect ICG or SERS nanoparticles deposited in tissue. The detected ICG (B) and SERS (C) signals obscured in tissues attenuate as a function of the probe depth in tissue in an exponential-like decay. Reprinted with permission from ref. [166]. Copyright 2010 American Chemical Society.

in tissue.

3.4.2 Widefield imaging head

3.4.2.1 Design and construction

While the SpectroPen alone is sufficient for medical applications, using the SpectroPen requires the operator to reconcile the recorded spectra with locations on the patient. We originally sought to build a widefield imaging system for documentation while using the SpectroPen, but discovered that it made using the SpectroPen much more intuitive. The design was refined into a proof-of-concept prototype, and is shown in Figure 19 on page 57. Design priorities were for economy, NIR light sensitivity, simplicity, and imaging quality, in that order. The overall design fits on a 20×20 cm breadboard and weighs 2.75 kg. The optical bench is designed to be mounted upside down, such that the common objective lens is facing downwards over the surgical field. Support lenses mounted in lens tubes are used to extend the focal length of this lens and collimate the light for filtering, before refocusing it on one of 3 cameras: one each for imaging the surgical area, imaging the laser excitation

source from the SpectroPen, and imaging any emitted NIR light from the imaging field. A system of dichroic mirrors mounted within a collimated light path are used to direct the appropriate light ranges to each camera, and optical filters increase specificity. The cameras use uncooled, interlaced charge-coupled device (CCD) sensors with a hole-accumulation diode design that increases NIR light sensitivity (up to 47% quantum efficiency at 800 nm). The surgical area camera ("anatomic") uses a color camera, the other two channels are black and white. All 3 cameras use a Firewire computer interface for both power and data transfer, and all 3 cameras can be simultaneously imaged at 30 frames per second ("real-time"). The imaging head is sufficiently compact and light to be mounted onto a commercial computer display arm and computer cart designed for medical use. A simple light-tight enclosure was constructed of black polyoxymethylene for prototyping purposes; a glass UV filter for consumer cameras was used as a window for the common objective. The optical breadboard is attached to the enclosure by screws with rubber washers sitting in between the breadboard and enclosure for vibration dampening. The entire enclosure can then be mounted onto the display arm through drilled and tapped holes.

To handle data acquisition and image processing, we wrote a custom software program using application programming interfaces (APIs) provided by the camera manufacturer. A schematic of the processing scheme appears in Figure 20 on page 59. The program itself images all three channels from the imaging system (future revisions will also simultaneously acquire spectra from the SpectroPen). These data are then processed in software to create a composite display. The composite display shows the location of any NIR light (presumably from the contrast agent) overlaid onto the anatomic view. The system also shows the position of the laser excitation source. As currently configured, the contrast agent is shown in cyan, and the laser position as a red circle. An example of the software interface is shown in Figure 20 on page 59 as well. The view of the software shown is for an assistant, the system operator (*i.e.,* surgeon) would only be shown the composite view

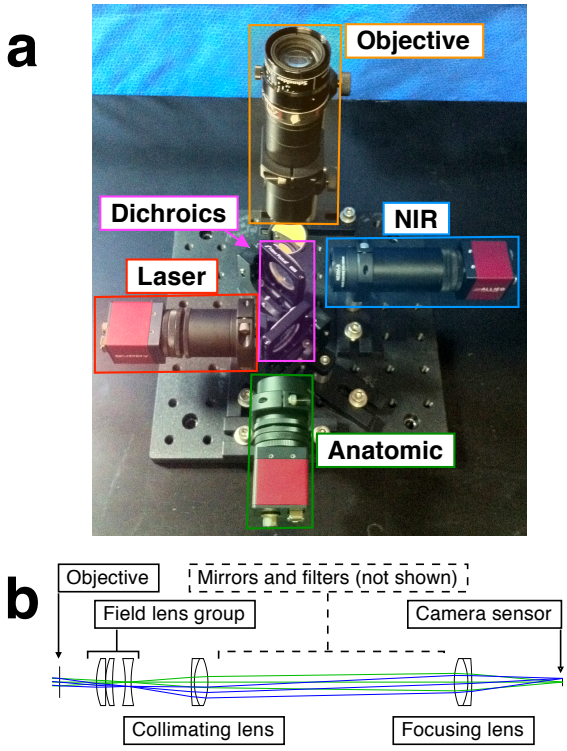

Figure 19: Current implementation of the widefield imaging head. (A) A marked image of the current widefield imaging head, upside-down from the working orientation (with the objective facing downwards). (B) Optical layout for the field, collimating, and focusing lenses that are obscured from view by the lens tubes in (A).

on a physically separate display as to minimize distractions. The software records experiment metadata (*e.g.,* experiment date, system operator, contrast agent used) and can record still frames or live video. In addition, the software can apply real-time video processing filters, for example, one filter increases the persistence time that the NIR display is shown on screen. The filter is inspired by the decaying luminescence over time that defines phosphorescence, and so is called "virtual phosphorescence". Applying the filter (implementation described in methods) makes any NIR signal appear to "glow" when the SpectroPen is swept over an area, much like the luminous hands of a wrist watch. Changing the user set decay time allows the user to select a persistence time that assists in unobtrusively localizing NIR emission. This is an example software feature that can increase usability of the system without experimental changes: other "smart features" that can assist are autofocusing the lens on the laser location or zooming the composite display on the laser location (by definition, the area of interest), or emitting a click sound with a rate proportional to the amount of NIR signal detected (similar to a Geiger counter).

3.4.2.2 Characterization

We tested the imaging performance of the proof-of-concept system built using the U.S. Air Force (USAF) 1951 test chart for the resolution limit, as well as calculating the contrast transfer function (CTF, closely related to the modulation transfer function, MTF) of the lens system. The results of the testing are shown in Figure 21 on page 60. The camera resolution itself is low (768×492 pixels), and is interlaced (acquiring even line pixels in one field, then odd line pixels in the next field, and combining these two fields to make one frame), and has a color Bayer filter in place. The interlaced nature of the camera causes the resolution limit of the system to be different in the vertical and horizontal directions, 2.8 line pairs per mm in the vertical direction, and 4 line pairs per mm in the horizontal direction. The imaging quality is reflective of the economy of the system design as well as the nature of the off-the-shelf lenses used. The most noticeable aberration is vignetting. The vignetting

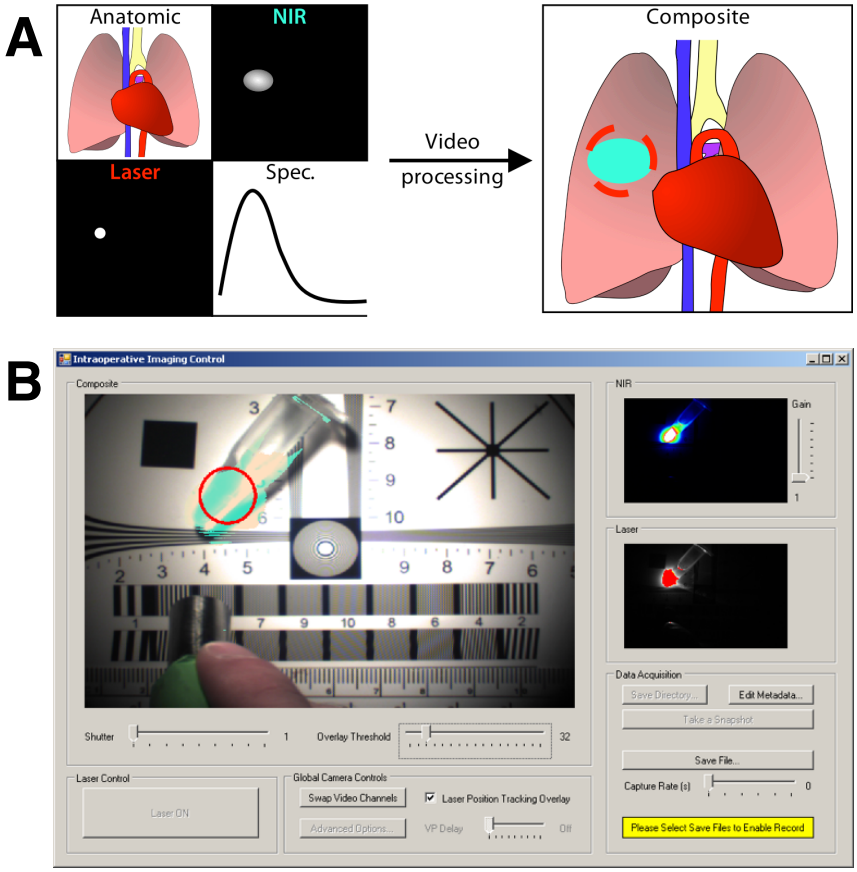

Figure 20: Software processing scheme for the integrated imaging system. (A) is the general scheme for software processing: information from available channels (anatomic view, laser tracking, near-infrared (NIR) light, and spectroscopy) are all used to create a composite image displayed to the system operator. (B) is a screenshot of the system software that was developed in-house, as would be shown to an assistant to the system operator.

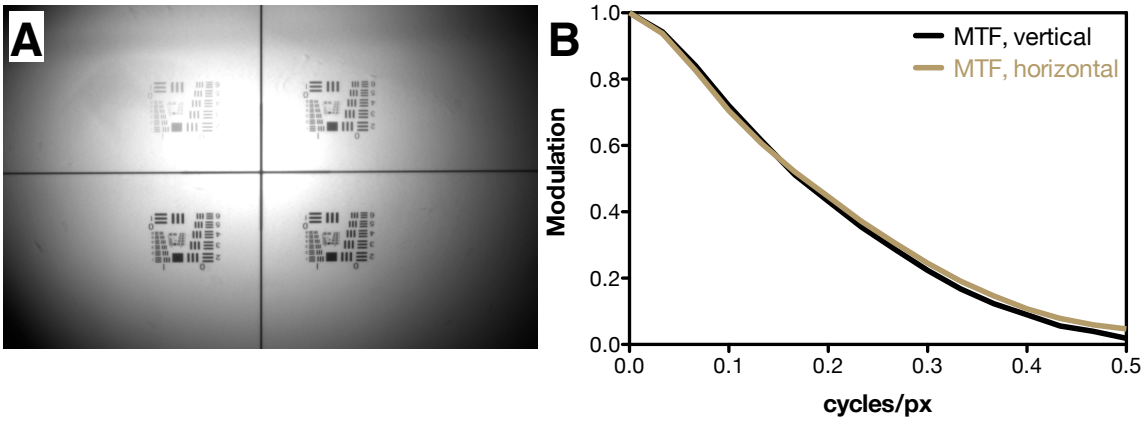

Figure 21: Optical resolution testing of the imaging head. (A) The USAF-1951 test target was imaged by the widefield imaging head, under normal conditions for animal surgery. Illumination is provided by two consumer white-LED bulbs. Resolution limit of the system is 4 lp/mm horizontally, 2.8 lp/mm vertically (difference due in part to interlaced camera sensors). (B) The calculated modulation transfer function (MTF) for the system, measured by the color camera at the center of the imaging field, in both the vertical and horizontal directions. The MTF was calculated by using a slanted-edge test target.

is a result of the small diameter (relative to the sensor size) catalog lenses for imaging. Another issue with the current implementation is chromatic aberration, particularly in the blue light range. This is unavoidable because of the broadband imaging range required and cost constraints. The imaging performance in terms of detection sensitivity was tested next.

When used with the SpectroPen, quantification of contrast agents can be done through the spectra recorded, as was shown in Figure 17 on page 54. This is advantageous because of the high sensitivity of the SpectroPen, close proximity to the sample, and discrimination afforded by spectroscopy. The widefield imaging system, because of economy as a design goal, is one-fifth the cost of the SpectroPen prototype. Combining the widefield imaging head with a near-infrared "laser pointer" could be useful as a low-cost surgical system. We tested the limit of detection for the widefield system alone, detecting ICG in tissue homogenates, by dosimetry on the NIR channel. As shown in Figure 22 on the following page, the system has a dynamic range of approximately 30 fold, more than sufficient for surgical imaging where a contrast ratio of 5 is considered outstanding. Assuming a Gaussian emission profile over the same area as was tested in the experiments, the system has a

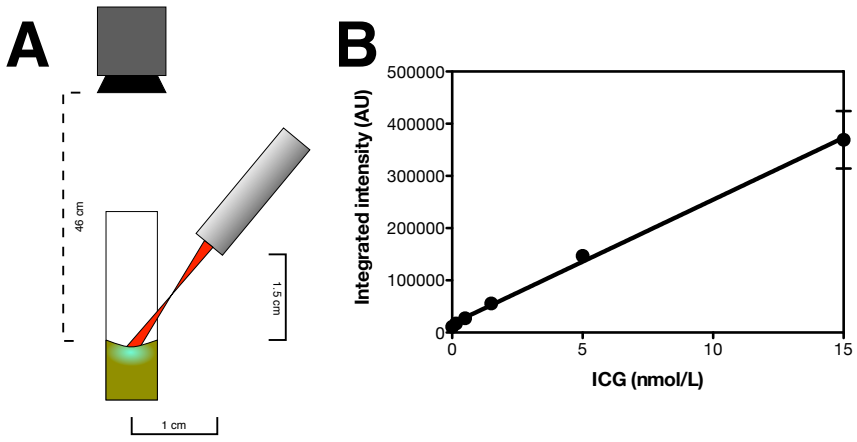

Figure 22: Widefield imaging head limit of detection for indocyanine (ICG) in tissue homogenate. ICG was diluted into 5% (w/v) tissue homogenate in glass vials and placed under the widefield imaging head, arranged as in (A). As shown in (B), the area sum of ICG fluorescence as measured on the near-infrared camera channel shows a linear response, with a Pearson's coefficient of 0.99. Error bars show the 95% confidence interval (n = 3).

detection limit between 0.15–0.5 nmol/L ICG. Both the dynamic range and detection limit for the widefield imaging head compare well to the SpectroPen.

3.5 Integrated intraoperative instrumentation as a platform technology

The instrumentation presented describes an integrated platform technology, consisting of the local point excitation source (with optional spectroscopy), widefield imaging, the software powering the system, and the exogenous contrast agent used for tumor imaging. This system is a flexible design: the local excitation source can be used alone, with fluorescence spectroscopy, or with Raman spectroscopy (in order of increasing resolution and cost). The widefield imaging system need not be present (perhaps for ultra-portable needs), could be a low-cost system as is presented here, or could be a high-performance system using cooled or intensified imaging sensors for increased sensitivity. The instrumentation enables the contrast agents to be used, but it is the contrast agents that make the entire system work. Contrast agents could change the types of tumor lesions detected (perhaps through active targeting mechanisms), improve sensitivity through an activatible fluorescence scheme (as

Table 1: Specifications of the currently implemented intraoperative instrumentation

Parameter	Specification
Number of imaging channels	3
Imaging wavelengths	400–700, 700–800, 800–900
Camera resolution	768×492
Camera maximum frame rate	60 fields/second (interlaced)
Camera sensor size	1/2 in.
Camera cell sensor size	$8.4\ \mu\text{m} \times 9.8\ \mu\text{m}$
Camera NIR QE	700 nm: 80%, 800 nm: 47%, 900 nm: 23%
System resolution limit	4 lp/mm (horizontal), 2.8 lp/mm (vertical)
Intended working distance	60 cm
Field of view (at working distance)	11 cm × 7 cm
Pixel spacial resolution (at working distance)	145 μm
System aperture	$f/4$
ICG detection limit	0.15–0.5 nmol/L
Dynamic range	30 fold
Excitation source wavelength	785 nm
Excitation source irradiance (at focus)	1.3 kW/cm^2
Excitation source focal length	0.5 cm
Excitation source spot size (at focus)	100 micron
Spectrograph resolution	0.6 nm / 8 cm^{-1}
Spectrograph range	200–2000 cm^{-1}
ICG detection limit	0.05 nmol/L
Dynamic range	40–50 fold

has been demonstrated by Tsien's group), or be used for combination intraoperative surgery and intraoperative pathology.[180] As shown through the "virtual phosphorescence" example, the integrated software can greatly enhance the usability of the system. The specifications of the current prototype implementation, as characterized in this chapter, are summarized in Table 1 on the current page.

3.6 Conclusions

We have described proof-of-concept instrumentation designed for medical imaging, specifically to offer intraoperative guidance during surgery. The instrumentation is designed to work with contrast enhancement, instead of native detection of biomolecules. The systems are complementary: point spectroscopy offers increased specificity over a simple bandpass

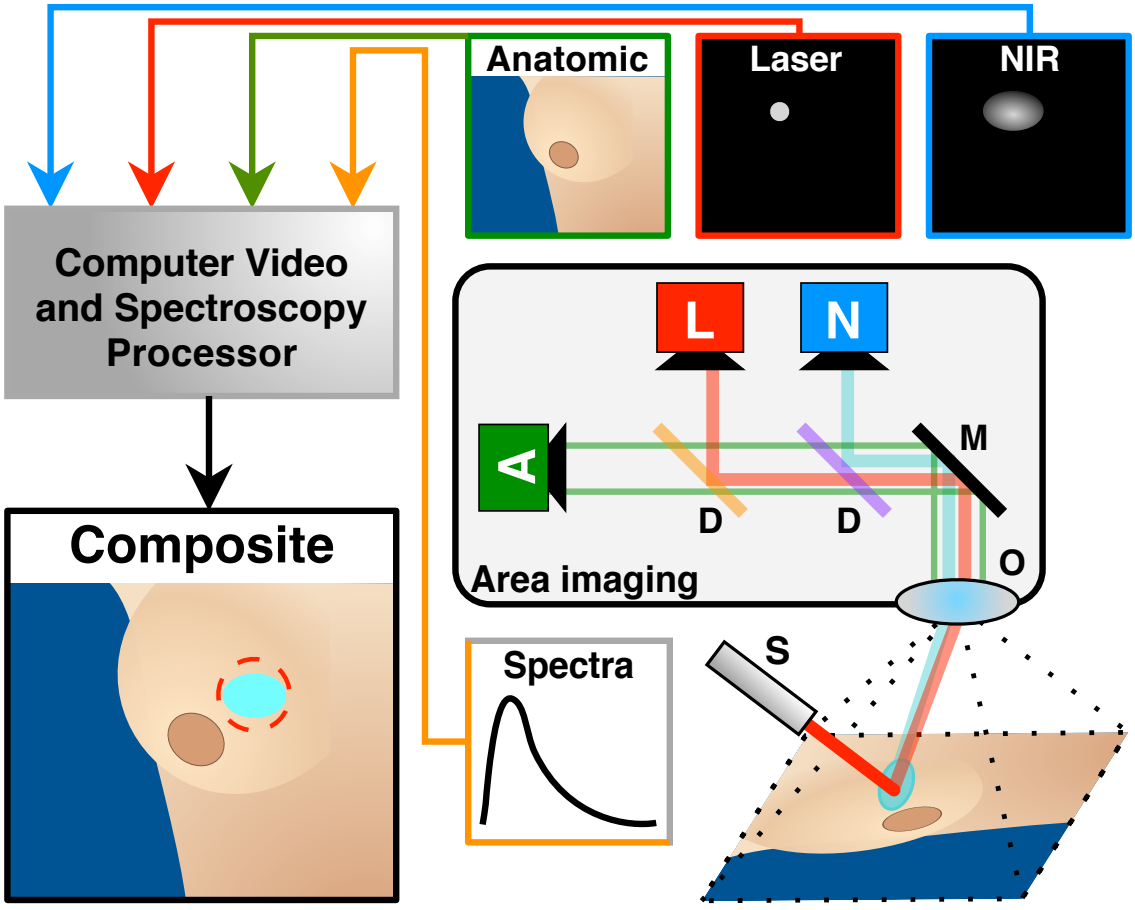

Figure 23: Operational scheme of widefield imaging with directed point excitation and spectroscopy. The widefield imaging head (center-right) is positioned over the surgical area. Directed point excitation is provided in this case by the SpectroPen (S). The area imaging system uses 3 cameras to image the anatomical view (A), the laser position within the anatomical view (L), and any near-infrared (NIR) light emitted within the anatomical view (N). The area is imaged by a common objective lens (O) and the collected light is folded by mirrors (M) and folded/filtered by dichroic mirrors (D). Complex optics within the area imaging head (e.g. collimation lenses, bandpass filters, etc.) are not depicted. The three video channels recorded by the cameras (top-right) and spectral information collected by the SpectroPen (bottom-center) are processed by a computer system to synthesize a composite display (bottom-left) to show anatomical landmarks with the laser position and any detected NIR signal.

filter, while widefield imaging offers spatial information that is lost with point spectroscopy. Integration of the two instruments also makes wide area Raman spectroscopy practical for medical use. This is a system where the whole is greater than the sum of its parts. In Chapter 4, we show the application of these two devices to medical imaging *in vivo*.

CHAPTER IV

GUIDING CANCER SURGERY THROUGH IMAGING AND SPECTROSCOPY

4.1 Abstract

The clinical efficacy of cancer surgery is dependent on the skill of the surgeon. Although preoperative imaging can diagnose and locate tumors, intraoperatively, a surgeon must rely on their visual and tactile senses, honed through experience, to determine the location of a tumor and whether a tumor has been completely removed. Improving the ability of a surgeon to completely resect a tumor would be expected to improve the odds of a patient having a good surgical outcome. In this chapter, we describe how the instrumentation developed in Chapter 3 has been applied to animal models of cancer as well as clinical canine patients with cancer. Initial results show that using clinically-approved fluorescent contrast agents, along with the instrumentation developed, neoplasia is distinguishable from normal tissue in both murine tumor models and in spontaneous tumors in companion canines. The pre-clinical data support the further development of this instrumentation towards clinical translation.

4.2 Introduction

In Chapter 3, we introduced instrumentation designed for imaging contrast agents *in vivo* to be used for guiding cancer surgery. A schematic overview of the integrated imaging system platform appeared in Figure 23 on page 63. In comparison to other widefield fluorescence imaging systems that use wide area illumination, the system we presented uses a point excitation source directed by the operator to probe the patient.[252, 206, 225] Interactive point excitation has several advantages over wide area illumination. One advantage is

that by definition, the area of interest to the operator is always known—this is useful for image processing. Another advantage overcomes fluorescent dye photobleaching: wide area illumination excites fluorophores in the entire surgical field, photobleaching those of interest to the operator as well as those not currently inspected by the operator; interactive point excitation only photobleaches fluorophores undergoing inspection. A third advantage is that point excitation can have high fluence rates not practically achievable with wide area illumination, overcoming attenuation due to the absorption and scatter inherent in biological imaging. Fourth, wide area illumination can color the surgical field, making operating on the patient more difficult. Finally, a major advantage of the integrated system is that it makes real-time (30 frames per second video), wide area spectroscopy practical. Tunable filters or filter wheels, used by some for intraoperative spectroscopy, have a finite acquisition time and so are not real-time. For imaging Raman scatter (an inherently weak process) a high numerical aperture is required: this is provided through having the point excitation probe near the surgical cavity, and cannot happen with a widefield imaging head sitting over a surgical cavity with clearance necessary for work on the patient. Of course, a high numerical aperture is beneficial for fluorescence imaging as well. The solution is to acquire spectroscopy through a local probe and spacial information through a distant probe, and then combine the information sets into a composite display. Others, notably Michael Feld, have proposed using spectroscopy in medicine, however spectroscopy alone lacks the "intuitive" information display inherent in showing spectral information composited on an image of the surgical area.[170, 171] A major and clear disadvantage of interactive point excitation and spectroscopy is that it is interactive: it requires a free hand to use. While the interactive nature might require that a surgeon to switch between imaging and cutting, there are numerous other personnel in the operating suite who can assist in operating the instrumentation while the surgeon is cutting, and software features (such as taking and displaying still photographs) can lessen the burdens of interactive excitation.

We use indocyanine green (ICG) as our lead contrast agent for intraoperative imaging in

animals. ICG has a long history of use as a blood pool contrast agent, being first approved by the U.S. Food and Drug Administration (FDA) for human use in the 1950s.[37, 8, 126] It is considered very safe, with few reported adverse events.[17] The most common adverse event is an allergic reaction, and so ICG is conta-indicated in patients with iodine allergies. ICG is currently FDA-approved for hepatic blood flow monitoring and retinal angiography. Interestingly, ICG immediately complexes with serum albumins when injected systemically, due to the overall hydrophobicity of ICG and a hydrophobic binding pocket within serum albumins. This means that *in vivo*, ICG tends to behave as a 4–6 nm macromolecule or nanoparticle. As was explained in Chapter 2, macromolecules and nanoparticles tend to accumulate within tumors through the enhanced permeability and retention (EPR) effect. ICG would thus be expected to passively accumulate within tumors. As one of only two FDA-approved fluorophores (the other being fluorescein), ICG is commonly used as an *in vivo* human contrast agent for investigational fluorescence imaging systems. Although it is an off-label use, since ICG is recognized as safe and has FDA-approval for other applications, it has an easier approval path than novel contrast agents. Recently, locally-injected ICG has been used by several investigators for fluorescence-guided sentinel lymph node (SLN) mapping.[252, 206, 225, 272] The SLN is the lymph node which drains a defined area in the body, so if a tumor is to metastasize, it will go to the SLN first.[19] Colloids (radiocolloids or strongly-absorbing dyes) are commonly used for the same purpose.[36, 10, 175] In contrast to other groups, we are using systemically-injected ICG as a tumor contrast agent. ICG has been used as a tumor contrast agent previously, but required unconventional imaging modalities to detect *in vivo* because of the overall low quantum yield of ICG in aqueous environments.[206, 198] Clinically, ICG is used for bolus injections, with total dosages of 0.5–1 mg/kg and a maximum FDA-allowed dose of 2 mg/kg.

In this chapter, we first demonstrate the use of our intraoperative instrumentation in guiding cancer surgery in murine tumor models. Murine tumor models have contributed

greatly to human medicine, but they have limitations.[219, 220, 128] Notably, murine xenograft and ectopic tumor models tend to have a fibrous capsule that clearly delineates the tumor from normal tissue. These tumors also tend to have poor vascular integrity beyond that of natural human tumor. Since the EPR effect is dependent on poor vascular integrity, murine tumor models often have higher accumulations of macromolecules by the EPR effect than is observed in human tumors. Orthotopic murine tumors are architecturally closer to a natural human cancer, however, they do not overcome the scaling differences between mice and men. Operating on a mouse necessitates using smaller tools and instrumentation with a greater magnification factor than for human surgery. To overcome the challenges inherent in using murine tumor models, we have also investigated using canines with spontaneous cancers. In drug development, there is a growing movement to use companion canines with cancer as part of the drug development pipeline. [90, 192] Companion canines are afflicted with the same cancers as humans (but with different incident rates), and the cancers are biochemically and architecturally similar to the corresponding cancer in humans. Companion canine cancers are also much more similar in size to those in humans. The surgical procedures and medical care for canines are in most cases identical to those in humans: a largest difference being that normal tissue preservation to achieve a good cosmetic result is less of a concern. Canines also have a similar drug response profile to humans—ICG was originally investigated in canines and so is known to be safe to use. Using companion canines with spontaneous tumors, we are able to perform correlation analyses between imaging ICG and the pathologic status of the tissue, a critical step in translating this technology to the clinic.

We envision the workflow of image guided surgery to begin by the patient being diagnosed with operable cancer: perhaps through an x-ray computed tomography (CT) or magnetic resonance (MR) imaging scan with contrast agent, followed by a fine-needle aspirate (FNA) or incisional biopsy to confirm neoplasia. A surgery date is scheduled and a surgical plan is made. The day of surgery, while preparing the patient for surgery, the

patient is injected with a tumoral contrast agent such as indocyanine green (ICG). This contrast agent will accumulate through passive (as in the case of ICG) or active means in the tumor, providing contrast between neoplastic and normal tissue. Surgery begins: the surgeon, guided by preoperative imaging, exposes the area where the tumor is suspected to be. The tumor removal procedure is illustrated in Figure 24 on the next page. The surgeon uses the imaging system to confirm the tumor position and borders of the tumor. The surgeon then debulks the tumor, attempting to remove the entire tumor with the smallest margin between neoplastic and normal tissue possible. The tumor bed is then scanned to detect residual disease. Any residual disease is then removed until the tumor bed appears "clean" (*i.e.,* a complete resection). The device could then be used for sentinel lymph nodes (SLN) dissection by injecting ICG into the tumor bed and following the lymph drainage. Finally, the resected tissues can be checked intraoperatively to confirm contrast accumulation before submitting to pathology. The pathologist can use the same contrast agents and instrumentation (optimized for pathology) to find areas of interest to investigate in writing the pathology report.

4.3 Methods

4.3.1 Animal experiments

4.3.1.1 Murine tumor models

All *in vivo* murine studies were performed under a protocol approved by the Emory University Institutional Animal Care and Use Committee. Mice used were age-matched nude athymic females. The tumor cell line 4T1 (a murine mammary carcinoma, stably expressing firefly luciferase) was used to create the tumor models. Cell lines were maintained as per American Tissue Type Collection guidelines. The cells were washed with phosphate-buffered saline (PBS) before collecting and diluting to a final concentration of 2×10^7 cells/milliliter for injection. Cells were injected into the flank, approximately 2×10^6

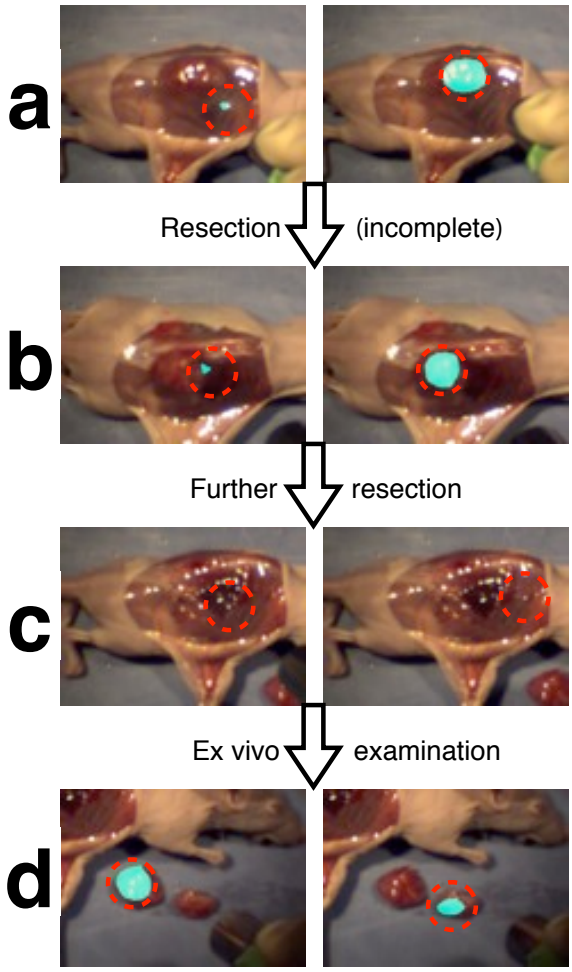

Figure 24: Workflow for resection of tumors by interactive intraoperative guidance. (A) Initially, the suspect tumor area is scanned to find the borders of the tumor, as determined by indocyanine green (ICG) accumulation. (B) The tumor is then removed by standard surgical technique. Following resection, the surgical bed is rescanned to find residual ICG signal. (C) The resection is revised until no ICG signal is detected in the surgical bed. (D) Finally, the resected surgical specimen are scanned to confirm ICG accumulation and areas of pathologic interest for histologic analysis. Areas of ICG accumulation are false-colored cyan, and the area the point excitation source is being directed is shown by the dashed red circle.

cells, per animal. Anesthesia was provided by an intraperitoneal injection of 2.5% tribromoethanol in PBS. For bioluminescence imaging, the animals were injected with 100 μmol/L of luciferin (30 mg/mL) intraperitoneal, then imaged on a bioluminescence imaging system 5 minutes after injection. Animals were sacrificed by CO_2 asphyxiation.

4.3.1.2 Clinical canine patients

Clinical canine patients are handled by a veterinary team at the University of Georgia (UGA) College of Veterinary Medicine (CVM) under a Clinical Research Committee approved protocol. Canine patients are recruited by a veterinary oncologist, Dr. Corey Saba. After informed consent is given, canine patients receive standard of care treatment with the sole addition of an ICG injection (prepared by the pharmacy) before surgery. Canine patients are monitored for anaphylaxis reactions after ICG infusion. A small financial incentive (hospital credit for medical costs) is given to owners of canine patients for participating in the trial. To participate in the trial, canine patients must have cytologically or histologically confirmed malignant solid-mass tumors amenable to surgical resection. There must be no severe underlying disease, and no known allergy to contrast agents.

4.3.2 ICG pharmacokinetics and biodistribution

4.3.2.1 Percent accumulated dose in tumor

ICG at indicated doses was injected by tail vein into mice bearing 4T1 tumors approximately 5–10 mm in diameter, 3 mice per dose. After 24 hours, the mice were sacrificed and the tumors were harvested. The tumors from 5 mice not injected with ICG (reference sample) were also harvested. The tumors within groups were pooled and homogenized. The homogenized tissue was diluted with PBS such that the percent weight of tumor in each sample was equal. ICG diluted into 4% BSA (w/v) in PBS was then spiked into the reference sample homogenate sample with known concentrations of dye. A standard curve was generated from the integrated ICG fluorescence in the spiked homogenates. The integrated ICG fluorescence in the dosed mice was then measured and correlated to the

standard curve to determine the amount of ICG in each tumor group. These values were then correlated to the administered ICG dose.

4.3.2.2 Pharmacokinetics and biodistribution

ICG at indicated doses was injected by tail vein into mice bearing 4T1 tumors approximately 5–10 mm in diameter, 1 mouse per dose. At the specified time intervals, the mice were sacrificed and perfused with saline to flush blood and any ICG in the serum out of the tissues. The tumor, muscle, and lung were then removed and quantified for ICG fluorescence.

4.3.3 *In vivo* measurements of ICG accumulation in murine tumors

ICG was infused in mice bearing 4T1 tumors at a concentration of 357 μg/kg via the tail vein for imaging 24 hours later. Mice were anesthetized and injected with luciferin before bioluminescence imaging. The animals were then scanned with the SpectroPen at regularly spaced intervals, with the SpectroPen held a constant distance away from the tissue. The integrated ICG fluorescence signals recorded were then correlated to the measurement locations on the brightfield and bioluminescence images. Surgery was then performed with standard technique to remove the tumor mass (without continuous SpectroPen guidance). After surgery, the resected tumor and tumor bed were imaged a second time with brightfield and bioluminescence imaging to confirm completion of the resection. Any areas of bioluminescence activity following surgery were probed with the SpectroPen.

Tissues excised (including tumor, tumor bed, and any other areas of interest) were fixed in fresh 3.7% formaldehyde in PBS and submitted to a core facility for paraffin-embedding and processing with H&E or immunohistochemistry.

4.3.4 *In vivo* measurements of ICG accumulation in companion canine tumors and histologic correlation

After *en bloc* removal of the tumor, intraoperative measurements were taken of the tumor bed by the attending surgeon (Dr. Karen Cornell, Chad Schmiedt, or MaryAnn Radlinsky,

UGA-CVM) with the SpectroPen placed in a sterile sleeve. Following surgery, tissue specimens resected from the patient, including biopsies of the tumor bed, were probed with the SpectroPen in the presence of the attending pathologist, Dr. Elizabeth Howerth (UGA-CVM). Locations of spectral readings were recorded on a photograph of the tissue sample for later correlation to the histologic preparations, or when available, recorded by the integrated imaging system. The pathologist was blinded to the results of the spectral readings. After histologic mounting, the points of interest were marked on the prepared slide images and given to the pathologist to render determination of the presence or absence of neoplasia in a 0%, 50%, or 100% likelihood scale. In later patient cases, punch biopsies were taken at sites of interest with a 1.0×0.5 cm punch biopsy tool—these punch biopsies were probed for ICG fluorescence using the SpectroPen before being formalin-fixed and paraffin-embedded by standard practices.

Statistical testing varied based on the circumstances. For complete data sets, including 0%, 50%, and 100% tumor likelihood samples, data were analyzed by Kruskal-Wallis non-parametric testing. Post-hoc multiple comparison testing was done by Dunn's method. A p-value of 0.05 was used as the threshold for statistical significance. For incomplete data sets (having only 0% and 100% tumor likelihood samples), data were analyzed by a Mann-Whitney non-parametric test. The receiver-operator characteristic (ROC) was calculated using the 0% and 100% tumor likelihood values only.

4.4 Results and discussion

Using ICG as a systemically-injected tumor contrast agent is atypical, so we first determined the accumulation of ICG within murine tumor models as a function of the injected dose one day before tumor removal. As shown in Figure 25 on the following page, we find that there is a dose-dependent behavior in the amount of ICG that accumulates in the tumor. For low doses of ICG (below 500 μg/kg), approximately 0.05% of the injected dose is delivered to the tumor; for high doses of ICG (1–2 mg/kg, closer to clinical dosing),

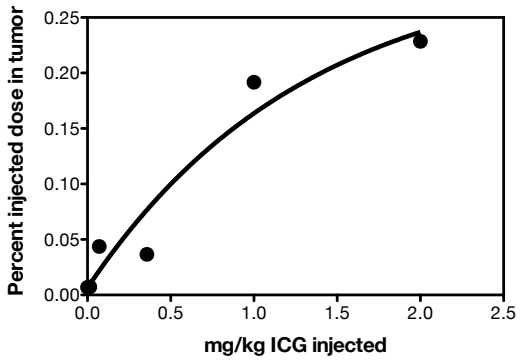

Figure 25: Indocyanine green (ICG) accumulation within tumors is dose-dependent. ICG at indicated doses was injected via tail vein into mice bearing 4T1 ectopic tumors. The tumors were harvested after one day, homogenized, and then compared against ICG spiked into homogenate from mice bearing tumors but not injected with ICG. Each point is the average of 3 harvested tumors, the line of fit is a one-phase exponential association regression model shown as a visual guide.

approximately 0.2% of the injected dose is delivered to the tumor. This difference could reflect a change in the ICG clearance rate from normal tissue: in the sub-clinical dosing regime, ICG is cleared from normal tissue within one day, whereas in the clinical dosing regime, ICG is still being cleared from tissues (both normal and abnormal), and so the apparent dose is higher. This saturation of the clearance mechanism is most likely involving the lymphatics, since the ICG pharmacokinetics have been well-described and ICG as a compound is known to clear from the circulation within minutes. Since the subclinical dosing regime offered sufficient signal for imaging, we next quantified the pharmacokinetics of ICG accumulation within the tumors, compared to lung and muscle tissue (both highly vascular). As shown in Figure 26 on the next page, doses of 71.4 or 357 μg/kg offered tumor contrast relative to lung or muscle (selected because they are highly vascularized) at all time intervals interesting for surgery, between 1–48 hours.

4.4.1 Imaging and spectroscopy of murine tumor models

We then tested the usability of ICG accumulation for delineating tumor boundaries in a murine tumor model. The tumor cell line used, 4T1, is transgenic with a luciferase reporter

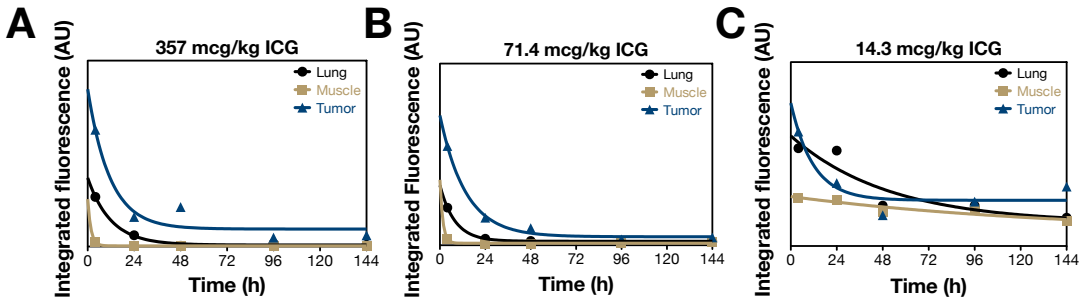

Figure 26: Pharmacokinetics and biodistribution of indocyanine (ICG) in a murine tumor model. ICG was injected into mice bearing MDA-MB-231 breast cancer cells in a xenograft flank tumor model in 3 subclinical doses. The tumors and tissue were removed at specified time intervals following injection and quantified for fluorescence with the SpectroPen. Regression lines are an exponential decay model shown as a visual guide.

gene and so can be detected by bioluminescence. Comparing the bioluminescence readings and spectra recorded with the SpectroPen shows that there is a an enhancement of 5–10 fold in ICG accumulation in the primary tumor and "satellite tumor" (tumor growing at the tumor injection site) relative to the tumor-free areas around the tumor. Examination of the surgical cavity and resected tumor following surgery showed that the high ICG signals were still associated with the tumor, approximately 10 fold higher in the tumor than the tumor bed. As shown in Figure 28 on page 77, a small point of tumor cells were detected in the surgical cavity under bioluminescence imaging that were not obvious on visual inspection. This area was detectible using the SpectroPen with an approximate 5 fold higher ICG fluorescence relative to the surgical bed. This illustrates how spectroscopy guidance can detect residual disease.

We then examined whether the tissue detected as tumor positive by the integrated imaging system was indeed tumor positive, using histology as a gold reference. As shown in Figure 30 on page 79, we found that the primary tumor mass, visible by eye and under intraoperative instrumentation by ICG accumulation, was tumor positive by hematoxylin and eosin (H&E) staining. Curiously, when performing surgery on one mouse, we noticed

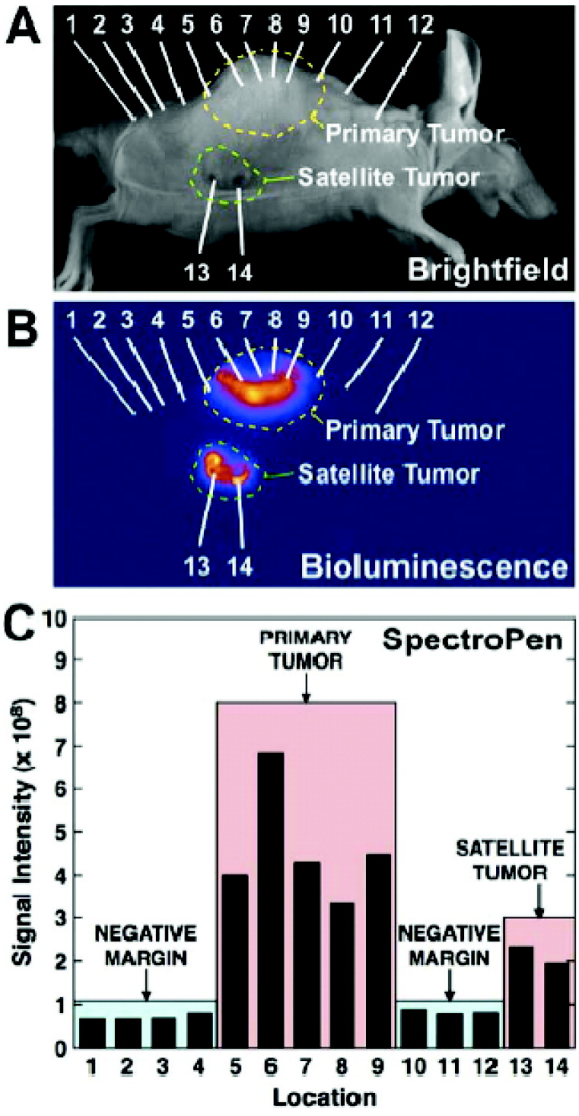

Figure 27: Systemically-injected indocyanine green (ICG) accumulates in mouse tumors as determined by bioluminescence. (A) A brightfield image of a mouse bearing a subcutaneous 4T1 mammary tumor. The mouse was measured at the indicated points by the SpectroPen. (B) The same mouse, imaged under bioluminescence imaging that can detect the transgenic tumor cells. (C) ICG fluorescence intensity as measured by the SpectroPen at the designated points on the image. Reprinted with permission from ref. [166]. Copyright 2010 American Chemical Society.

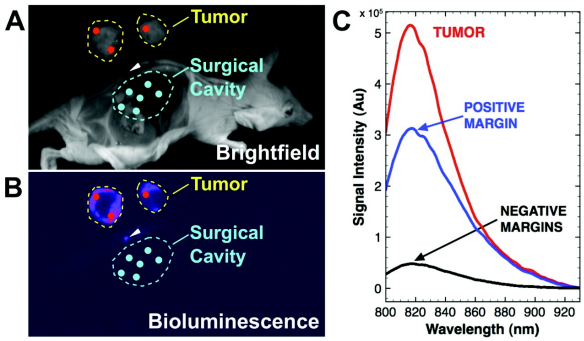

Figure 28: Indocyanine green (ICG) accumulation within tumors is specific enough to detect dirty surgical margins. A mouse bearing a 4T1 ectopic tumor was operated on to remove the primary mass. (A, B) Images of the mouse and excised tumor, as imaged under brightfield and bioluminescence imaging (which can detect the transgenic tumor cells), respectively. The SpectroPen was used to measure fluorescence from a prior injection of ICG at designated points across the animal. Interestingly, a positive tumor margin was detected by bioluminescence imaging; the positive margin was also distinguishable from background by using the SpectroPen. Reprinted with permission from ref. [166]. Copyright 2010 American Chemical Society.

an area not associated with the tumor that had an abnormally high amount of ICG accumulation. This area was identified as a lymph node by H&E histology, and was shown to be positive for tumor metastasis by cytokeratin-18 (CK18) immunohistochemistry (IHC). CK18 is considered a tumor marker for the 4T1 cell line used to create the tumor model. Areas of low ICG accumulation were shown to be free of tumor by histology. These results show that ICG accumulates in areas of "surgical interest". These results also illustrate the limitations of murine tumor models. In general, the ectopic and xenograft tumor models are well-encapsulated by a fibrous cap and so are easy to distinguish from normal tissue by visual inspection. There's no challenge to removal of the tumor, so the additional guidance provided by instrumentation cannot be tested. The ectopic and xenograft models are also notorious for having poorer vascular integrity than spontaneous tumors, magnifying macromolecule and nanoparticle accumulation by the EPR effect; ICG accumulation may not provide the same high contrast ratios with a spontaneous tumor. Although an orthotopic tumor model provides a more "natural" tumor to test, the small size of the mouse and the tumor make a histology correlation analysis difficult. Finally, testing different tumor

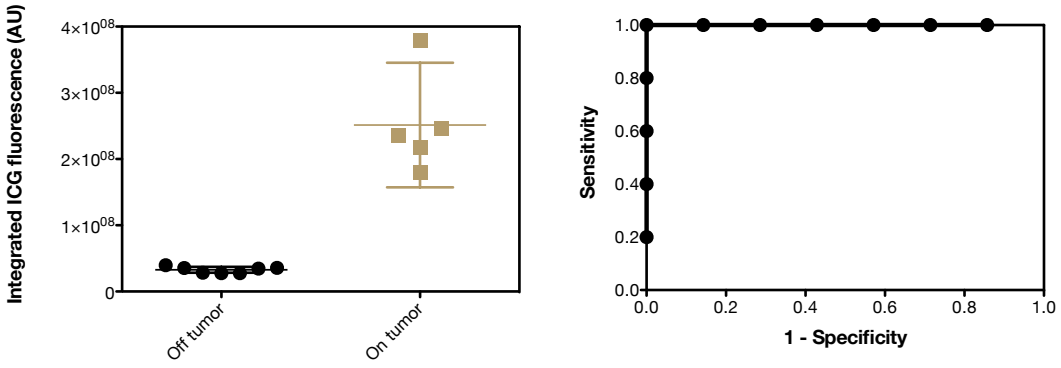

Figure 29: An example of the spurious contrast between normal and neoplasia in murine tumors. A mouse expressing an ectopic 4T1 tumor (expressing luciferase) was injected with indocyanine green (ICG) 24 hours before imaging with the SpectroPen. Sampled points were confirmed to be tumor by biolumenscence imaging of the transgenic tumor. As shown on the left, the contrast between normal and tumor is far higher than would be expected to be encountered *in vivo*. On the right is a receiver-operator characteristic (ROC) analysis of the data, showing perfect discrimination ability with an area under the curve of unity. The high contrast ratio is due to the limitations of this murine tumor model for this application and does not reflect the real capabilities of the system.

types through mouse tumor models is logistically difficult, because each tumor model has an associated cell line that must be cultured as well as verified. The greatest problem posed by using murine tumor models for histologic correlation is highlighted in Figure 29 on this page, an analysis of a murine tumor correlated with bioluminescence imaging. In this case, the difference between normal and neoplasia is so high as to be unrealistic. This high contrast is in part due to the artificially high leaky vasculature inherent in large murine tumor models and the encapsulated nature of the tumor creating an artificially abrupt difference between normal and neoplasia.

4.4.2 Imaging and spectroscopy of canine patient tumors

Due to the limitations in performing histological correlation in murine tumor models, we began working in a clinical canine population with spontaneous solid-mass tumors. Tumors in canines are biochemically and structurally similar to those in humans, and the size scale is more favorable to correlation analysis. Drawing from a clinical population also offers

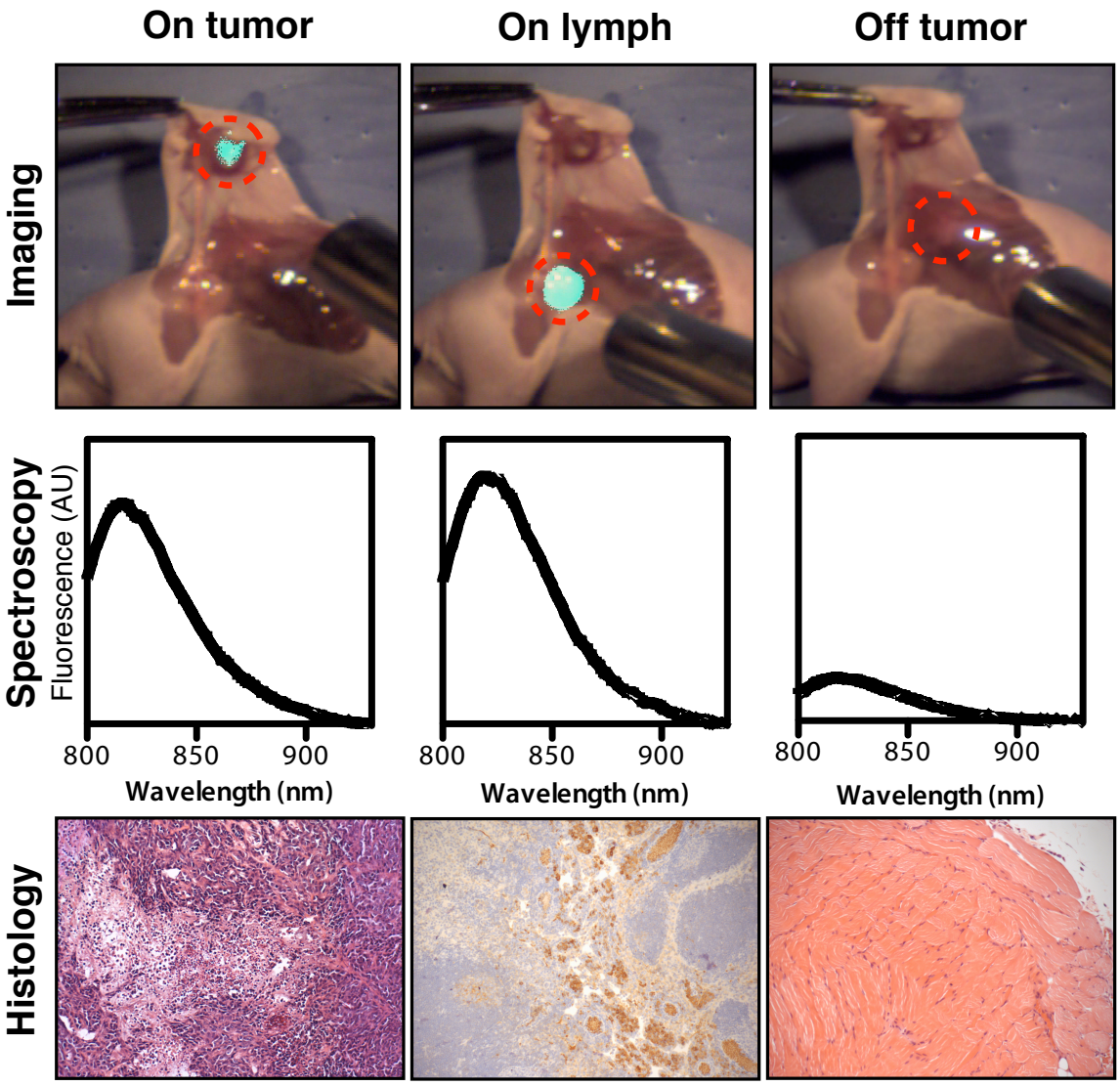

Figure 30: Systemically-injected indocyanine green (ICG) enriches in tumors and metastases but not normal tissue. A nude athymic mouse bearing a subcutaneous 4T1 tumor was injected by tail vein with ICG one day before dissection and imaging. When the SpectroPen is directed onto the tumor, the widefield imaging system is able to detect ICG emission (cyan false-color) and the spectrometer is able to record the ICG emission. Hematoxilyn and eosin (H&E) histology of the ICG-rich area is characteristic of tumor. Interestingly, an ICG "hot spot" was found that appeared to be a lymph node; cytokeratin-18 (CK18, a metastasis marker) immunohistochemistry of the tissue was positive, suggesting the lymph node was bearing a metastasis from the primary mass. When the SpectroPen is directed away from the tumor, no ICG emission is detected by the widefield imaging system or spectrometer. H&E histology of the "off tumor" location is consistent with skeletal muscle.

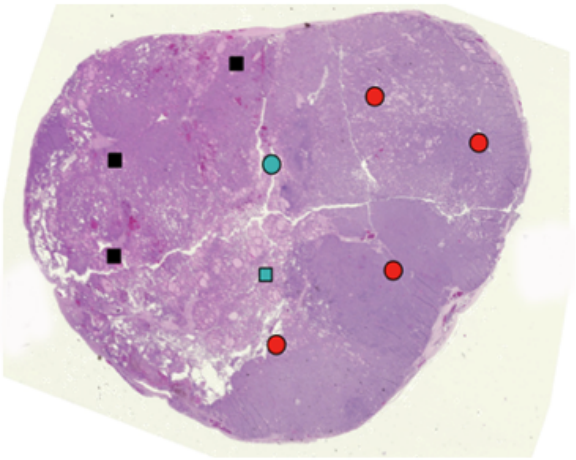

Figure 31: Indocyanine green (ICG) spectroscopy correlation with histology in a canine thyroid specimen. A 12-year old collie with thyroid carcinoma was infused with ICG one day before surgery to remove the thyroid. The thyroid was sliced in half and was probed with the SpectroPen. The same specimen was then prepared as a hematoxylin and eosin (H&E) slide. Areas of low ICG intensity are marked black, moderate ICG intensity cyan, and high ICG intensity (saturating the detector) are marked in red. Circles denote areas that are definitively tumor, whereas squares denote areas that are follicular tissue and may or may not be tumor. Histologic readings were performed by a veterinary pathologist.

the possibility to test efficacy in a number of tumor types and locations. In an early clinical experiment, we examined a 12-year old collie with a thyroid carcinoma. The patient was infused with pharmaceutical-grade ICG one day before surgery, as was done with the murine tumor experiments. The thyroid was probed for ICG accumulation and correlated with histology, as shown in Figure 31 on the current page. In this case, the pathologist reading the slide determined that tissue was either follicular or obviously tumor. In the case of follicular tissue, it was not possible to determine to what degree the tissue was neoplastic. A clear difference in ICG accumulation was detected between the follicular and neoplastic regions of the thyroid, but analysis was complicated by saturation of the SpectroPen detector in the neoplastic tissue regions. The thyroid carcinoma is a well-encapsulated tumor type, in some ways similar to the ectopic murine models.

We then focused on enrolling canine patients with tumors less encapsulated than thyroid carcinomas. One such canine patient was a 13-year old mixed-breed with a fibrosarcoma in the hind leg. The leg was amputated as is standard for this tumor type, size, and location.

A tissue slice from the amputated leg was placed under the integrated imaging system for analysis, as shown in Figure 32 on the following page. We found minimal ICG accumulation in normal fat and muscle, and high ICG accumulation within the tumor (which visually looked like the normal fat). Interestingly, we found an area of ICG accumulation in what appeared to be muscle, but further dissection showed this area to be occult tumor hidden by a layer of superficial muscle. Although the penetration depth of SpectroPen is only 1–3 mm for ICG (depending on tissue type, see Figure 18 on page 55), it is sufficient in this case to find occult tissue that would ordinarily be missed.

Encouraged, we performed histological correlations on several canine patients. The results of one bearing a histiocytoma (a Langerhans cell histiocytosis in humans), one bearing a neurofibrosarcoma, one bearing a salivary carcinoma, and one bearing a myxosarcoma are summarized in Figure 33 on page 83. Each example case also received a different ICG dosing: the histiocytoma and neurofibrosarcoma were dosed with 220 μg/kg at 24 hours before surgery; the salivary carcinoma received 220 μg/kg of ICG at 4 hours before surgery; the myxosarcoma received 71 μg/kg of ICG 2 hours before surgery. For human clinical use, same day dosage of ICG greatly reduces costs involved with patient handling and monitoring across two procedure days for 24 hour dosing versus same-day dosing, and as such is important for future clinical translation. In these 4 cases, the pathologist was instructed to classify each measured point as being either "0%" or "100% tumor likelihood". If the marked point was close to neoplastic tissue or was likely but not definitely neoplastic, it was marked as "50% tumor likelihood". There is some uncertainty in matching the points recorded with the SpectroPen with points on histologic preparations due mostly to tissue shape and size changes during processing, so point correlation is at best approximate (thus necessitating the "50%" category). In each of these cases, there was a statistically-significant difference in the mean values between the 0% and 100% tumor likelihood groups.

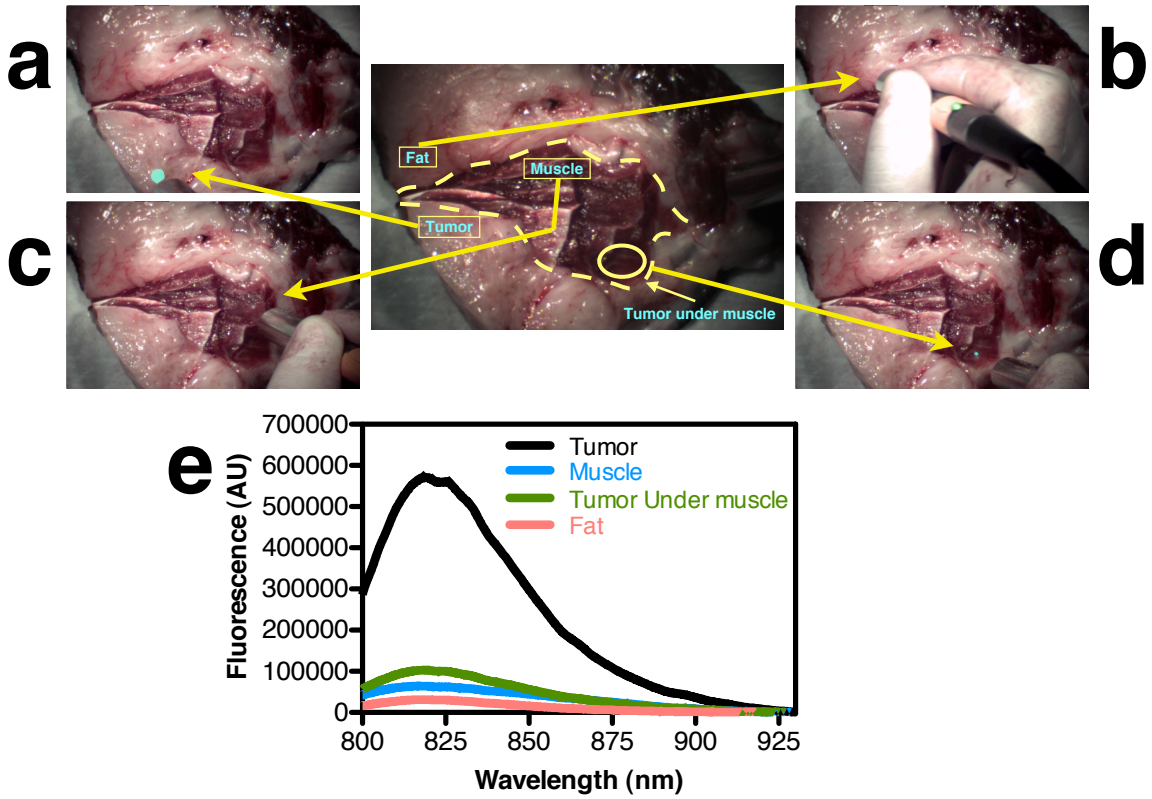

Figure 32: Post-operative imaging analysis of a surgical specimen from a canine with spontaneous fibrosarcoma. A 13-year old mixed-breed canine was infused with indocyanine green (ICG) one day before surgery to amputate the left hind leg that had an 8.5cm in diameter mass. The leg was dissected post-operatively for analysis of normal and neoplastic tissue as determined by visual and tactile inspection. ICG was found to accumulate and deposit in the tumor (a, cyan false-colored region) but not fatty connective tissue (b) or normal muscle (c). Interestingly, an ICG "hot spot" was detected in an area that appeared under gross inspection as muscle (d, small cyan false-colored region); further dissection into this area showed that the ICG had deposited into occult tumor laying 2 mm underneath the muscle. Areas rich in ICG deposits (tumor) show a unique spectral signature (e) that is distinct from the broad, featureless spectrum of normal tissue (muscle, fat).

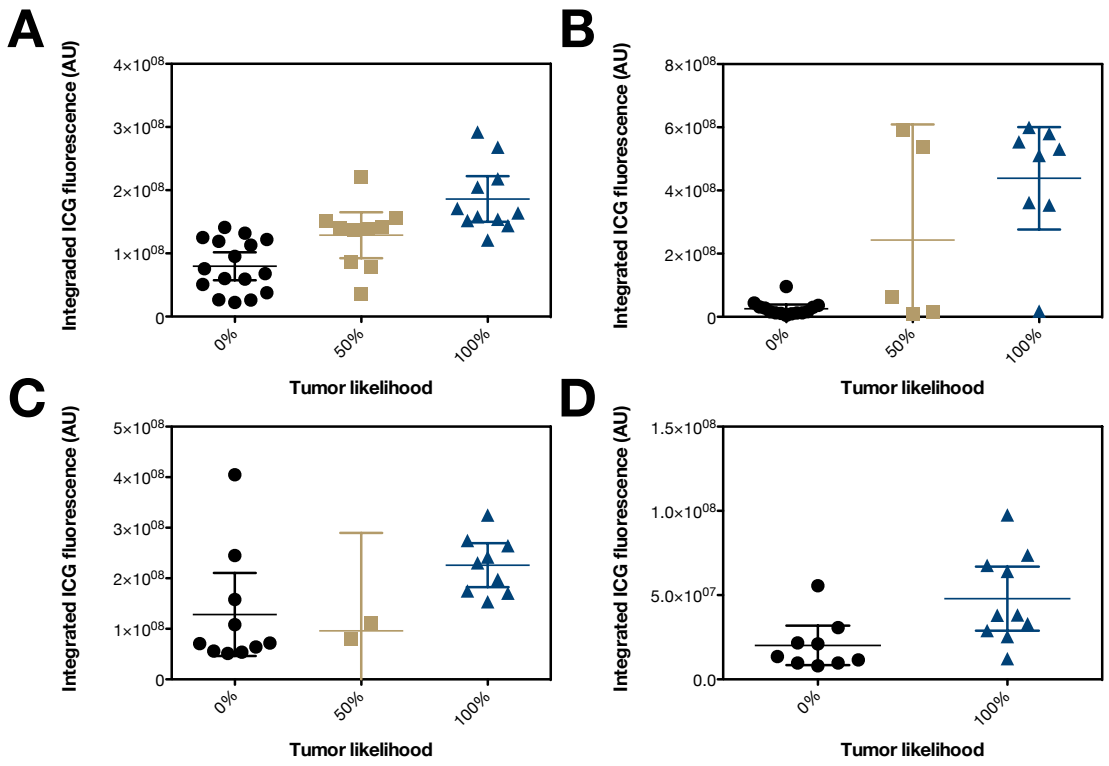

Figure 33: Post-operative imaging analysis is able to distinguish neoplasia from normal in canine patients. Four canine patients bearing a histiocytoma (A), neurofibrosarcoma (B), salivary carcinoma (C), and a myxosarcoma (D) were administered indocyanine green (ICG) 24 hours (A, B), 4 hours (C), and 2 hours (D) before surgery. In all four cases, there was statistically-significant difference between the mean integrated ICG fluorescence in the tumor tissue versus non-tumor tissue. Tumor likelihood values were given by a veterinary pathologist examining hematoxylin and eosin (H&E) preparations of the examined tissues. Error bars show the mean and 95% confidence intervals, statistical analysis was a Kruskal-Wallis non-parametric test with post-hoc Dunn's testing in the case of (A, B, and C), and a Mann-Whitney non-parametric test in the case of (D).

Knowing the histologic status at each measured point in the three canine patients summarized in Figure 33 on the previous page, we then subjected these data to receiver-operator characteristic (ROC) analysis using histology as the gold standard reference. ROC analysis reveals, among other values, how well a sample can be categorized at a given classification threshold.[261, 187, 70, 146] In each of the three cases, we found that the SpectroPen was able to sensitively (*i.e.,* high true positive rate) detect neoplasia with a low false positive rate (plotted as "1 - specificity"), as shown in Figure 34 on the following page. The area under the curve of an ROC curve is the probability that in selecting a true positive and a true negative, the true positive will be correctly identified. In the case of these three canine patients, the AUC are all above 80%, showing good discrimination ability.

4.4.2.1 Observations on imaging lymph nodes in canine patients

Sentinel lymph node (SLN) mapping seeks to dissect the lymph nodes draining a tumor with the hope of staging the tumor accurately and possibly remove metastatic disease.[19] Significant research effort by others is allocated towards developing fluorescent probes and fluorescence instrumentation for SLN mapping.[272, 10, 175, 256, 244, 12] While SLN mapping was not an objective of the clinical canine studies presented, lymph nodes were dissected from the patients as part of standard care and these nodes were available for imaging analysis. It must be noted that while others have used fluorescence (including ICG) for SLN mapping, in those cases it is by local peritumoral injection of the contrast agent, not systemic injection of contrast agent as in the case of the subjects presented in this dissertation. Shown in Figure 35 on page 87, we found that the ICG fluorescence observed in lymph nodes confirmed by histology to be free of disease to vary based on the time interval between ICG injection and surgery. For long time intervals (24 hours) between ICG injection and surgery, the pathologically negative lymph nodes were low in ICG signal. For the shorter time interval (4 hours) between ICG infusion and surgery, a wide distribution of ICG fluorescence in the negative lymph nodes was observed, ranging between

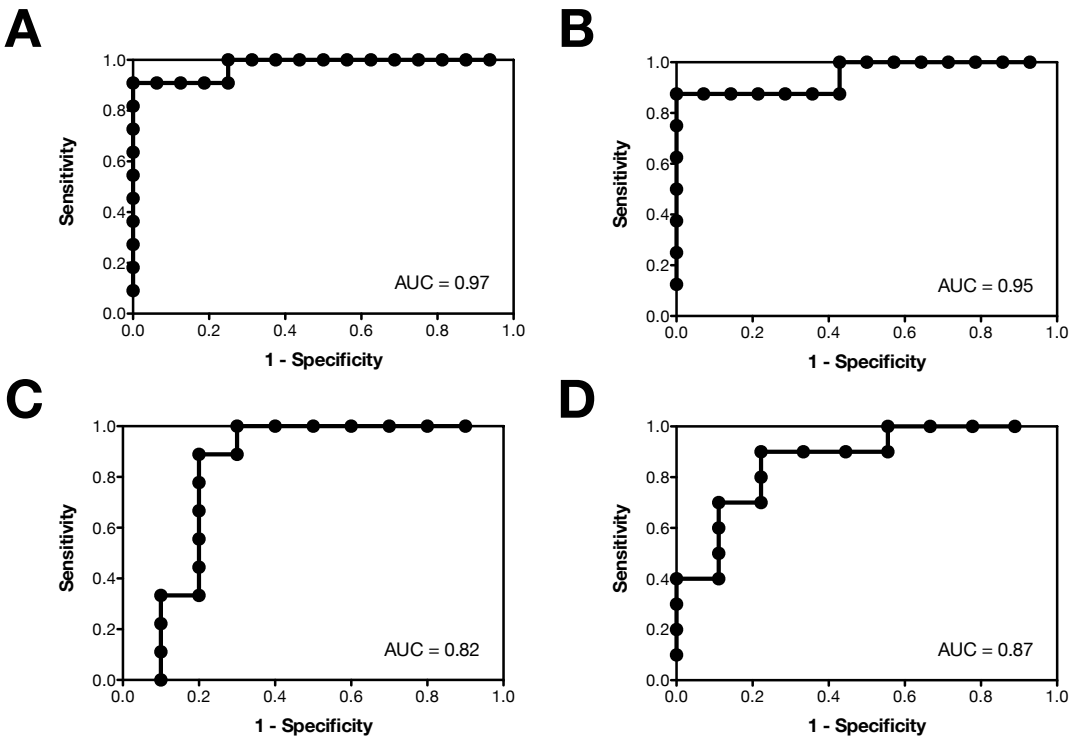

Figure 34: Receiver-operator characteristic (ROC) analysis shows high sensitivity in detecting tumor by accumulated indocyanine green (ICG). Three separate canine patients bearing a histiocytoma (A), neurofibrosarcoma (B), salivary carcinoma (C), and a myxosarcoma (D) were administered ICG 24 hours (A and B), 4 hours (C), and 2 hours (D) before surgery. The ROC analysis shows that there is high sensitivity in detecting tumors: an accepted false-positive rate of 30% gives sensitivities between 90–100%. The area under the curve (AUC) is a measure of diagnostic quality, and in all three cases is quite high.

the (low) ICG accumulation in normal tissue to the (high) ICG accumulation in neoplasia. The pharmacokinetics of ICG are known.[37] It is rapidly cleared from the plasma, within minutes of injection. It is likely that the ICG detected in the lymph node at the 4 hour interval is due to clearance of ICG from the tumor, where in murine models, it can persist for days (*c.f.* Figure 26 on page 75). These canine data would suggest that for the clinically important same-day injection of ICG, the dye accumulation may be able to locate lymph nodes but not inform on metastatic presence. The residual ICG in the lymph nodes would also preclude the use of local ICG injections for SLN mapping in a patient systemically injected with ICG for tumor resection. SLN mapping has been performed with isosulfan blue, an absorptive dye, as well as with technetium radiocolloids for radioscintography with great success for many years—the inability to do SLN mapping with short time interval systemic injections of ICG has no impact on the future clinical utility of this system and techniques.[222, 36, 135, 227] A related procedure, axillary lymph node dissection (ALND), would also be inadvisable to carry out with this instrumentation if same-day systemic injections of ICG are being used. The clinical efficacy of ALND in breast cancer has been recently shown to be less effective than originally thought;[151] it is therefore possible that ALND will in the future no longer be part of standard care.

4.4.2.2 Confounding issues in imaging canine cancer patients

Not all canine patients have shown significant contrast between tumor and normal tissue, but in these cases, there were identifiable confounding issues. In one early case, a schwannoma around the mandible, there was heavy bone involvement that attenuated ICG fluorescence. In another case, another myxosarcoma, the tumor margin marking dye (a colored India ink) obscured and attenuated ICG fluorescence. In several cases, the surgery performed was tissue-conserving (with the intention to follow up with radiation or chemotherapy), so while there were many neoplastic areas to sample, there were few or no normal areas to

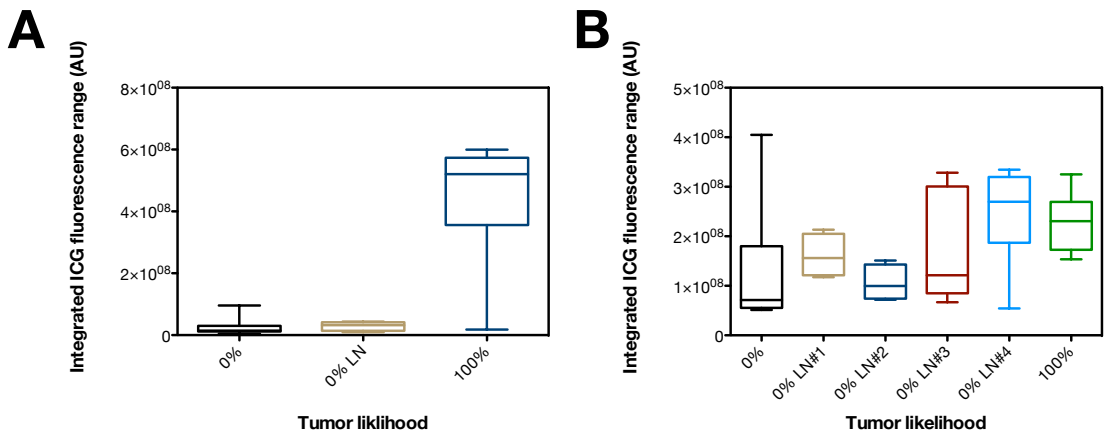

Figure 35: The indocyanine green (ICG) accumulation within canine lymph nodes is dependent on dosing interval. (A) A canine with neurofibrosarcoma was injected with 220 μg/kg ICG 24 hours before surgery. The lymph node recovered showed low accumulation of ICG and was pathologically free of metastatic disease. (B) A canine with salivary carcinoma was injected with 220 μg/kg ICG 4 hours before surgery. The lymph nodes recovered (all pathologically negative) show a range of ICG accumulation, between the range of normal and neoplasia in this patient. The boxes show the quartile range, the whiskers show the minimum and maximum values recorded.

sample; the opposite issue, nearly all normal areas with only a few tumor areas, also occurred in one case. None of these issues would not have arisen in murine tumor models, underscoring the value of a comparative oncology study.

There is tissue distortion during histology processing that confounds correlation between gross images and histology images. To overcome this issue, we recently have started taking punch biopsies of the surgical specimen and using these biopsies for the actual analysis. Another way to overcome this would be to use a "tissue scanner" to image the tissue before histology preparations with white light and for ICG fluorescence, mount the tissue for histology, and rescan the tissue. Computer algorithms can then match the before and after images of the tissue and generate a mapping of ICG within the tissue, taking tissue distortion into account.

Another item yet to be resolved is how to make comparisons between patients. Device calibration is simple and well described: there are industry and government methodologies

and standard reference materials for Raman and fluorescence calibration. Device calibration is only one half of the problem. Canines have greater genetic and physical variability than humans, and humans have greater variability than laboratory mice. Variations in ICG dosing between patients (*e.g.,* due to pharmacy handling) and in patient response to ICG (*e.g.,* due to disease burden beyond cancer) could alter the accumulation of ICG within normal tissues and the tumor. A way to reference measurements, taking ICG dosing between patients into account, would address the first point; the second point would require alterations to the research protocol to allow canine patients with underlying diseases to be enrolled and has additional patient safety burdens associated. We have recently attempted to find a well-perfused and universally accessible location to take measurements of ICG deposition in what is expected to be normal tissue in an attempt to establish a reference system. Finding a suitable location is in itself a challenge: many canines have pigmented skin that can interfere with the optical measurements. The buccal cavity is vascularized, universally accessible, and generally has areas of low pigmentation. We therefore tried using measurements of the gingiva, but the prevalence of gingivitis in canines due to poor preventative oral hygiene makes this a ill choice—inflamed tissues lose vascular integrity and become leaky. Another prospective location being investigated is the underside of the tongue.

4.5 Conclusions

In this chapter, we have demonstrated using proof-of-concept instrumentation that indocyanine green, an FDA-approved contrast agent (albeit in an off-label application) preferentially accumulates within tumors as verified by histology. ICG shows efficacy in murine tumor models as well as spontaneous canine tumors from a clinical population. Further developments of this instrumentation would be useful to determine the boundaries of a tumor during a surgical procedure. Being able to completely resect a tumor would reduce the need for follow up radiotherapy or chemotherapy, in itself improving patient care, as well

as decreasing the number of scar revision surgeries that would need to be performed. Since a “clean margin” is in many cases prognostic of surgical efficacy, improving the ability to effect a clean margin would be expected to greatly increase surgical cure rates.

CHAPTER V

DEGRADATION OF QUANTUM DOTS BY CHEMICAL OXIDANTS

5.1 Abstract

Semiconductor quantum dots are interesting for biological applications because of advantageous and unique optical and structural features in comparison to organic fluorophores. Optically, quantum dots have size- and composition-tunable emission wavelengths, large absorption cross sections, broad absorption spectra that permit facile multiplexing, and superior photostability to organic dyes. Structurally, quantum dots have a large surface area relative to volume that can be used for functionalization to one or more affinity ligands, enzymes, or other molecules. All of these properties are desirable for an *in vivo* fluorophore, however, toxicity concerns have stymied the deployment of quantum dots for human use. quantum dots are necessarily made of heavy metals known to be toxic (*e.g.,* cadmium, lead), but it has been unclear if the heavy metals making up a polymer-encapsulated nanocrystal are bioavailable and so subject to the same toxicity concerns as free heavy metal ions. In this chapter, we show that quantum dots can be rapidly degraded by hypochlorous acid , a chemical oxidant found biologically. The degradation process causes photoluminescence quenching; we also show that another process, photoannealing, can restore fluorescence in some cases. In Chapter 6, we will demonstrate that live cells can degrade quantum dots in a manner consistent with the "pure chemistry" experiments of this chapter, and we will describe the circumstances under which this degradation is expected to occur *in vivo*.

5.2 Introduction

Semiconductor quantum dots (QDs) first garnered attraction as biological labels based on a pair of studies published simultaneously in *Science* in 1998.[22, 33] These papers introduced two distinct water solubilization strategies that, when combined with high-quality QDs synthesized in organic solvents, permitted demonstrated applications in *in vitro* cell imaging. A few years later, following the development of more stable water-soluble surface coatings, the first *in vivo* use of QDs was reported.[63] Early on, concerns were raised about the possibility of toxic effects stemming from either the QD composition or the nanoparticles themselves (*i.e.,* in a composition-independent manner). Despite the concerns raised about QD toxicity in biological systems, few practical mechanisms for QD toxicity to be realized have been proposed. QD degradation through hypochlorous acid (HOCl), a biologically-produced oxidant, represents a realistic and achievable mechanism for QD degradation to occur *in vivo*, leading to the release of the heavy metal components of the QD in a known biologically-accessible form. A more comprehensive review of QD-related toxicity, as well as experimental findings of QD degradation, appears in Chapter 6—in this chapter, we are concerned with the chemistry of QD degradation.

Although QDs are a novel structure, the semiconductor materials making up common QDs have a long history of use in the semiconductor industry as bulk materials in camera sensors and solar panels. In semiconductor processing, a common step is to "etch" the substrate to remove material not protected by resist material; it is through repeated cycles of laying photoresist, etching, adding new material layers, washing and relaying photoresist, that semiconductor circuits are built. Wet etching of nanocrystals differs from bulk materials in that the nanocrystals have a corona layer of passivating organic material and surfactant (*e.g.,* trioctylphosphine oxide, TOPO), and in that a nanocrystal has numerous crystal facets exposed to possible etching, whereas the bulk material has a single crystal facet exposed. The corona layer can act as a steric barrier to etchants, and it can also be reactive towards the etchants. These differences both would be expected to lead to differences

in kinetic rates of the etching process.

Hypochlorous acid (HOCl) is familiar as household bleach, a weak acid and strong oxidant. In addition to using it as a laundering agent and general-purpose antimicrobial agent (*e.g.,* in maintaining swimming pools), it was investigated as a wet etchant for use with cadmium and zinc chalcogenides;[54, 55] it is not used presumably because the reaction proceeds too quickly to be well-controlled. HOCl is a member of the hypohalous acid family, which also contains hypofluorous acid (HFO), hypobromous acid (HOBr), and hypoiodous acid (HOI) in the "hypo" +1 halide oxidation state. Of the other halohalous acids, only HFO can exist in the pure form: the others exist only in aqueous solution, and in aqueous solution, exist in equilibrium with halo-oxo acids of other oxidation states (*e.g.,* hypochlorous acid exists with chlorous acid, chloric acid, and perchloric acid). In general, the hypohalite form of the halo-oxo acid (*i.e.,* the halo-oxo acid in basic water) is the form with greatest stability. Attempts to isolate hypohalous acids other than HFO result in the hypohalous acid disproportionating into other halo-oxo acids, anhydrous halooxygen compounds, forming salts, or into the diatomic halide proper. Halo-oxo acids have strong absorbances in the UV range that change depending on if the compound is in the protonated or neutral form—this strong absorbance also means that halo-oxo acids degrade rapidly when exposed to UV light or in sunlight.[1] Hypochlorous acid is somewhat unique in that it is a powerful oxidant (the Cl^-/HOCl redox potential is 1.495 V vs. SHE), relatively stable (*e.g.,* a bottle of commercial bleach is still usable after months), and possesses very fast reaction kinetics, especially against thiols. While H_2O_2 is a more powerful oxidant and is more stable, is has very slow reaction kinetics in comparison.[196, 265]

In this chapter, we will show how HOCl exposure quenches the QD fluorescence within seconds of exposure. In addition to quenching QD fluorescence, we will show that elemental analysis shows increases in the heavy metal ions that make up the QD in the solvent;

[1]This is why swimming pools need a constant, fresh supply of chlorine tablets and the pH must be balanced.

these increases are consistent with etching of the QDs and release of the components into the environment. Surprisingly, the reaction proceeds regardless of conventional QD protection strategy used (insulating shell material, polymer solubilization coatings, and QD material). Finally, we will show that the QD fluorescence can be restored in some cases by a process called "photochemical annealing" or "photoannealing";[149] the band-edge fluorescence of these quenched and then photoannealed QDs is hypsochromic relative to the unreacted QDs, consistent with a size decrease.

5.3 Methods

5.3.1 QD synthesis and water solubilization

CdSe QDs were synthesized by procedures described in the literature.[229, 173] The CdSe particles ("cores") were then purified from the crude mixture via precipitation in methanol, capped with a lattice-matching layer of CdS, and several insulating layers of ZnS. The core diameter was estimated to be 3.4 nm via optical absorbance, and the shell was estimated to be 1.75 nm thick for a total diameter of 6.9 nm. The final QDs had an emission peak of 618 nm and a full-width-at-half-maximum of 22 nm in chloroform. The QDs were phase transferred into water using previously-described methods to produce amphiphilic polymer-coated QDs, lipid-coated QDs, and polyethyleneimine-coated (PEI) QDs.[62, 229, 9] In the case of polymer-coated QDs, the polymer used (polyacrylic acid graft dodecylamine, PAA-*g*-DDA) is similar to the one used by Anderson and Chan with a 12-carbon alkyl graft.[9] The PAA-*g*-DDA coated QDs will be referred to as "polymer-encapsulated QDs" and these QDs are used throughout this dissertation unless otherwise specified. The detailed composition of these QDs is listed in Table 2 on the next page.

5.3.2 Reagent preparation

HOCl for QD quenching experiments was diluted from reagent grade stock in house deionized water (18.2 MΩ) that was treated with Chelex resin to remove transition metal ions. This stock solution was assayed by iodometric titration with sodium thiosulfate and by

Table 2: Optical properties and composition of quantum dots (QDs) used. Detailed composition and optical properties of the QDs used for fluorescence quenching and degradation studies. Diameter is approximate and is based on transmission electron microscopy measurements, atoms per QD is an estimate based on complete reaction of the QD precursor reactants, and the fluorescence peak and full-width-at-half-maximum (FWHM) measures are in chloroform. Reprinted with permission from ref. [148]. Copyright 2008 American Chemical Society.

Monolayer Number	Material	Diameter (nm)	Atoms per QD	Fluorescence Peak (nm)	FWHM (nm)
-	CdSe	3.36	468	572.9	23.7
1	CdS	4.06	826	580.6	25.8
2	CdZnS	4.76	1333	586.3	26.5
3	CdZnS	5.46	2013	595.6	23.1
4	CdZnS	6.16	2892	606.0	22.0
5	ZnS	6.86	3995	615.8	20.8

UV-vis absorbance of the stock solution in basic conditions (pH 12). H_2O_2 for QD quenching experiments was similarly diluted from reagent grade stock into Chelex-treated house deionized water. Phosphate buffer stock was made from monobasic and dibasic sodium phosphate diluted in house deionized water, with a pH adjustment to 7.4 made with 1.00M sodium hydroxide and a final treatment with Chelex resin before use. For UV-vis measurements, the molar extinction coefficient for HOCl was taken to be $\epsilon_{\mathrm{HOCl,\,292\,nm}}$ = 350 L $\mathrm{mol^{-1}cm^{-1}}$, and for H_2O_2, $\epsilon_{\mathrm{H_2O_2,\,240\,nm}}$ = 43.6 L $\mathrm{mol^{-1}cm^{-1}}$. Both diluted HOCl and H_2O_2 solutions were used fresh.

5.3.3 QD degradation by HOCl

5.3.3.1 Fluorescence change following HOCl and UV light exposure

Polymer-encapsulated QDs were diluted to a final concentration of 50 nmol/L in phosphate-buffered ultrapure water and reacted with molar ratios of HOCl up to 10,000 times the QD concentration (a maximum of 500 μmol/L). QDs exposed to HOCl were allowed to react for 30 minutes light-protected before measuring the photoluminescence intensity (PL) in a fluorometer and the absorbance in a UV-vis recording spectrometer. Following PL measurements, QDs were photoannealed by exposing the samples in glass vials under a

light stand approximately 6 cm from two 15 W UB-B bulbs for 10 minutes. The QDs were allowed to rest for 30 minutes in the dark before measuring both PL and absorbance again.

5.3.3.2 Elemental analysis of QD degradation products

Polymer-encapsulated QDs diluted in phosphate-buffered water were reacted with increasing concentrations of HOCl and allowed to react for one week light-protected and at ambient temperature. The solution was then filtered through a 10,000 MWCO centrifugal ultrafiltration membrane and the effluent was submitted for inductively-coupled plasma mass spectrometry (quadrupole) analysis at a core facility for Cd, Zn, and Se. S cannot be measured on a quadrupole instrument because sulfur is too close in mass to the Xe carrier gas.

5.3.3.3 Timecourse of QD degradation due to chemical oxidant exposure

Polymer-encapsulated QDs were diluted in phosphate-buffered water in a black plastic microtiter plate (96 well) and reacted with varying concentrations of either HOCl or H_2O_2 for up to 30 minutes at room temperature and light-protected. The microplates were then read at varying time points on a fluorometric microplate reader with appropriate fluorescence filters for QD detection.

5.3.3.4 Effect of QD surface coating on degradation due to HOCl exposure

QDs from the same batch of synthesis but with differing surface coatings were diluted into phosphate-buffered water in a black 96-well microtiter plate. They were then reacted with varying concentrations of HOCl for 30 minutes at room temperature, light protected. The microplates were then read on a fluorometric microplate reader with appropriate fluorescence filters for QD detection.

Commonly used surface coatings were selected for comparison. PAA-*g*-DDA is the "standard" polymer surface coating used for many commercially-available quantum dots,

described *supra*. Polyethyleneimine-graft-polyethylene glycol (PEI-*g*-PEG) is an amine-containing coating that displaces the alkyl surfactants remaining from QD synthesis, and was prepared as described by Duan and Nie.[62] Mercaptopropionic acid (MPA) is a small-molecule thiol that displaces the alkyl surfactants from QD synthesis, used in the earliest applications of QDs in biology and was prepared as described by Smith *et al.* [229] Lipid/PEG coated QDs of varying PEG content intercalate in the alkyl surfactants from QD synthesis, and were created with the lipids DPPC (1,2-dipalmitoyl-glycero-3-phosphocholine) and DPPE-PEG (1,2-dipalmitoyl-*sn*-glycero-3-phosphoethanolamine-*N*-methoxy(polyethylene-glycol)-2000). The percentage (40% or 100%) is the percentage of lipid PEG used in the feed for coating. The procedure used was from Smith *et al.*, an adaptation of a procedure by Dubertret *et al.* [229, 63]

5.3.3.5 Data analysis of microplate experiments

Microtiter plate (microplate) experiments all included a baseline reference (buffer solution only) that was used to calibrate the fluorometric plate reader photodetector. The microplate experiments also included a full-signal reference, typically QDs in buffer solution without additional treatment. Each data point consisted of at least 4 samples (n = 4), and was considered acceptable if the coefficient of variation (CV, $\%CV = 100 \times \frac{\bar{x}}{\sigma}$) was below 30%. The relative fluorescence remaining is the ratio of the mean fluorescence at each data point to the mean fluorescence of the full-signal reference.

5.4 Results and discussion

5.4.1 Phenomenological observations of QD fluorescence quenching

The finding that HOCl can lead to QD degradation was accidental: during characterization of QD surface charge (zeta potential) for an unrelated experiment, some samples lost fluorescence. The zeta potential measurement uses a voltage potential across a short electrode separation (*i.e.,* a high voltage gradient) to induce particle mobility; the applied voltage, in the presence of chloride ions present in the solution buffer, generates HOCl. This is the

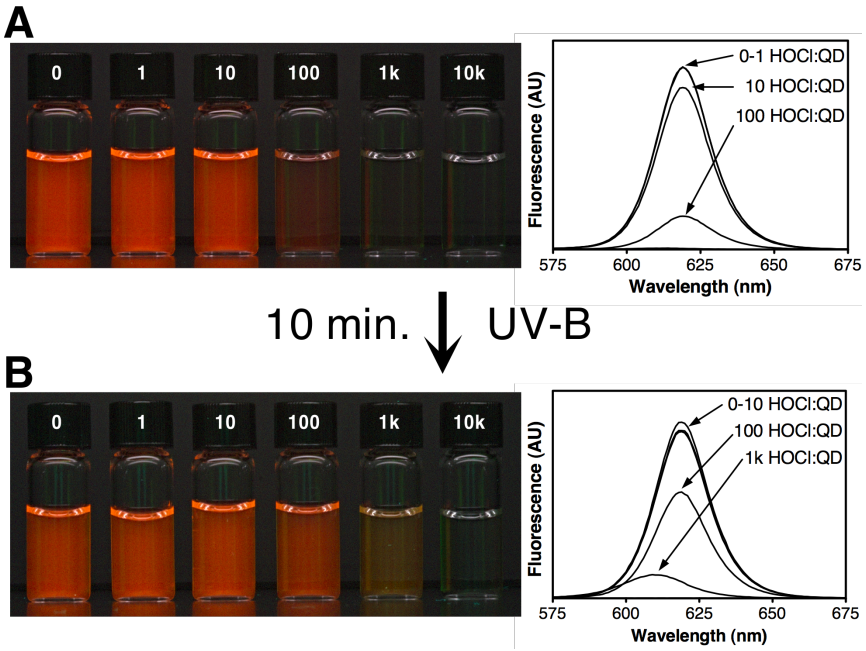

Figure 36: Hypochlorous acid (HOCl) exposure quenches quantum dot (QD) fluorescence but photoannealing restores it. HOCl causes fluorescence quenching of QDs in a dose-dependent manner (A), but the fluorescence can be partially recovered following UV-B illumination (B). The photographs show a series of vials containing dilute solutions of polymer-encapsulated QDs with increasing molar ratios of HOCl added to the solution (ratio is indicated above each vial). Increased concentrations of HOCl cause greater levels of fluorescence loss. The bottom photo shows the same exact vials after being exposed to UV-B light for 10 minutes. In addition to regaining fluorescence intensity in some samples, one sample ("1k", 1,000 HOCl molecules per QD) shows a blue-shift in the band edge fluorescence peak. The right side of the figure shows fluorescence spectra of the vial solutions photographed on the left. Reprinted with permission from ref. [148]. Copyright 2008 American Chemical Society.

chloralkali process, which is used to generate Cl_2 and HOCl commercially. That HOCl was being generated *in situ* was determined later through basic analytical chemistry. In addition to noting the loss of fluorescence in some samples, it was also noted that a subset of the samples which lost fluorescence regained it over time. It was later determined that the fluorescence recovery was caused by ambient fluorescent lighting inducing photoannealing. The "big picture" overview of this process is illustrated in Figure 36 on this page.

From a phenomenological standpoint, there are several interesting points about the HOCl-induced quenching process shown in Figure 36 on the current page. One is that

the process itself is very fast: QD fluorescence is quenched within seconds of the addition of HOCl (too fast to record without specialized equipment) and reaches completion within 30 minutes of exposure. Previous work by Derfus *et al.* showed that H_2O_2 can also lead to QD fluorescence quenching, however, this reaction takes days to go to completion and in even in the presence of a higher molar ratio of oxidant to QD, results in less fluorescence quenching as shown in 37.[56] Another surprising aspect of this reaction is that it occurs so quickly despite the QD crystal being encapsulated both by an aliphatic polymer and a hydrophobic surfactant. This might be because the pKa of HOCl is 7.53, so at the physiologic pH at which these experiments are carried out, approximately half will exist in a neutral form that can cross hydrophobic barriers.[169, 2] Another surprise is that the fluorescence can be recovered simply by exposing the samples to UV light, and not only does the fluorescence recover, but is in some cases accompanied by a shift in the band-edge fluorescence peak—in the case of Figure 36 on the preceding page, the sample treated with 1,000 HOCl per QD and photoannealed displays a hypsochromic band edge fluorescence shift of 10 nm. The location of the fluorescence peak is determined in part by the size and composition of the QD, and so the peak shift supports the idea that the QD size has decreased.

5.4.2 Measurements of bulk QD fluorescence quenching and degradation

Fluorescence quenching by HOCl exposure is rapid, occurring within seconds. We measured the effects of HOCl exposure on two synthesized batches of QD crystals, both with similar structures but synthesized years apart and polymer-encapsulated for water solubilization with different batches of polymer coating at different times. As shown in Figure 38 on page 100, the response profiles of both batches of QDs are indistinguishable. The QD615C crystal batch is the QD sample used in the analysis of QD degradation below and characterized in Table 2 on page 94; the QD620C crystal batch was used in some experiments described in Chapter 6. The fluorescence quenching reaction itself was also

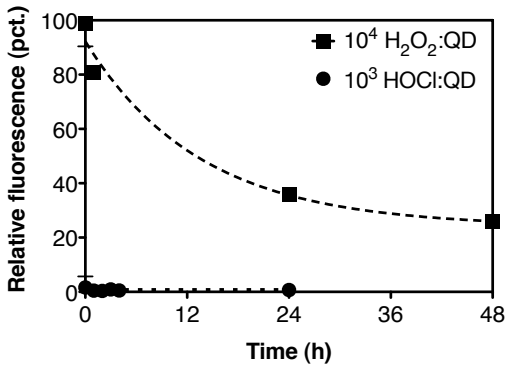

Figure 37: Time course of quantum dot (QD) degradation following exposure to hypochlorous acid (HOCl) or hydrogen peroxide (H_2O_2). Polymer-encapsulated QDs in phosphate-buffered water were exposed to specified concentrations of HOCl or H_2O_2 and allowed to react over a period of two days. Note that the molar ratio of HOCl added to the QD solutions, 1,000, is one-tenth that of H_2O_2 added. Error bars show the 95% confidence interval (n = 4) and the lines of fit are drawn solely as a visual guide.

carried out one year apart, using different batches of HOCl, phosphate buffer, and water supply. The core/shell structures of both QD crystals are similar, so the identical reaction profile towards HOCl is expected. In both cases, a loss in fluorescence is detectible at a molar ratio of 10 molecules of HOCl per QD, and fluorescence becomes difficult to detect on the instrument used beyond 1,000 HOCl per QD.

Measurements of the UV-vis absorbance spectra of QDs exposed to HOCl shown in Figure 39 on page 101 show that as the exposure level of HOCl increases (1,000 HOCl per QD), the first exciton peak decreases in absorbance and the peak becomes more blue-shifted: taken together, these are signs of the QD core decreasing in size. Interestingly, this same exposure level is the same exposure level that shows significant band-edge fluorescence peak shift with photoannealing as shown in Figure 36 on page 97. With overwhelming exposure to HOCl, the absorbance spectra becomes featureless, consistent with complete destruction of the QDs. Elemental analysis of QD solutions treated with HOCl and then filtered to remove intact QDs confirms the UV-vis spectroscopy findings that suggest QDs degrade in the presence of HOCl. As shown in Figure 40 on page 101, increasing exposures of HOCl liberate increasing amounts of the metals (Cd, Zn) and chalcogens (S,

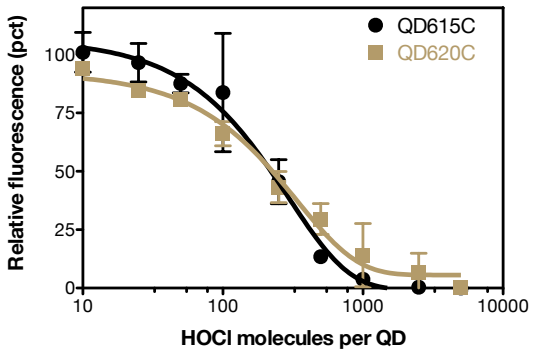

Figure 38: Fluorescence quenching in quantum dots (QDs) exposed to hypochlorous acid (HOCl). QDs were diluted into physiologic pH phosphate-buffered water and reacted with indicated molar ratios of HOCl. The QDs reacted are from two different synthesis batches, and the reactions were carried out completely independently. Non-linear regression lines are a one-phase exponential decay model, error bars show the 95% confidence interval (n = 4), and Pearson's correlation coefficient for both non-linear regressions is 0.98. The best-fit exponential decay constant between the two regressions are the same, with 64% probability as calculated by Akaike's informative criteria, corrected (AICc).

Se) which make up the QDs. Importantly, the stoichiometric ratios of the atoms liberated matches well with the expected chemical composition of the QDs used in this study, $Cd_{0.65}Zn_{0.35}Se_{0.35}S_{0.65}$, described layer by layer in Table 2 on page 94. The amounts of each element are lower than would be expected, however, the polymer used for encapsulating the QDs can still chelate free metal ions, and during the separation process the polymer (with chelated ions) could remain in the retentate of the separation. The band-edge fluorescence peak shift observed in Figure 36 on page 97 after photoannealing QD reacted with 1,000 HOCl per QD, 609 nm emission (*c.f.* the unreacted QDs with band-edge emission of 619 nm) is consistent with the loss of the outer ZnS layer of the QD based purely on fluorescence data from Table 2; the characterization table also estimates approximately 1,000 atoms in the outer ZnS shell of the QD, approximately half which would be S and able to react with HOCl—on the same order as the molar ratio of HOCl added per QD.

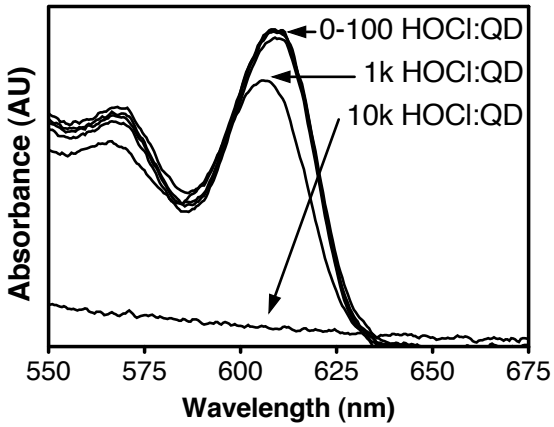

Figure 39: Ultraviolet-visible (UV-vis) absorbance spectroscopy of quantum dots (QDs) exposed to hypochlorous acid (HOCl). UV-vis absorption spectroscopy of phosphate-buffered QDs exposed to HOCl shows that at a molar ratio threshold of 1,000 HOCl molecules per QD, there is a noticeable decrease in intensity and blue-shift in the first exciton peak of the QDs (noted with arrows), both indicative of a decrease in QD size. An excess (10,000) of HOCl molecules per QD results in a featureless and broadband absorption spectrum consistent with scatter, suggesting complete QD destruction. Reprinted with permission from ref. [148]. Copyright 2008 American Chemical Society.

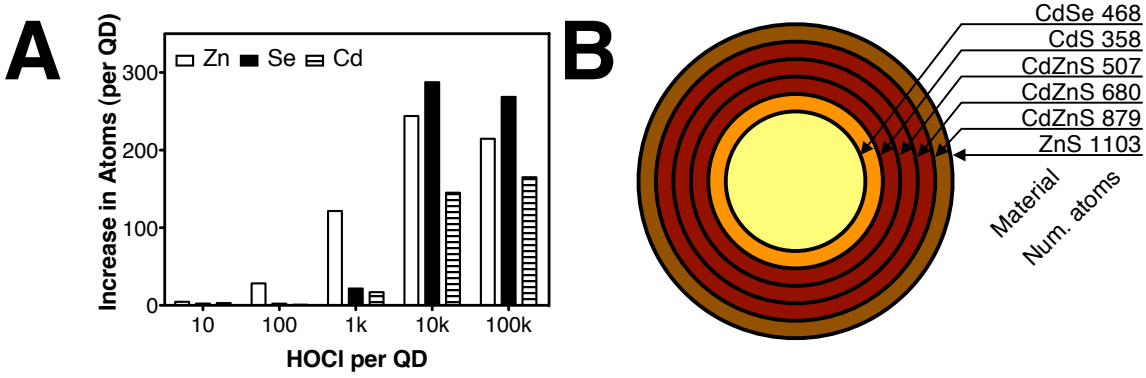

Figure 40: Elemental analysis of quantum dot (QD) solutions after exposure to hypochlorous acid (HOCl). (A) Elemental analysis by inductively-coupled plasma mass spectrometry (ICP-MS) shows that there is an increase in the free ions making up QDs in solution that correlates with an increased molar ratio of HOCl molecules added to the solution. The ratios of the ions are consistent with the QD chemical composition, taking into account the core/shell structure of the QDs tested. (B) In outer shell layers of the QD there is an excess of Zn relative to the other elements, so moderate amounts of HOCl (1,000) would be expected to liberate mostly zinc, whereas more HOCl (10,000) is needed to liberate the Cd and Se in the core of the QD. Panel (A) reprinted with permission from ref. [148]. Copyright 2008 American Chemical Society.

5.4.3 Common QD surface coatings do not prevent degradation by HOCl

A surprise in studying degradation of QDs by HOCl exposure is the relative insensitivity of the reaction to the surface coating of the QDs. High-quality QDs are synthesized in organic solvents, and are by nature soluble only in non-aqueous solvents. To make these QDs water soluble, they are either re-coated with a water-soluble ligand (usually called a "small ligand exchange"), or coated with a polymer or surfactant that intercalates with the hydrophobic alkyl surfactant layer surrounding the QDs and simultaneously presents a water-soluble moiety: in the case of PAA-*g*-DDA, this moiety is the carboxylates of polyacrylic acid, in the case of phospholipids, this is the charged phosphate group of the phospholipid head group. We tested the response of QDs coated with common surface coatings to degradation by HOCl. The surface coatings tested can be divided into two groups: those that displace the alkyl surfactant layer from QD synthesis, and those that preserve it. Polyethyleneimine (PEI) is a branched amine-rich polymer that displaces the QD alkyl surfactant layer and confers water solubility with good quantum yield (QY); we tested a variant of PEI grafted with 2000 kD PEG side chains that make the overall QD surface charge more neutral than the positive PEI coating.[62] Mercaptopripioic acid (MPA) is a small-molecule thiol that displaces the QD alkyl surfactant layer and is only slightly larger than the mercaptoacetic acid (MAA) water-solubilization strategy used in the first biological QD application articles.[33] PAA-*g*-DDA is a polymer coating that has a alkyl moiety that intercalates in the alkyl surfactant layer of the QD, an acrylic acid backbone, and carboxylate moieties that provide water solubilization; it is very similar or identical to the polymer surface coatings used by commercial QD manufacturers. Lipid-coated QDs are a micellar structure using the alkyl surfactants of the QD and phospholipids added to confer water solubilization; they are available commercially and are in general quite "inert" biologically. The form tested had lipids grafted to PEG chains with varying feed ratios for the QD coating procedure.

As shown in Figure 41 on the following page, regardless of the coating, QDs exposed

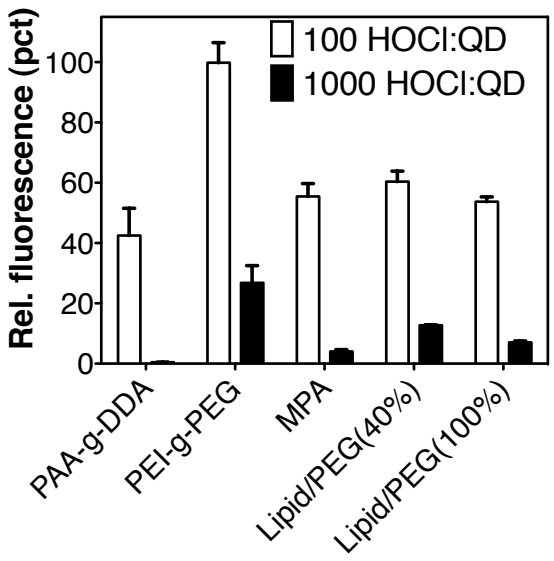

Figure 41: Altered surface chemistry is insufficient to protect quantum dots (QDs) from hypochlorous acid (HOCl) attack. QDs from the same batch of synthesis were coated with several different and common surface coatings, then tested for fluorescence quenching following HOCl exposure at the indicated molar ratios. PAA-*g*-DDA is polyacrylic acid-graft-dodecylamine; PEI-*g*-PEG is polyethyleneimine-graft-polyethylene glycol (2,000 kD MW); MPA is mercaptopropionic acid; lipid/PEG is a phospholipid coating with varying graft ratios of 2,000 kD MW PEG. Error bars show the 95% confidence interval (n = 4). Reprinted with permission from ref. [148]. Copyright 2008 American Chemical Society.

to HOCl rapidly degrade even in moderate levels of HOCl. The PAA-*g*-DDA surface coating, in many applications one of the most stable surface coatings, actually performs the worst. Both PEI-*g*-PEG and MPA perform well in comparison; both have functional groups (amine and thiol, respectively) that are targets of oxidation by HOCl. In effect, both surface coatings "buffer" the QD surface from HOCl oxidation. The small molecule thiol coatings are commonly one of the less-stable surface coatings both by colloidal and optical measures.[229] In the case of lipid/PEG coatings, there is a considerable steric interference offered by the QD alkyl surfactant layer (in this case, a mix of hexadecylamine and octadecylamine), the phospholipids (palmitic acid base, 16 carbons long), and the grafted PEG (2000 kD MW).

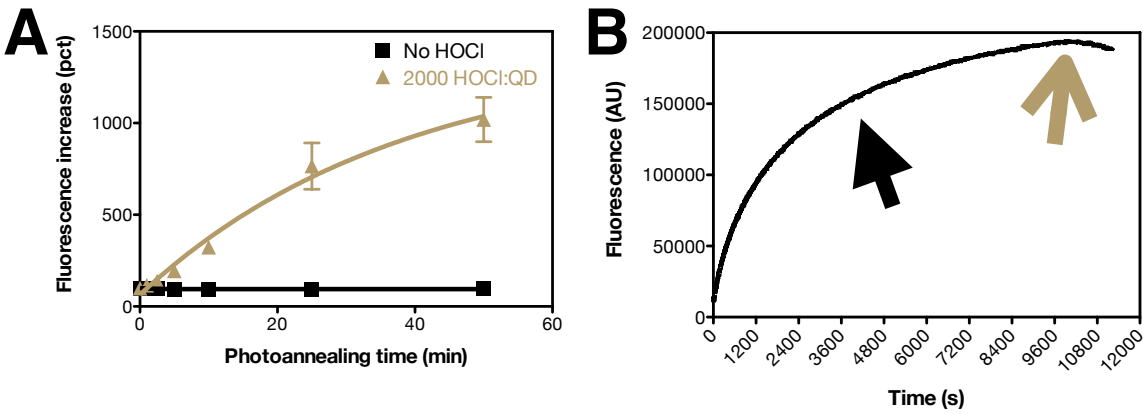

Figure 42: Photoannealing degraded quantum dots (QDs) results in restoration of fluorescence. (A) QDs were exposed to 2,000 molecules of hypochlorous acid (HOCl) per QD and photoannealed by exposure to UV-B light for the specified time intervals. The QDs exposed to HOCl showed a dramatic fluorescence increase (relative to the original emission strength). Error bars show 95% confidence intervals, n = 3, and lines are a one-phase exponential regression fit provided solely as a visual guide. (B) A single sample of QDs were exposed to HOCl and photoannealed while the fluorescence emission was continuously tracked. The solid black arrow marks a kink at which the excitation volume becomes saturated with photoannealed QDs—beyond this point, fluorescence increase due to photoannealing previously "dark" QDs is diffusion limited. The open gold arrow shows the point at which the entire sample has photoannealed, beyond this point, photooxidation occurs.

5.4.4 Observations on single particle and bulk QD photoannealing

The time course in which photoannealing occurs was first tested using UV-B light provided by a germicidal light stand. As shown in Figure 42 on the current page, significant fluorescence increases are observed in the QD samples treated with HOCl, whereas samples not treated with HOCl have only minute fluorescence increases. It should be noted that these fluorescence increases are relative, so while the HOCl-treated QDs may increase in fluorescence by 10 fold, they are still considerably dimmer than the unreacted QDs (shown in Figure 43 on the following page, inset). Continuous tracking of a single QD sample, also shown in Figure 42 on the current page, shows that the fluorescence rise is exponential-like, before plateauing and then decreasing (presumably due to photooxidation). In addition to a fluorescence increase, there is also a shift in the band edge fluorescence peak that becomes

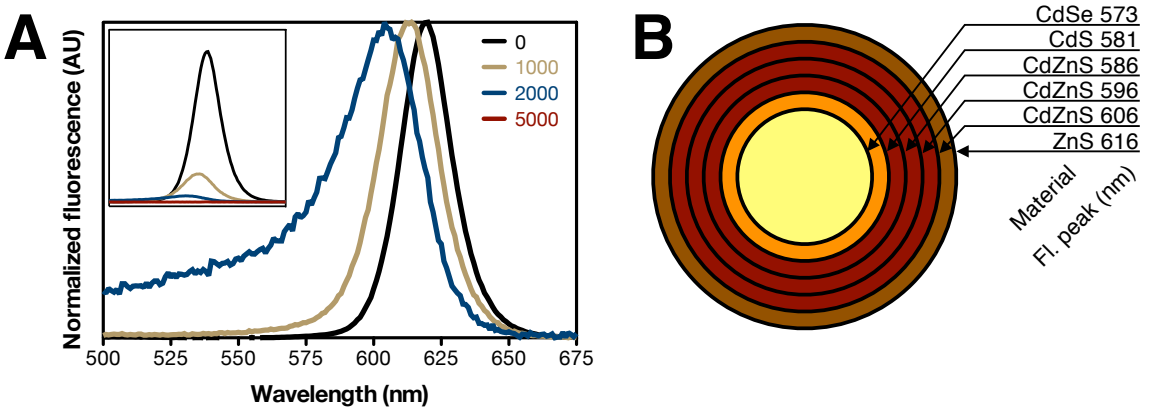

Figure 43: Photoannealing degraded quantum dots (QDs) results in fluorescence peak shifting and broadening. (A) QDs were exposed to specified molar ratios of hypochlorous acid (HOCl) per QD and photoannealed by exposure to UV-B light for 10 minutes. The band edge fluorescence peak shifts up to 20 nm, and in the furthest shifted sample, shows a significant blue tail. In the inset for A is the unnormalized spectra so that the relative quantum yields may be observed. (B) Correlation between band edge fluorescence peak (in chloroform) and layer-by-layer structure for the QDs in A.

visible only after photoannealing. The peak shift is dependent on the amount of HOCl reacted with the QDs, as shown in Figure 43 on this page, and is roughly correlated with the known layer-by-layer band edge fluorescence of the QDs from synthesis.

QDs are distinct from organic dyes such as rhodamine in that QDs are a population of particles with a range of core sizes, shell thicknesses, surface passivation, *&c.*, whereas organic dyes are all identical. The variation in the properties of a population of QDs would naturally be assumed to lead to a variation in the behavior of QDs exposed to HOCl. As such, we examined the single particle and ensemble (a population of singly-identifiable particles) behavior of QDs exposed to HOCl and reconciled these results with the bulk behavior. In terms of fluorescence quenching, single particle observations in a fluorescence microscope showed that the blinking rate of QDs changes dramatically on addition of HOCl, decreasing the duty cycle of the QDs and in effect, lowering the quantum yield of the bulk solution. Attempts were made to investigate the alteration in blinking rates, but the changes were too subtle to detect on the laboratory equipment available. It must be noted however that these observations were made under QD excitation, and so the QDs are

undergoing photoannealing at the same time they are being chemically oxidized.

Deliberate photoannealing of the QDs that were treated with HOCl explains the altered shape of the bulk solution QD fluorescence peak following photoannealing, depicted in Figure 44. The bulk QD spectrum following photoannealing, in addition to a 15 nm shift in the main band-edge fluorescence peak, has a distinct "blue tail" that is not observed in the untreated QDs. Ensemble observations of QDs under the microscope showed that the photoannealed QDs had visible fluorescence spanning a range of colors, from green to red, shown in Figure 45. Smaller (bluer) QDs have lower quantum yields than larger (redder) QDs, all other things being equal, and in this case, the smaller QDs are produced by chemical etching and so may have an even lower QY due to defects remaining on the QD related to the etching process and to loss of the passivating layers of the QD shell. Therefore, the "blue tail" can be explained as being due to the presence of a range of QD sizes and structures, with higher QY particles closer to the band edge fluorescence peak, and lower QY particles farther from the band edge fluorescence peak.

5.4.5 Mechanism of QD degradation by HOCl exposure and restoration of fluorescence by photoannealing

The group IV-VI QDs used in this chapter (and throughout this dissertation) contain chalcogens (S, Se). HOCl is known to have extremely fast reaction kinetics in oxidizing chalcogens, and so it is reasonable to expect that HOCl is oxidizing exposed chalcogens on the surface. Since HOCl is relatively small and can exist in a neutral acid form at the physiologic pH in which these experiments are carried out, it is understandable that HOCl could penetrate the polymer and alkyl surfactant shell (corona) surrounding the QD. The corona layer also has potential targets for oxidation, amines of the alkyl surfactants in the case of the polymer-encapsulated QDs used. Curiously, altering the surface chemistry has little effect on the end-result of HOCl exposure, but this probably has much to do with the reaction kinetics of HOCl being faster for thiols than for amines or unsaturated/aromatic carbon–carbon bonds.[196] Once HOCl reacts with an exposed chalcogen on the surface

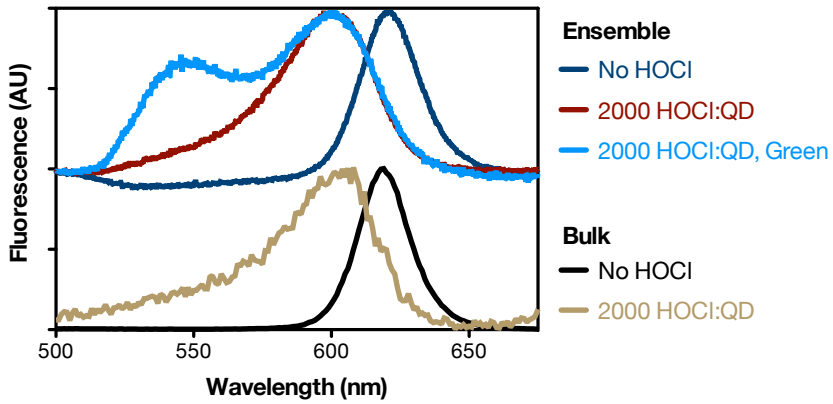

Figure 44: A comparison of the bulk and ensemble fluorescence spectra of photoannealed quantum dots (QDs). QDs were reacted in bulk solution with a molar ratio of 2,000 HOCl molecules per QD, photoannealed with 10 minutes of UV-B exposure from a UV light stand, and then measured on a fluorometer ("Bulk") or on a microscope with a 100X objective ("Ensemble") and equipped with a spectrograph. Bulk and ensemble spectra show good agreement. The "Green" sample is a spectrograph reading of a bright green QD observed in the microscope and is shown to illustrate how the range of QD emission profiles, summed together, can explain the blue tail associated with the photoannealed QD band-edge fluorescence peak.

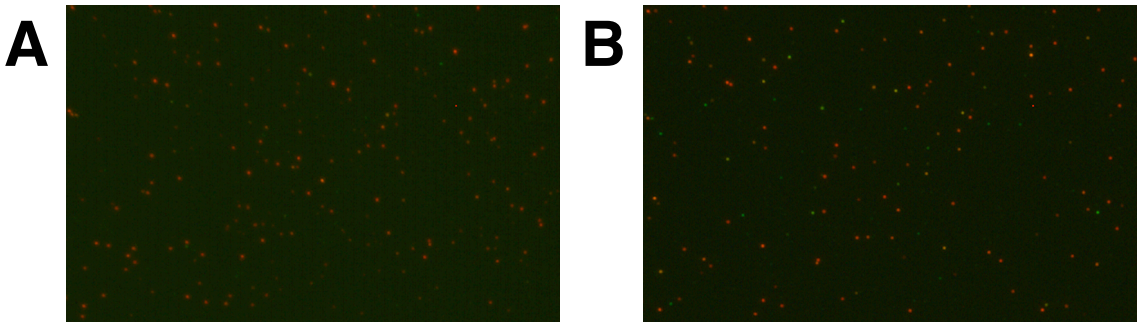

Figure 45: Micrograph of quantum dots (QDs) before and after photoannealing. (A) QDs adsorbed to a glass coverslip were imaged with a 100X objective before addition of HOCl. Following HOCl addition, QDs were allowed to photoanneal using UV-C excitation light for 5 minutes, then imaged again. (B) After etching with HOCl and photoannealing, the ensemble of QDs shows a range of fluorescence colors in comparison to the single color of the unreacted QDs. Images were digitally adjusted for brightness and contrast with identical settings used for both images.

of the QD, this oxidation site can act as a trap for the exciton, immediately quenching QD fluorescence.[234] Photoannealing is clearly a correction of this defect, but the exact mechanism is still elusive. Photoannealing unconnected to the HOCl reaction has been observed previously, but was explained as a "structural rearrangement."[149] It is possible that photoannealing represents the ejection of the oxidized chalcogen, similar to very early observations of macroscopic CdS electrodes undergoing photocorrosion.[103, 213] This would make the surface of the QD metal rich, favoring luminescence.

5.5 Conclusions

The degradation of semiconductor quantum dots by exposure to hypochlorous acid is unique in the fast kinetics and high efficiency of the reaction, and in the relative insensitivity of the QD crystal material or solubilizing ligands. Beyond the obvious contra-indication of using QDs in an environment containing HOCl (or in electrophoretic potential measurements), the data presented in this chapter demonstrate that while QDs may be superlatively photostable, they are not invincible in terms of chemical stability. In addition to independently replicating results presented here and in Chapter 6 (published in part in 2008), two groups have published extensions of this work into new areas.[41, 273] The relevance of this reaction in the biological context, a prime application of colloidal QDs, will be explored in Chapter 6. Restoring the fluorescence to QDs through photochemical annealing could prove to be useful in sensing applications (*i.e.,* determine the amount of QD degradation and so estimate the quantity of HOCl present, as was done in ref. [273]) and in basic research into the role of surface defects on QD fluorescence emission. Control over the emissive state of fluorophores is also important for both optoelectronics applications (*e.g.,* optical memory) and in super-resolution microscopy and it is possible that the QD/HOCl interaction could lead to QD adoption for these applications.

CHAPTER VI

DEGRADATION OF QUANTUM DOTS BY BIOLOGICAL PROCESSES

6.1 Abstract

The advantageous optical and physical properties of semiconductor quantum dots makes them desirable for use as optical contrast agents for *in vivo* human imaging, however, the toxic composition of quantum dots prevents the use of quantum dots for this application. These concerns existed despite a well-defined mechanism for the breakdown of quantum dots *in vivo* into their substituent materials that are known to be toxic. The toxicity associated with the presence of the particles themselves is also a factor and must be considered. We have described in Chapter 5 how quantum dots are rapidly degraded by exposure to hypochlorous acid. Hypochlorous acid is a biologically-relevant chemical, generated by phagocyte cells of the immune system as an antimicrobial compound. Quantum dots are known to be sequestered by immune cells when systemically-injected, and so it is possible that quantum dots could be degraded *in vivo* by immune cells via a process involving hypochlorous acid. In this chapter, we explore the sensitivity of quantum dots to degradation by a range of biologically-relevant reactive chemicals, we demonstrate that quantum dots can be degraded by cells in *in vitro* models, and we investigate the limitations of degradation by these processes. We find that cellular processes can cause quantum dot degradation, but that the rate of degradation is far slower than is observed in the "test tube" cell-free systems of Chapter 5. Thus, degradation of quantum dots by immune cells is expected to take long time periods *in vivo* and require pathophysiologic conditions to generate sufficient oxidants to cause degradation.

6.2 Introduction

Semiconductor quantum dots (QDs) are interesting for use as an *in vivo* imaging probe, including for human applications, however the toxic semiconductor components making up the QD and the tendency of QDs to biopersist make regulatory approval unlikely. An analogy is commonly made between using QDs for imaging and medical technology with known toxic side effects, *e.g.,* gadolinium chelates used in magnetic resonance imaging. The difference is that chelates of gadolineum are known to be relatively non-toxic (unlike free gadolinium which is quite toxic) and the chelates are cleared from the body with well-defined kinetics. Gadolinium chelates are still used despite the possibility of nephrogenic systemic fibrosis, a serious complication with a yet to be determined cause.[201] If QDs were shown to remain intact *in vivo* until cleared (in an intact state), it could improve the odds of gaining regulatory approval for QD use in humans. Despite the concerns related to the toxic components of QDs, it has not been clear how QDs would cause toxicity *in vivo*. While it is true that some of the constituent atoms making up the QD are known to be toxic, it is not clear that the atoms when in crystalline form are equally toxic. Numerous toxicity studies have been conducted, but a clear consensus of QD toxicity has yet to emerge.[95] Part of the difficulty is because heavy metal toxicity is in general a chronic disease that takes years to present. Another major confounding factor is the considerable chemical and structural variation in QDs used between different research groups.

In Chapter 5, we showed how hypochlorous acid (HOCl) could rapidly degrade QDs and release the semiconductor materials making up the QD into the environment. HOCl is one of many reactive oxygen species (ROS) found in the body, generated by the haloperoxidase enzyme family. Notably, two enzymes in this family, myeloperoxidase (MPO) and the related eosinophil peroxidase (EPO), are found in immune cells.[131, 212] MPO is found in the azurophilic granules of neutrophils (where it can make up to 5% of the dry weight of a neutrophil) and in monocytes (the progenitor cell of macrophages); the similar EPO is found in azurophilic granules of eosinophils and is capable of generating hypobromous

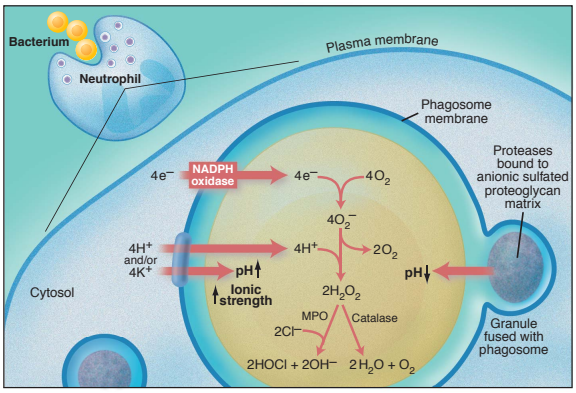

Figure 46: Phagocytes engulf foreign bodies and release an array of antimicrobial compounds. A neutrophil engulfs a bacterium, forming a phagosome. Granules fuse with the phagosome, releasing compounds that can generate reactive oxygen species (ROS). By forming a phagosome, the cell can create high local concentrations of ROS, and better control the reaction. From Roos and Winterbourn, ref. [209]. Reprinted with permission from AAAS.

acid (HOBr) in addition to HOCl.[154, 255] It is theorized that the purpose of both enzymes is to generate hypohalous acids *in situ* to kill foreign organisms, as shown in Figure 46 on the current page—individuals with a genetic deficiency in MPO (chronic granulomatous disease) have increased susceptibility to opportunistic diseases associated with individuals having compromised immune systems (e.g., aspergillosis, candidiasis).[193, 178] In this chapter, we will focus on MPO as a representative haloperoxidase: EPO is found only in eosinophils (which represent no more than 5% of circulating leukocytes) whereas MPO is found in both neutrophils and monocytes (representing approximately 65% of circulating lymphocytes). MPO catalyzes the production of HOCl in the presence of chloride ions (found endogenously at approximately 140mM concentration), and H_2O_2, generated *in situ* by phagocytes during the "degranulation" process of phagocytosis.

Since both HOCl and H_2O_2 can degrade QDs, and both compounds are considered biological ROS, we became interested in all biological ROS for their ability to degrade QDs. Nitric oxide (·NO) is synthesized by nitric oxide synthases (NOS) in the body for signaling and antimicrobial purposes; in the case of macrophages, the enzyme isoform is inducible NOS (iNOS). Superoxide ($\cdot O_2^-$) is used as an antimicrobial agent by granulocytes and

Table 3: Sources and biological oxidants assayed for QD degradation

Oxidant	Pathophysiologic concentration	Biological source	Chemical source
HOCl	1–1000nmol/L	haloperoxidases	Pure reagent
·NO	10–1000nmol/L	nitric oxide synthases	Angeli's salt
$\cdot O_2^-$	1–100nmol/L	NADPH oxidases	KO_2
$ONOO^-$	10–100nmol/L	·NO + H_2O_2	Pure reagent
H_2O_2	10–1000nmol/L	$\cdot O_2^-$ + superoxide dismutase	Pure reagent
·OH	Unknowm	H_2O_2 + iron(II)	H_2O_2 + iron perchlorate

macrophages and is generated by the NADPH (nicotinamide adenine dinucleotide phosphate) oxidase (NOX) system. At physiologic pH, $\cdot O_2^-$ exists mostly in the anion form. In the presence of water, $\cdot O_2^-$ disproportionates into oxygen and H_2O_2—this process is catalyzed by the metalloenzyme family superoxide dismutase (SOD). Peroxynitrite ($ONOO^-$) is not a radical but is a powerful oxidant; it is formed by the adduction of ·NO and $\cdot O_2^-$. At physiologic pH, $ONOO^-$ is in the unstable ionic form which has a half-life of 1.9s.[16] Finally, hydroxyl radical (·OH) is the most reactive ROS found in the body, presumably produced through a variant of Fenton's reaction between H_2O_2 and iron(II) and through reaction of HOCl with $\cdot O_2^-$.[92] Hydroxyl radical is so reactive that it is exceedingly short-lived: its half life in aqueous solutions is on the order of nanoseconds, implying a mean diffusion distance in pure water of 10 angstroms. The extreme reactivity of ·OH also means that the *in vivo* concentration is unknown. All of these ROS, summarized in Table 3 on this page are generated during the "oxidative burst" (a period of high oxygen consumption) of phagocytosis, where phagocytes fuse the primary vesicles containing enzymes and precursors with the phagosome containing engulfed foreign bodies; some of these ROS can also be generated elsewhere in the body as signaling molecules (*e.g.,* ·NO is also known as endothelium-derived relaxing factor).

If QDs were to be used as a contrast agent for *in vivo* imaging, they could be used

as either a passive or active targeting contrast agent, and would presumably be systemically injected. Once injected, QDs encounter endothelial cells lining the blood vessels, erythrocytes (red blood cells) ferrying oxygen to tissues and carbon dioxide away, leukocytes (white blood cells) that are involved in the immune response, platelets responsible for wound healing, and any number of serum proteins. Many serum proteins are known to bind to nanoparticles, and some of these serum proteins are part of the the immune system (antibodies, complement proteins).[60] QDs injected *in vivo*, like most nanoparticles, are soon sequestered by immune cells in the liver and spleen, and mechanically filtered and retained in the kidneys.[164, 163] The liver is rich in Kupffer cells, a type of resident macrophage (and so of monocyte origin);[174] the spleen is a reservoir of monocytes.[243] While not all monocyte-derived cells have MPO, Kupffer cells do.[21] The immune cells in these organs (classically referred to as the reticuloendothelial system, RES, now referred to as the mononuclear phagocyte system, MPS) are designed to recognize and filter foreign bodies from the blood. It is thus possible that the body may be able to degrade QDs by the existing foreign body response (nanoparticles are after all foreign matter). Previous work has shown that QDs in cell culture models of the liver can be degraded following phagocytosis, however, earlier work only considered H_2O_2 and the immune response was ignored.[56] As was discussed in Chapter 5, H_2O_2 degradation of QDs occurs over a time span of days, whereas HOCl-mediated degradation occurs over much shorter time periods as was shown in Figure 37 on page 99.

In this chapter, we will consider the degradation of QDs by HOCl and other biological oxidants associated with resident macrophages (as has previously been considered), as well as circulating granulocytes and endothelial cells. Unlike many studies which use easily manufactured cadmium telluride QDs, which are well-known to be fragile and prone to degradation simply by being in aqueous solution, we will use polymer-coated core/shell QDs that are similar to commercially available QDs.[226, 279, 147, 278] These polymer-coated QDs are ordinarily extremely stable and are more likely to be of a kind useful for

human *in vivo* use.

6.3 Methods

6.3.1 Degradation of QDs *in vivo* by a panel of biological ROS

QDs crystals were the same particles synthesized, described, and used in Chapter 5, and used the PAA-*g*-DDA polymer coating. QDs were diluted into phosphate-buffered water at pH 7.4 (described as "physiologic buffered") in a black microplate, to which ROS were added. ROS were sourced as follows: HOCl was diluted from reagent-grade stock; ·NO was generated by the ·NO donor Angeli's salt (disodium diazen-1-ium-1,2,2-triolate) diluted into house deionized water and used immediately; $\cdot O_2^-$ was diluted from potassium superoxide diluted in basic water; $ONOO^-$ was synthesized by oxidation of nitrous oxide by hydrogen peroxide in alkaline conditions with a subsequent freeze fractionation workup;[114] H_2O_2 was diluted from reagent-grade stock; and ·OH was generated by Fenton's reaction with the same concentration of H_2O_2 as in the H_2O_2 sample. HOCl, $ONOO^-$, and H_2O_2 were assayed for concentration by UV-vis absorbance spectroscopy. The molar extinction coefficients used were $\epsilon_{HOCl,\,292\,nm}$ = 350 L $mol^{-1}cm^{-1}$, $\epsilon_{ONOO^-,\,302\,nm}$ = 1670 L $mol^{-1}cm^{-1}$, $\epsilon_{H_2O_2,\,240\,nm}$ = 43.6 L $mol^{-1}cm^{-1}$.

6.3.2 Degradation of QDs by the MPO enzyme system

QDs were diluted into phosphate-buffered saline (PBS) in black microplates, to which components of the MPO enzyme system were then added. MPO was obtained commercially, isolated from human leukocytes. Activity was confirmed spectrophotometrically by oxidation of guiacol in the presence of H_2O_2, as per a protocol recommended by the manufacturer and described by Desser *et al.* [57] MPO, H_2O_2, and 4-aminobenzoic acid hydrazide (ABAH) were diluted into house deionized water (18.2 MΩ) before addition to the QDs/microplate, and were allowed to react one hour at room temperature, light protected, before reading in a fluorometric plate reader.

6.3.3 Cell culture for live cell experiments

HL-60 cells, derived from a human promyelocytic leukemia, were obtained commercially. [44] The main cell line was maintained in a standard incubator, maintained at 37 degrees Celsius and with a 5% CO_2 atmosphere. Standard medium for culturing was Isocove's modification of Dulbecco's-modified Eagle's medium (IMDM), supplemented with 20% fetal bovine serum (FBS) and no antibiotics. Cells were maintained, suspended in culture flasks, between 1×10^5 and 1×10^6 cells per milliliter, counted by automated cell counter. Cryopreservation was performed using standard technique using the normal growth medium supplemented with 5% dimethylsulfoxide (DMSO), cell culture grade, as a cryopreservant. On awakening, the cells were centrifuged to pellet and washed with balanced salt solution several times to remove excess DMSO that could cause unwanted differentiation before being transferred to the culture flask. To differentiate HL-60 cells into a neutrophil-like phenotype, the cell medium was supplemented with 1.3% DMSO, cell culture grade, with a fresh culture of cells at 1×10^5 cells/milliliter. Differentiation took approximately 6 days, and was accompanied by acidification of the culture medium (appearing yellow due to the phenol red indicator solution), cessation of cell proliferation and stabilization at approximately 5×10^5 cells per milliliter, and a slight decrease in cell size (from 15 to approximately 12 micron in diameter). Differentiated cells were confirmed to be differentiated by a smear-prep of the cultured cells on a glass slide, followed by flame fixation and staining in Wright-Giemsa's stain: neutrophil-like cells had a clear cytoplasm and a basic-staining bent or multi-lobular nucleus, similar to a band neutrophil.

Bovine aorta endothelial cells (BAEC) pooled from multiple donors were obtained commercially and maintained in a standard incubator, maintained at 37 degrees Celsius and with a 5% CO_2 atmosphere. Standard medium for culturing was Dulbecco's-modified Eagle's medium (DMEM), with 4.5g/L glucose, supplemented with 10% FBS and 100 U/mL each of penicillin and streptomycin. Cells were seeded at 2,500 cells/mL, in 10 cm petri dishes maintained between 30–90% confluency as monitored by microscopy, and

passaged when necessary by using 0.25% (w/v) trypsin in ethylenediamine tetraacetic acid (EDTA) balanced salt solution. Cells were used between passages 4–9: in order to have a ready supply of appropriately-aged cells, cells were cryopreserved using standard technique in the normal growth medium supplemented with 10% DMSO, cell culture grade, as a cryopreservant. Cryopreserved cells were awakened by standard technique.

6.3.4 QD degradation in the presence of antioxidants

6.3.4.1 Cell-free microplate assays of QD degradation

QDs were diluted in phosphate-buffered saline (PBS) in black 96-well microtiter plates so that the final concentration would be 1 nmol/L. Samples of biological oxidants were added so that the final concentration would be equivalent to the human reference values (where available) or values from the literature, as summarized in Table 4 on page 124. Lyophilized plasma, lyophilized catalase, and lyophilized serum albumin (Bt Plasma, Bt Catalase, and BSA) were obtained commercially and were of bovine origin; they were diluted into PBS before use. L-ascorbic acid, uric acid, L-cyseine and glutathione (GSH) were obtained commercially as powders and were diluted into PBS before use.

6.3.4.2 Stimulated degradation of quantum dots by live cells

Several days ahead of degradation experiments, BAEC cells were trypsinized and passaged into clear bottom black 96-well microtiter plates. The BAEC cells were allowed to form a confluent monolayer (monitored by light microscopy) before proceeding with experiments. Neutrophil-like HL-60 cells were placed in a separate clear bottom black 96-well microtiter plate for experiments at a final density of 1×10^5 cells/milliliter. In both cases, cells were either in physiologic balanced salt solutions (Hank's buffered saline solution, HBSS, with calcium and magnesium, Ca^{++}/Mg^{++}) or in respective standard culture medium (IMDM for HL-60, DMEM for BAEC) containing FBS but not phenol red indicator solution, as indicated. QDs were added so that the final QD concentration would be 1nmol/L. Cells were then stimulated with 100nmol/L phorbol 12-myristate 13-acetate (PMA) for HL-60

or 1 μg/mL lipopolysachharides (LPS) from *Escherichia coli* (E. coli) for BAEC. Inhibitors of MPO (1mmol/L sodium azide, NaN_3; or 100μmol/L 4-aminobenzoic acid hydrazide, ABAH) and scavengers of H_2O_2 (100 U/mL catalase, Cat, from bovine liver) were used to test inhibition of degradation. Cells were placed in the incubator for the indicated times (1 or 24 hours) before reading the plate on a fluorometric plate reader.

For microscopy, QDs were adsorbed onto glass coverslips, onto which neutrophil-like HL-60 cells were plated at low density (such that only 3–5 cells were observed in the field with a 40X objective). Cells were suspended in either HBSS or IMDM and FBS, as indicated. Cells were then stimulated with PMA and allowed to rest in the incubator 1 hour before imaging on the microscope. For initial microscopy images, cells were imaged under excitation light with a bandpass filter centered at 475 nm with 30 nm bandwidth and a 510 nm longpass filter. To photoanneal, the microscope field was exposed to UV excitation light centered at 358 nm with 55 nm bandwidth for 5 minutes with the sample in focus, then imaged with the same filter set as before.

6.3.4.3 Data analysis of live-cell microplate experiments

Microtiter plate (microplate) experiments for live cells all included a zero reference of water that was used to calibrate the fluorometric plate reader photodetector, and a baseline reference of cell medium only (either balanced salts or cell culture medium). The microplate experiments also included a full-signal reference of QDs in cell medium but without cells. In addition to the cell-free references, each microplate also had these references but with cells added. Each data point consisted of at least 4 samples (n = 4), and was considered acceptable if the coefficient of variation ($\%CV = 100 \times \frac{\bar{x}}{\sigma}$) was below 30%. The relative fluorescence remaining is the ratio of the mean fluorescence at each data point to the mean fluorescence of the full-signal reference, subtracting the mean fluorescence of the QD-free cell reference.

6.4 Results and discussion

6.4.1 QD degradation by biological oxidants is only by HOCl and H_2O_2

We tested the optical stability of QDs against a panel of ROS that can be found in phagocytes, with the assumption that a change in fluorescence emission would indicate that degradation could be occurring. The results are shown in Figure 47 on the next page Of all the ROS tested in this panel, only HOCl, H_2O_2, and ·OH showed significant decreases in fluorescence intensity. It should be noted that in this case, ·OH was generated by Fenton's reaction, which uses H_2O_2 as a component of the reaction. The fluorescence loss between the H_2O_2 and ·OH groups is the same, and so the fluorescence loss due to ·OH exposure is assigned to the presence of H_2O_2 in the reaction. ·OH also has an extremely short half life, on the order of nanoseconds, and so has a mean diffusion distance in pure water of about 1nm. The PAA-*g*-DDA polymer coating of the QDs has a thickness of 1nm (including the alkyl surfactants from QD synthesis) as measured by transmission electron microscopy (TEM), and the layer is thicker when in aqueous solvent and not on the TEM grid. Thus, it is unlikely that ·OH could diffuse across the thick QD polymer coating to react at the crystal surface of the QD without reacting with the polymer itself. Beyond diffusion distance considerations, the QDs used in these studies have a negative charge at physiologic pH which can repel charged species through Coloumb interactions. Of all the oxidants tested, only HOCl, H_2O_2, and ·NO are neutrally-charged at physiologic pH. ·NO binds to transition metals to form metal nitrosyls, but such an interaction should result in a change in the optical properties of the QD and no change is observed. $ONOO^-$, in addition to being charged at physiologic pH, has a short half-life in aqueous solution of 1.9 seconds and so is unlikely to reach the QD surface and participate in a QD surface reaction before reacting with something else.

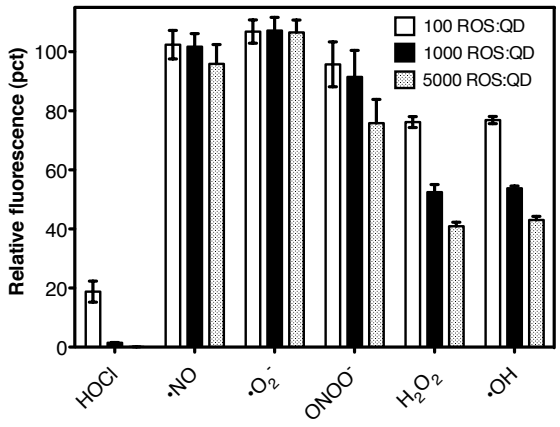

Figure 47: Quantum dot (QD) fluorescence loss following exposure to biological reactive oxygen species (ROS). The fluorescence of QDs in physiologic buffered pH solutions were exposed to the indicated biologic ROS and the fluorescence was then monitored. The molar ratio of ROS to QD is based on the initial amount of reagent added and is a approximate measure in many cases because of the short lifetimes of many ROS. Error bars show the 95% confidence interval, n = 4.

6.4.2 Degradation of QDs by the MPO enzyme system is similar to HOCl alone

Since the MPO enzyme system is known to produce many products, not just HOCl, we next tested the ability of the MPO enzyme system to cause QD fluorescence quenching. The canonical MPO-catalyzed reaction is the reduction of Cl^- in the presence of H_2O_2 to generate HOCl, but MPO actually can exist in three different forms (referred to as compounds I–III) and so the actual reaction may not be so straightforward.[131] As shown in Figure 48 on the following page, QDs lose significant amounts of fluorescence only when combined with MPO and the precursors of HOCl production (Cl^- and H_2O_2). The addition of 4-aminobenzoic acid hydrazide (ABAH), an MPO inhibitor, prevents a large percentage of the quenching from occurring.[129] MPO is a cationic protein, and the polymer-encapsulated QDs used for these experiments is anionic (as are many nanoparticles for *in vivo* use). It is possible that MPO is able to electrostatically bind to QDs, creating a "ball and chain" situation where the HOCl concentration is greatest proximal to the QD.

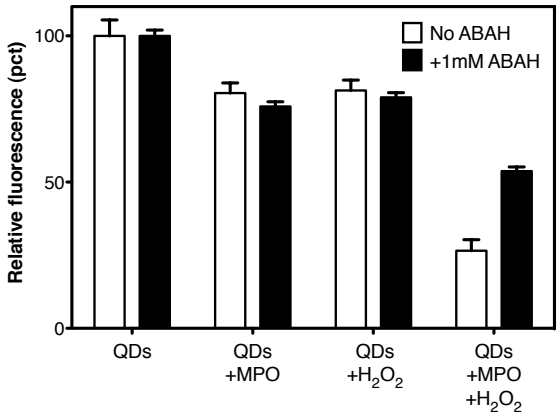

Figure 48: Quantum dot (QD) fluorescence loss occurs only in the presence of myeloperoxidase (MPO) and the precursors for generating hypochlorous acid (HOCl). The fluorescence of QDs diluted into phosphate-buffered saline (PBS) was monitored after the addition of MPO, H_2O_2, and the combination of the two. The effects of ABAH, an MPO inhibitor, was also measured. The required precursors for MPO to produce HOCl are Cl^- (supplied in the PBS) and H_2O_2; only this combination results in significant QD fluorescence quenching. Error bars show 95% confidence interval, n = 4.

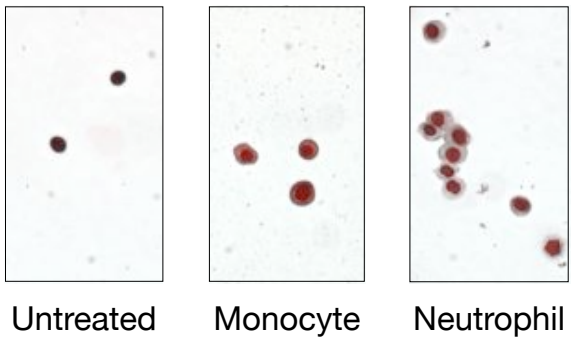

Figure 49: An example micrograph of differentiated HL-60 cells. HL-60 cells can differentiated in culture by exposure to all-*trans* retinoic acid (ATRA) to induce a monocyte-like phenotype or dimethylsulfoxide (DMSO) to induce a neutrophil-like phenotype. The undifferentiated and differentiated cells are shown with Wright-Giemsa staining.

6.4.3 Degradation of QDs by live cells

To see if live cells could degrade QDs by generating HOCl via MPO, we used the HL-60 cell line, a human line originally derived from a patient with acute promyelocytic leukemia.[44] The utility of the HL-60 cell line is that by co-culturing with specific small molecules, the cells can be terminally differentiated from a promyelocyte-like cell into other cell types, such as granulocyte-like or monocyte-like cells.[44, 245, 162] In the case of HL-60 cells co-cultured in 1.3% dimethylsulfoxide (DMSO), the cells adopt a neutrophil-like phenotype after approximately six days. Like neutrophils, the DMSO cultured HL-60 cells are smaller than the promelocyte progenitor, have a clear cytoplasm and banded or multilobular nucleus under Wright-Giemsa staining, and are positive for nitro blue tetrazolium (NBT) staining.[43] Differentiated HL-60 cells stained with Wright-Giemsa stain are shown in Figure 49 on the previous page. The neutrophil-like HL-60 cells will also phagocytize zymosan particles (yeast) and undergo oxidative burst, releasing HOCl by MPO catalysis. Alternatively, the cells can be exposed to phorbol 12-myristate 13-acetate (PMA), a PKC activator, to induce a potent oxidative burst without phagocytosis.[45] We used PMA to induce an oxidative burst in neutrophil-like HL-60 cells that were incubated with QDs. As shown in Figure 50 on the following page, QD fluorescence is lost when QDs are incubated with neutrophil-like HL-60 cells, and the fluorescence loss occurs in a PMA dose-dependent manner. Addition of sodium azide (NaN_3), an MPO inhibitor, largely prevents the fluorescence loss.

Going beyond population measurements of cells in a microplate as in Figure 50 on the next page, we adsorbed QDs onto the bottom of coverslips and performed microscopy of neutrophil-like HL-60 cells. As seen in Figure 51 on page 123, HL-60 cells stimulated with PMA quench the fluorescence of QDs that are directly underneath the cells (appearing as "holes" in the layer of adsorbed QDs on the glass coverslip). As in the microplate experiments, addition of NaN_3 prevents the quenching from happening. Imaging one of the "holes" with a UV excitation filter cube on the microscope reveals that the QDs underneath

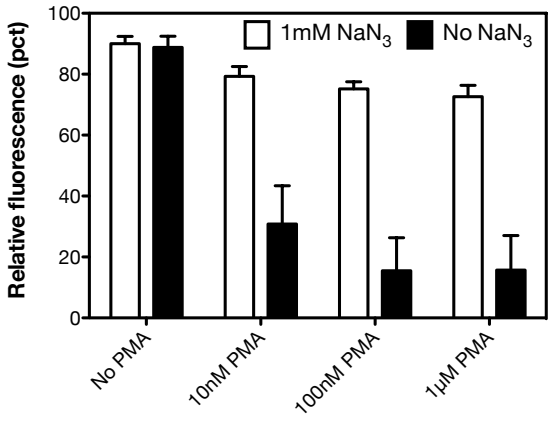

Figure 50: Quantum dot (QD) fluorescence loss occurs in the presence of cells stimulated to undergo an oxidative burst. The fluorescence of QDs incubated with HL-60 cells differentiated into a neutrophil-like phenotype was monitored after the addition of PMA, a small molecule that stimulates neutrophils to undergo an oxidative burst and subsequently produce HOCl. The addition of sodium azide (NaN_3) to inhibit HOCl production largely prevents the fluorescence loss. Error bars show 95% confidence interval, n = 4. Adapted with permission from ref. [148]. Copyright 2008 American Chemical Society.

and near the stimulated HL-60 cells will photoanneal, and that the photoannealed QDs are multicolored. That the QDs have blue-shifted in fluorescence emission is indicative of a size decrease, *i.e.,* etching and degradation.

6.4.4 Degradation of QDs in the presence of endogenous antioxidants

Based on the cell culture results, it would be expected that QDs would rapidly degrade if injected *in vivo*, however, this is not observed. In fact, Bruchez and coworkers noted that QDs could still be observed in mice that were injected two years prior, and that these QDs exhibited hypsochromic spectral shifts from the original fluorescence peak—photoannealing was not considered.[77] The difference between the cell culture experiments presented so far and the *in vivo* experiments performed by others can be explained as a difference in context: in the experiments presented in previous subsections, the solutions were very "clean", using pure reagents and cells in balanced salt solutions devoid of serum or other additives. In the *in vivo* milieu, there are many things present other than the cells and QDs.

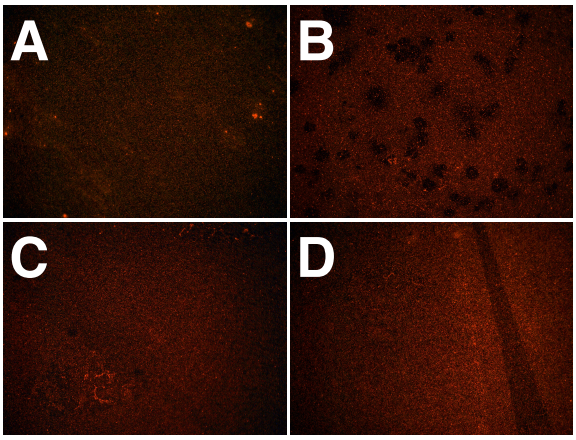

Figure 51: Live cells cause quantum dot (QD) fluorescence quenching after a stimulated oxidative burst. QDs were adsorbed onto the surface of glass coverslips, onto which neutrophil-like HL-60 cells were then placed. (A) Unstimulated cells on the field of QDs cause no fluorescence quenching. (B) After stimulation to release hypochlorous acid (HOCl), the cells quenched the fluorescence of QDs underneath and near the cells, resulting in a "Swiss cheese" pattern in the adsorbed QD layer. Addition of an inhibitor of the enzyme which produces HOCl prevented the fluorescence loss both without (C) and under (D) stimulation to produce HOCl. Images were contrast-enhanced with the same settings used across images.

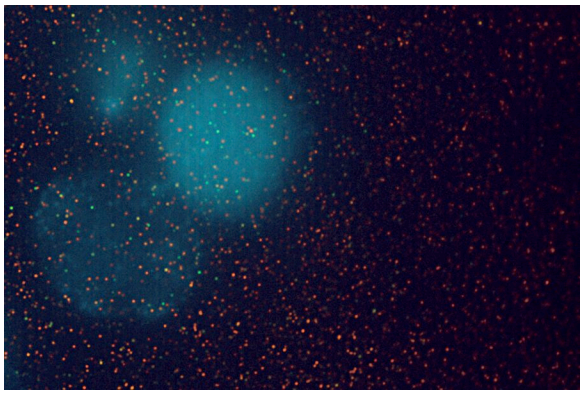

Figure 52: Quantum dots near live cells can be photoannealed after fluorescence quenching. QDs were adsorbed onto the surface of glass coverslips underneath neutrophil-like HL-60 cells. After stimulation with to release HOCl, the cells quenched the fluorescence of QDs directly underneath the cells. The microscope field was then photoannealed by short time exposure to UV light. QDs that were previously not visible became visible but with a shifted emission wavelength consistent with degradation. The cells themselves appear as a blue haze. Image was digitally-adjusted for color balance.

Table 4: A partial listing of antioxidants found in the bloodstream

Antioxidant	Type	Reference value	Literature reference
Serum albumin	Protein	32–45 g/L	[157]
Glutathione	Small molecule/thiol	24–37 mg/dL	[157]
Cysteine	Small molecule/thiol	9.2μmol/L	[115]
Ascorbic acid	Small molecule/vitamin	0.6–1.6 mg/dL	[157]
Uric acid	Small molecule	3.6–8.3 mg/dL	[157]
Catalase	Enzyme	94.8–127.8 MU/L	[257]

Since ROS are highly reactive, these other entities are possible targets for reaction simply by being present. These secondary products can themselves be useful as antimicrobial agents (chloramines), or can be deleterious as in the case of oxidized low-density lipoprotein (oxLDL) cholesterol.[247, 248, 50] Additionally, there are many antioxidants present designed to specifically react with ROS to protect the organism from oxidative damage. Summarized in Table 4 on the current page is an abbreviated listing of the antioxidants found in the blood. We will consider the effects of serum albumin, a protein which maintains serum osmotic pressure and can act as an antioxidant;[208] glutathione and cysteine are both small-molecule thiols, both of which are general antioxidants;[168, 264] ascorbic acid (vitamin C) is a hydrophilic vitamin ubiquitous in the body and a participant in many biological redox cycles;[264] uric acid is a major antioxidant in the blood;[207] and catalase is an enzyme carried by erythrocytes.[3]

Given the high reactivity of HOCl, it would be predicted that the ability of HOCl to cause QD fluorescence decreases in the presence of any other species in solution would be greatly reduced; conversely, because H_2O_2 has a lower kinetic rate of reaction with many species, it would be expected to be less influenced by the presence of other species in solution. As shown in Figure 53 on page 126, the full story is more nuanced. For HOCl, any antioxidant specie in solution protects QDs against fluorescence quenching; this is a reflection on the promiscuous reactivity of HOCl. Ultimately, enough HOCl is able to overcome

antioxidant protection and begin reacting with the QDs. Uric acid offers no protection, thiols have minimal protective effects, and BSA and ascorbate have moderate protective effects against H_2O_2 attack of the QDs. Both plasma and catalase are sufficient to fully protect the QDs against H_2O_2 attack. These data show that while QD degradation in the presence of biological antioxidants is greatly reduced, it is still relevant. That HOCl showed degradation even in reconstituted plasma, albeit at super-pathophysiologic concentrations, suggests that degradation could still occur in *in vivo* with antioxidants present.

Revisiting cell culture experiments, conducting the experiments in normal cell culture medium (containing 10% bovine serum by volume) alters the dynamics of fluorescence loss in QDs after stimulation of primary endothelial cells and neutrophil-like HL-60 cells to produce ROS, as shown in Figure 54 on page 127. The endothelial cells are expected to generate H_2O_2 in majority following stimulation; the HL-60 cells will produce both H_2O_2 and HOCl following stimulation. Since there is no fluorescence loss in the endothelial cell experiments for any condition, it is likely that the endothelial cells are not able to produce enough H_2O_2 under these experimental conditions to cause a noticeable loss in QD fluorescence. In the case of the neutrophil-like HL-60 cells, the addition of serum is sufficient to completely protect the QDs under all condtions.

Revisiting the HL-60 microscopy studies using cell culture medium containing serum shows that QDs directly underneath cells still are quenched. A difference when compared to cells in balanced salts is that far from the cells, QD fluorescence is not quenched in the case of experiments carried out with serum present, whereas QD fluorescence is quenched in the case of experiments carried out in buffered saline solution. This shows that QD fluorescence quenching can still occur, even in the presence of antioxidants, however the scope of the fluorescence quenching (and subsequent degradation) is much more limited. Photoannealing the quenched QDs underneath the cells shows restoration of QD fluorescence only on the cell periphery, where the QDs now fluoresce green. That the QDs fluoresce green is a sign of severe degradation (based on the QD composition, Table 2 on page 94),

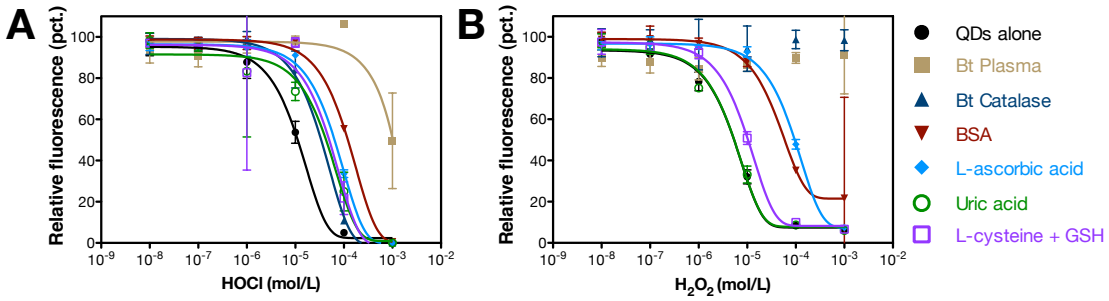

Figure 53: Quantum dot (QD) degradation by reactive oxygen species (ROS) is retarded in the presence of biological antioxidants. QDs were diluted into physiologic pH buffered solutions containing biological antioxidants in concentrations matched to *in vivo* human concentrations, and then exposed to indicated concentrations of either HOCl or H_2O_2. In all cases, the presence of antioxidants retarded the quenching of QD fluorescence. Lines of fit are a decaying exponential intended as a visual guide, error bars show the 95% confidence interval, n = 4.

and so it is likely that the QDs directly underneath the cells (which remain dark) have been oxidized beyond the point of fluorescence restoration. Note that this case of QD degradation still occurred in presence of serum.

6.5 Conclusions

In this chapter, we have shown that the HOCl degradation process described in Chapter 5 can occur via cell mediated processes. Enzyme-only systems show the same "dramatic" rapid and severe fluorescence quenching observed in the pure chemical experiments, and cellular experiments with model phagocytes show that fluorescence quenching and degradation occur. Taking the biological milieu into account, with numerous other species and antioxidants present, we find that QD fluorescence quenching and degradation still occur but the scope becomes much more limited—instead of QDs in the local area being quenched, only QDs directly in contact with cells become quenched. Some of these cellular results have been replicated in part by Yan *et al.*.[273] The data show that QDs cannot be assumed to be in a fluorescent state *in vivo*, and so pharmacokinetics and biodistribution studies of QDs relying on fluorescence alone require additional scrutiny and care to

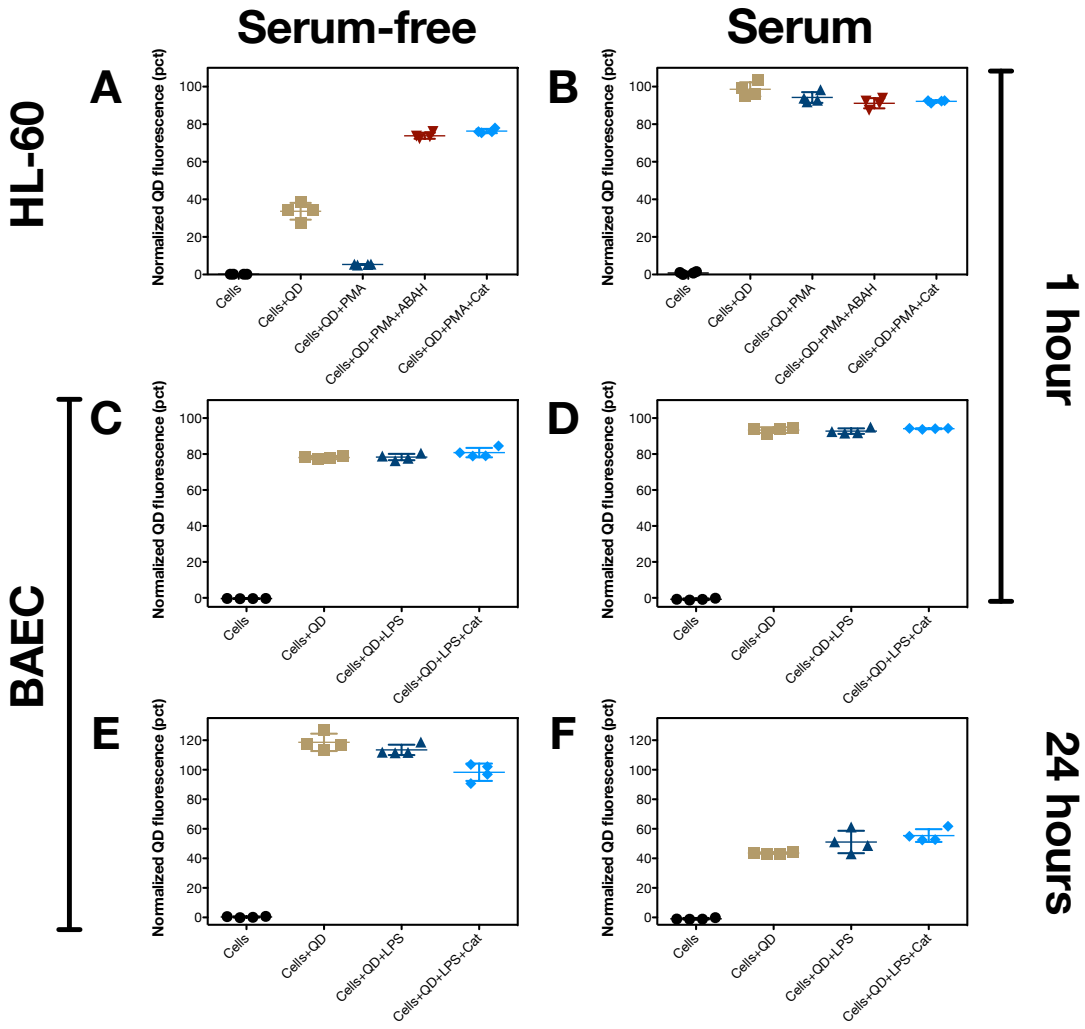

Figure 54: Quantum dot (QD) degradation by stimulated cells in a cell culture model is retarded by the presence of serum. QDs were added to cell cultures of neutrophil-like HL-60 cells (A, B) or bovine aorta endothelial cells (BAEC, C–F) in a presence of balanced salts, serum-free (A, C, E) or normal culture medium with serum (B, D, F). Cells were then treated with phorbol 12-myristate 13-acetate (PMA) or lipopolysaccharides (LPS), ROS production stimulants for HL-60 and BAEC cells, respectively. Where indicated, catalase (Cat) or 4-aminobenzoic acid hydrazide (ABAH) were used as inhibitors of HOCl or H_2O_2 production, respectively. BAECs were measured at 1 and 24 hours because they are known to produce H_2O_2, which was shown earlier in cell-free systems to take more time than HOCl to cause QD fluorescence quenching.

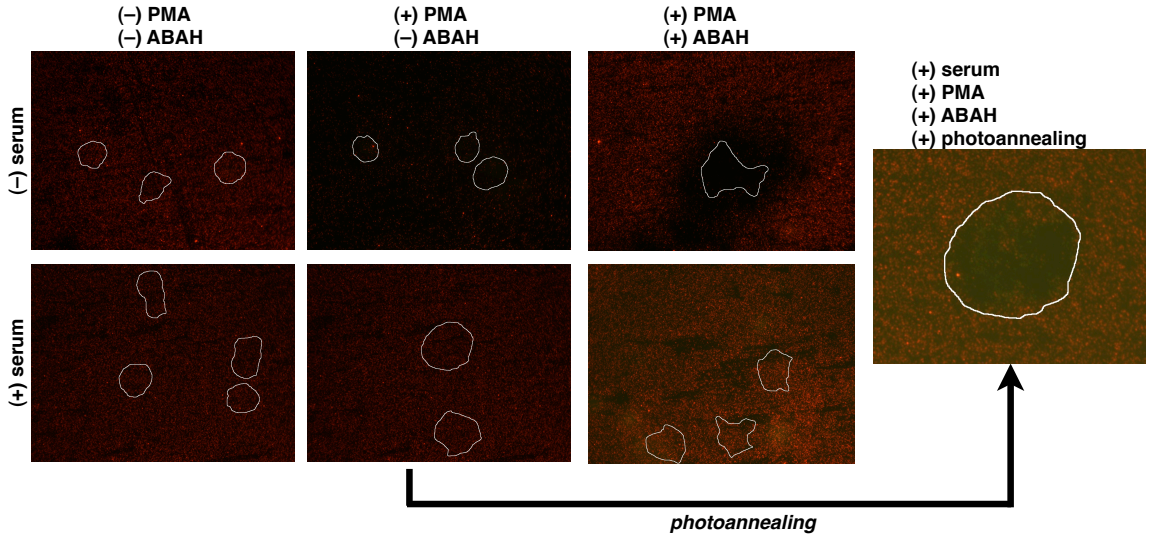

Figure 55: Quantum dot (QD) degradation by stimulated neutrophil-like (HL-60) cells occurs with serum present, but is limited in scope. QDs were adsorbed to glass coverslips, to which cells in either balanced salts (no serum) or culture medium (serum present) were added. When stimulated, cells in the serum-free sample reduced QD intensity across the microscope field when compared with the untreated cells; the addition of inhibitors of HOCl production reduced the scope of degradation to the area nearest the cells. The presence of serum greatly abated the degradation effect. Photoannealing the cells by short-term exposure to UV light showed that the QDs on the cell periphery with quenched fluorescence had a blue-shifted band-edge fluorescence emission (into the green range), consistent with a size decrease and degradation. White outlines show the borders of activated cells. Images were acquired with identical camera and filter settings, and are unaltered with the exception of the drawing of the outline.

account for possible oxidative degradation. For example, Chou *et al.* proposed using silver enhancement staining to find QDs that could be in a non-emitting state in histological preparations.[41] In sum, the results predict that QD degradation can occur *in vivo* by reaction with HOCl, however the degradation will not be the rapid degradation observed in the pure chemical experiments and will most likely require pathophysiologic conditions to occur, such as happens in cases of sepsis or organ failure.

CHAPTER VII

NEXT STEPS IN SURGICAL GUIDANCE AND NANOTECHNOLOGY

7.1 Abstract

Here, we summarize the work presented in this dissertation and the contributions made to the fields of cancer surgery and nanoparticle toxicity. We then consider the logical continuations of this research towards other problems in medicine.

7.2 Summary

This dissertation has been concerned with cancer. Cancer is a complex disease with a tremendous societal impact in the United States. Beyond the U.S., cancer will become a global problem as the developing world both grows older and adopts a Western lifestyle. In Chapter 1, we reviewed the impact of cancer on the U.S. in terms of morbidity, mortality, and the economic impact. We then briefly reviewed the characteristics of cancer as a disease, and why diagnosing and treating cancer is a challenge.

Next, we reviewed in Chapter 2 how nanotechnology has use in cancer imaging since much about cancer imaging is in the design and development of contrast agents. We looked through the "near-infrared window" and saw why it is a useful region of light for biomedical imaging. As such, we then reviewed two classes of nanoparticles that are popular as imaging research tools and have the potential for human translation: semiconductor quantum dots (QDs) and colloidal gold. As this dissertation is in part concerned with the degradation of semiconductor quantum dots, we concentrated on the synthesis and characterization of quantum dots and delved into the inner workings of quantum dots. We also explored how quantum dots are made water soluble, a necessary step for biological applications. We

then looked at colloidal gold nanoparticles, which beyond their own interesting properties, can be made into a tool for Raman spectroscopy (SERS).

In Chapter 3, we describe the development of an intraoperative imaging platform technology. This platform consists of contrast agents, a local excitation and spectroscopy device, and a widefield imaging system. The system is designed for intraoperative guidance, using the fluorescent compounds (such as QDs) or Raman-scattering compounds (such as SERS nanoparticles) described in Chapter 2 for contrast. We characterize an implementation of this platform technology, before using it in Chapter 4. We began by testing the instrumentation in murine models of cancer, and show that the system is capable of detecting the difference in contrast accumulation between normal and neoplasia. The technology is then applied to a cancer more similar to human cancer by imaging cancer in spontaneous canine tumors. We show that the results of imaging murine tumor models are similar to imaging of spontaneous canine tumors. We show that a systemically injected and FDA-approved contrast agent (in an off-label use) accumulates within spontaneous tumors and can be readily detected by the proof-of-concept instrumentation described in Chapter 3—a necessary step in translating this technology and related methods into the clinic.

Next, in Chapter 5 we explore the degradation of QDs through exposure to hypochlorous acid (HOCl), a common household chemical that also has importance in biology. We show that degradation of QDs by HOCl exposure is a rapid process that both quenches QD fluorescence as well as dissolves the QD crystal itself. We also show that QD fluorescence can in some cases be restored through a process known as photochemical annealing, and that through QD fluorescence changes, we can discover the amount of damage done to the QD by HOCl. We then explore the biological implications of the QD/HOCl process in Chapter 6. We learn that HOCl is a biological oxidant associated with the immune response, and that nanoparticles themselves tend to induce an immune response. Through *in vitro* testing, we show that live cells in a model system can cause degradation of QDs, but

that the degradation rate under expected biological conditions will be slow. Nanoparticle-associated toxicity is a great concern, both because of environmental exposures and through the growing use of nanoparticles in consumer goods and in medicine. These results bring a better understanding to the ultimate fate of QDs in the biological environment.

7.3 Future directions

This dissertation has been focused on two areas of development, one in biomedical instrumentation, and one in contrast agent stability *in vivo*. The instrumentation developed has clear translational potential into the clinic, and the spontaneous canine cancer experiments are a first step in this direction. The technology also has applications in other areas of human medicine. Beyond the implications for toxicology, the degradation of QDs by HOCl may have use for diagnostic applications.

7.3.1 Refinement of instrumentation

As proof-of-concept devices, naturally, there are numerous improvements and advancements that can be made to the intraoperative instrumentation that we have presented. Many of these are refinements, such as improvements to the optical layout to compact the system size, increases to the camera resolution for "HD" imaging, streamlining the physical packaging of the system, and better integration of the devices through software. Some necessary improvements will only become apparent once usability studies are performed in the operating room. As part of these usability studies, we would also be developing standardized protocols for use in the operating room. The increased use of minimally-invasive procedures demands that the system be adapted to laproscopic tools. Primarily, the adaptation consists of size minimization of the SpectroPen and coupling the widefield imaging system to a fiberscope. Beyond instrumentation, there is also potential to improve the contrast agents used with the system. ICG is useful as a contrast agent because of its favorable regulatory status and long history of safe use for fluorescence imaging. The optical properties of ICG are far from ideal, and newer contrast agents with better optical properties would

enhance the intraoperative instrumentation. Improved fluorescent dyes and semiconductor quantum dots are one class of candidates (although dyes have a more likely approval possibility). Activatable contrast agents that turn on only in a tumor would be useful for increasing the contrast ratio (CR) of the agent (as discussed in this dissertation, a CR of 5 would be considered outstanding). Higher CR probes would make micrometastases easier to detect *in vivo*. There is also a new contrast agent, 5-aminolevulinic acid (5-ALA), seeking U.S. regulatory approval after having already received European approval. This agent operates within the visual light range and has been applied to intraoperative imaging in brain cancer. Making the instrumentation compatible with this agent is a matter of adjusting the optical setup, mostly in the excitation laser and widefield optical filters. We also present data using SERS nanoparticles, and show how they have improved depth of penetration in tissue and explain how they can be used for facile multiplexing. Because Raman scatter operates through a virtual energy state, it can be induced by light of any wavelength. Developing instrumentation operating at 1064 nm offers the possibility of imaging with even lower endogenous background, with a tradeoff of greater cost in instrumentation. The SERS particles we have used are also gold colloid based, and have a favorable regulatory approval outlook. Finally, while spectroscopy is powerful it does increase the overall system cost. Local excitation paired with widefield imaging is in itself useful and would be loess costly than a system that also includes spectroscopy. Such a lower-cost system could be important for rural clinics and developing world users.

7.3.2 New applications of instrumentation in cancer surgery, pathology, and cardiovascular medicine

We show the application of the intraoperative instrumentation in several cancer types. The technology itself can be applied to many areas of medicine, so long as there is a suitable contrast agent. Through ourselves and collaborators, the technology has been applied to murine models of lung metastases, head and neck cancer, pancreatic cancer, colon cancer, and brain cancer. We have not yet explored the utility of this technology for cancer

screening. Being based on optics avoids the ionizing radiation concerns inherent to x-ray, x-ray computerized tomography, and nuclear medicine modalities (other than magnetic resonance, MR). Optical technologies also have a cost advantage over MR imaging.

This technology could also find a home in a pathology laboratory. A 1 cm^3 tumor, to sample completely by histology with 5 micron slices, would require 2,000 slices. Multiply this by a number of patients and it's clear that pathologists can only afford to sample a limited number of areas on a specimen. The correct pathologic determination then relies on the skill and experience of a pathologist to sample the correct areas of a specimen. The intraoperative imaging technology, with software customized for pathology, could be used as an integrated workflow alongside the surgical system. Using one contrast agent, the surgeon would resect tissues showing contrast accumulation, the pathologist could then use the same contrast agent accumulation to know what areas of the tissue warranted scrutiny.

Beyond cancer, this technology could also be useful for cardiovascular medicine. Atherosclerotic plaques, like tumors, have a "leaky vasculature" that could allow contrast agents like ICG to pool within. To be useful, the imaging instrumentation would need a catheter adaptation; to truly be useful, contrast agents specific for vulnerable plaques, perhaps through an activatable contrast agent scheme.

7.3.3 Using QD fluorescence quenching for functional assays

The unusual nature of the fluorescence restoration, through photoannealing, of QDs reacted with HOCl could be useful in biological assays. Myeloperoxidase (MPO), the enzyme that generates HOCl *in vivo*, is recognized as having a role in heart disease; some groups have also reported that serum MPO has value as a marker of ischemia (although this last point is actively debated).[267, 181] A simple microtiter plate assay could be developed with QDs as a functional reporter of MPO activity. Near-infrared (NIR) QDs could be mixed with whole blood, and the entire sample could be reacted with hydrogen peroxide (H_2O_2). The fluorescence quenching (if any) that resulted would be a function of the amount of MPO

present, its activity, and the amount of antioxidants present in the blood. Using photoannealing to restore the QD fluorescence could also be a useful step of the assay. Such a functional assay may give a more realistic assessment of the impact of MPO on an individual patient. MPO is also reported as present in atheromas, so QDs combined with photoannealing might make a useful *in vivo* contrast agent.[50] Outside of cardiology, QDs could be used for assays of total antioxidant capacity, common in food science.[28, 27, 112, 268] A challenge in these assays is the strong visual absorbance and autofluorescence of food compounds, which interferes with fluorescent sensors. Using NIR QDs could ameliorate this problem.

Using QDs for single particle HOCl measurements is an attractive idea, but the wide population distribution of colloidal QDs makes this quite challenging to implement. It might be more useful for epitaxially-grown QDs where there is better control of the final structure, in which case it could be useful both for sensing applications and for fluorescence emission control. A very specialized application of QD fluorescence quenching in the presence of HOCl could be in super resolution microscopy.[73] Many of these techniques require the modulation of the fluorescing state of the fluorophore to work. QDs naturally have an intermittent fluorescing state, on the order of milliseconds. Some have used this stochastic blinking property for super resolution microscopy.[111, 139] Quenching of QD fluorescence through HOCl exposure followed by stochastic recovery of the fluorescence through photoannealing would work similar to stochastic optical reconstruction microscopy (STORM).

7.3.4 Designing "safe" QDs for *in vivo* imaging

Knowing the causes of rapid QD degradation *in vivo* makes designing degradation-resistant QDs a possibility. We showed that the common surface coatings of QDs are unable to prevent degradation by HOCl, and we showed that biological oxidants were able to resist

HOCl attack. A QD surface coating incorporating strong antioxidants, such as a water-soluble vitamin E derivative, could greatly protect the QDs from HOCl attack. Combining an "armored" QD surface coating with a size-minimized QD (below 5–6 nm hydrodynamic radius for renal clearance) could result in a probe that would be eliminated from the body before degradation could occur. Animal model testing, using models of sepsis or multiple organ failure, could be used to provide worst-case scenarios of reactive oxygen species (ROS) assault. If ROS-resistant QDs are known to reliably clear from the body and without degradation, the case for using QDs for human *in vivo* imaging becomes more analogous to that of gadolineum chelates. Regardless of applications for human imaging, ROS-resistant QDs would be desirable for general imaging for animal models.

7.4 Conclusions

In this dissertation, we have presented both a highly translatable platform technology for intraoperative guidance and fundamental studies of semiconductor quantum dot behavior. The intraoperative instrumentation has the potential to greatly improve solid-mass tumor therapy by ensuring effective surgical resection of the entire mass. By doing so, the patient can be freed from radiotherapy/chemotherapy follow up and from possible scar revision surgery. In this chapter, we have described how the technology can be brought into other applications and diseases in medicine, improving medical care beyond oncology. The fundamental studies on nanoparticle behavior that we have presented allow predictions to be made on the *in vivo* fate of some nanoparticles. We further show how the degradation process we have described could be useful for diagnostic assays in medicine and beyond.

APPENDIX A

INSTRUMENTATION, SOFTWARE, AND MATERIALS USED

Table 5: Vendors and sources of instrumentation, software, and materials used

Supplier or Vendor (Abbrev. name)	Location
Aaron Mohs (AMM)	Emory University, Atlanta, GA
Acros Organics, Inc. (Acros)	Geel, Belgium
Akron, Inc	Buffalo Grove, IL
Allied Vision Technology, Inc. (AVT)	Newburyport, MA
American Type Culture Collection (ATCC)	Manassas, VA
Andrew Smith (AMS)	Emory University, Atlanta, GA
BioTek	Winooski, VT
Brad Kairdolf (BAK)	Emory University, Atlanta, GA
Caliper LifeSciences (Caliper)	Hopkinton, MA
Carestream	Rochester, NY
CVI Melles-Griot (CVI)	Albuquerque, NM
DeltaNu Inc.	Laramie, WY
GraphPad, Inc.	La Jolla, CA
Hongwei Duan (HD)	Emory University, Atlanta, GA
Ika Works, Inc. (Ika)	Wilmington, NC
Image Quality Laboratory	Polytechnic University of Catalonia, Spain
InPhotonics, Inc.	Norwood, MA
Invitrogen Corp.	Carlsbad, CA
Lambda Research Corporation	Littleton, MA
Lily Yang, M.D., Ph.D (LY)	Emory University, Atlanta, GA
Lonza Walkersville, Inc. (Clonetics)	Walkersville, MD
Mallinckrodt Chemicals (Mallinckrodt)	Phillipsburg, NJ
Mediatech, Inc (Cellgro)	Manassas, VA
Microsoft Corporation	Redmond, WA
Midsci, Inc.	St. Louis, MO
Nalge-Nunc Int'l (Nunc)	Rochester, NY
National Institutes of Mental Health (NIMH)	Bethesda, MD
Olympus Life Sciences (Olympus)	Center Valley, PA
Pall Life Sciences (Pall)	Port Washington, NY
Photon Technology International, Inc. (PTI)	Birmingham, NJ
Rapp Polymere (Rapp)	Tübingen, Germany
Roper Scientific	Acton, MA

Table 5: (continued)

Supplier or Vendor (Abbrev. name)	Location
Schneider-Kreuznach (Schneider)	Hauppauge, NY
Shimadzu Scientific Instruments (Shimadzu)	Columbia, MD
Sigma-Aldrich Fine Chemicals (SAFC)	St. Louis, MO
Ted Pella, Inc	Redding, CA
Thorlabs, Inc.	Newton, NJ
UGA Animal and Dairy Sciences Department (UGA-ADSD)	Athens, GA
UVP, LLC	Upland, CA

Table 6: Instruments used

Instrument	Model	Vendor	Used in section(s)
Bioluminescence imaging station	Image Station In-Vivo FX	Carestream	4.3.3
Cell counter	Auto T4	Nexcelom Biosciences	6.3.3
Fluorometer	QuantaMaster	PTI	5.3.3.1, *et alibi*
Microplate reader	Synergy 2	BioTek	5.3.3.1, *et alibi*
Microscope	IX-71	Olympus	4.3.3, 6.3.4.2
Microscope spectrometer	SpectraPro 150	Roper Scientific	5.3.3.1
Raman spectrometer	Advantage 785	DeltaNu	3.3.2.2
UV-vis absorbance spectrometer	UV-2401PC	Shimadzu	5.3.3.1, *et alibi*

Table 7: Software packages used

Software package	Vendor	Used for	Used in section(s)
ActiveFirePackage	AVT	Application programming interface for widefield imaging software	3.3.3.1
ImageJ	NIMH	Image analysis	*et alibi*
OSLO	Lambda Research Corporation	Optical layout and optimization of widefield imaging system	3.3.3.1
Prism	GraphPad, Inc.	General data analysis and visualization	*et alibi*
Slanted Edge Modulation Transfer Function	Image Quality Laboratory	(ImageJ plugin) calculation of MTF	3.3.3.2
Visual C-sharp	Microsoft Corporation	Writing and designing widefield imaging system software	3.3.3.1

Table 8: Materials used, in order of first appearance

Material	Item	Part number	Supplier	Used in section(s)
ICG	Cardiogreen	I2633	SAFC	3.3.1, *et alibi*
PBS	Phosphate buffered saline, 10X concentrate	46-013-CM	Cellgro	3.3.1, *et alibi*
BSA	Bovine serum albumin, lyophilized	A3059	SAFC	3.3.1, *et alibi*
Gold colloid, 60nm	Citrate stabilized gold colloid, 60nm	15708-6	Ted Pella	3.3.1
DTTC	3,3'-Diethylthiatricarbocyanine iodide	381306	SAFC	3.3.1
PEG-SH, 5kD	Polyethylene glycol, methoxy and thiol terminated, 5000 Da	12 5000-40	Rapp	3.3.1
SpectroPen head		RamanProbe	InPhotonics	3.3.2.1
SpectroPen spectrometer		Advantage785	DeltaNu	3.3.2.1
Polystyrene Raman standard			DeltaNu	3.3.2.2
Porcine fat			UGA-ADSD	3.3.2.2
Black 96-well microplate	Fluorescence immunoassay 96-well microplate, black polystyrene	781608	Midsci	3.3.2.2, *et alibi*
Common objective lens	35mm f1.9 c-mount lens	Xenoplan 1.9/35	Schneider	3.3.3.1
100mm meniscus lens	Singlet lens, BK7	LE1234-B	Thorlabs	3.3.3.1
60mm plano-convex lens	Singlet lens, BK7	LA1134-B	Thorlabs	3.3.3.1
-50mm biconcave lens	Singlet lens, BK7	LD1464-B	Thorlabs	3.3.3.1
45mm achromatic doublet, NIR	Achromatic doublet	AC254-045-B	Thorlabs	3.3.3.1
45mm achromatic doublet, visible	Achromatic doublet	AC254-045-A	Thorlabs	3.3.3.1
Protected silver mirror		PF10-03-P01	Thorlabs	3.3.3.1
NIR/laser dichroic mirror	800nm cut-on short pass filter	SWP-45-Runp-850-Tunp-694-PW-1025-C	CVI	3.3.3.1

Table 8: (continued)

Material	Item	Part number	Supplier	Used in section(s)
Laser/visible dichroic mirror	700nm cut-on short pass filter	BDA-700-25.0M	CVI	3.3.3.1
NIR bandpass filter	820nm center wavelength, 10nm bandwidth	F10-820.0-4-25.0M	CVI	3.3.3.1
NIR laser notch filter	785 notch rejection, OD >6 rejection	XNF-785.0-25.0M	CVI	3.3.3.1
Laser neutral density filter	OD 2, absorptive	NE20-B	Thorlabs	3.3.3.1
Color camera	Guppy FireWire camera	F-038C	AVT	3.3.3.1
Laser/NIR cameras	Guppy FireWire camera	F-038B/NIR	AVT	3.3.3.1
4T1 bioluminescent cell line		4T1/luc	LY	4.3.1.1
Tribromoethanol	2,2,2-tribromoethyl alcohol	T48402	SAFC	4.3.1.1
Luciferin	XenoLight RediJect D-luciferin solution	760504	Caliper	4.3.1.1
ICG, pharmaceutical grade	IC-Green	NDC 17478-701-25	Akron	4.3.1.2
Tissue homogenizer	Ultra-Turrax Tube Drive	3645001	Ika	4.3.2.1
CdSe/CdS/ZnS QDs, polymer-encapsulated	AMS and BAK	5.3.1, *et alibi*		
HOCl	Sodium hypochlorite, reagent grade, 10-13% active chlorine	425044	SAFC	5.3.2, *et alibi*
Chelex resin	Chelex resin, sodium form, 50-100 mesh	C7901	SAFC	5.3.2
H2O2	Hydrogen peroxide, 30% (w/v), with inhibitor, ACS grade	216763	SAFC	5.3.2, *et alibi*
Potassium iodide	Potassium iodide, ACS grade	60400	SAFC	5.3.2
Sodium thiosulfate	For titration, 0.1mol/L	35245	SAFC	5.3.2
Sodium hydroxide	Sodium hydroxide, ACS grade, pellet	221465	SAFC	5.3.2
Sodium phosphate, monobasic	Sodium phosphate, monobasic, monohydrate, ACS grade	S9638	SAFC	5.3.2

Table 8: (continued)

Material	Item	Part number	Supplier	Used in section(s)
Sodium phosphate, dibasic	Sodium phosphate, dibasic, heptahydrate, ACS grade	S9390	SAFC	5.3.2
UV light stand		XX15-M	UVP	5.3.3.1
10k MWCO ultrafiltration membrane	Nanosep	OD010C33	Pall	5.3.3.2
PEI-g-PEG QDs			HD	5.3.3.4
MPA QDs			BAK	5.3.3.4
Lipid/PEG QDs			AMM	5.3.3.4
Angeli's salt	Sodium ëś-oxyhyponitrite	82230	Cayman	6.3.1
Potassium superoxide		AC355420250	Acros	6.3.1
Sodium nitrite	ACS grade	517062	SAFC	6.3.1
Ferrous sulfate	Ammonium iron(II) sulfate hexahydrate	AC210370250	Acros	6.3.1
MPO	Myeloperoxidase, from human leukocytes, lyophilized	M6908	SAFC	6.3.2
ABAH	4-aminobenzoic acid hydrazide	A41909	SAFC	6.3.2, 6.3.4.2
HL-60		CCL-240	ATCC	6.3.3
IMDM	Isocove's modified Dulbecco's modified Eagle's medium	30-2005	ATCC	6.3.3
FBS	Fetal bovine serum, pooled donors	30-2020	ATCC	6.3.3
HL-60 tissue culture flasks	10cm^2 tissue culture flask	TP91253	Midsci	6.3.3
HBSS	Hank's buffered saline solution, without phenol red	21-023-CV	Cellgro	6.3.3, 6.3.4.2
Wright-Giemsa stain		WG128	SAFC	6.3.3
DMSO	Dimethylsulfoxide, cell-culture grade	4-X	ATCC	6.3.3
BAEC	Bovine aortic endothelial cell, pooled donors	BW-6002	Lonza	6.3.3

Table 8: (continued)

Material	Item	Part number	Supplier	Used in section(s)
BAEC tissue culture dishes	10cm diameter petri dishes, polystyrene, treated	TP93100	Midsci	6.3.3
DMEM	Dulbecco's modified Eagle's medium, 4.5g/L glucose	30-2002	ATCC	6.3.3
Pen/Strep	10kU/mL penicillin, 10g/mL streptomycin	30-2300	ATCC	6.3.3
Trypsin	0.25% trypsin in 0.53mmol/L EDTA	30-2101	ATCC	6.3.3
PBS	Phosphate buffered saline, no calcium or magnesium	21-040-CV	Cellgro	6.3.3, 6.3.4.2
Bovine plasma	Lyophilized bovine plasma	P4639	SAFC	6.3.4.1
Bovine catalase	Catalase, from bovine liver	C1345	SAFC	6.3.4.1
L-ascorbic acid		255564	SAFC	6.3.4.1
Uric acid		U2625	SAFC	6.3.4.1
L-cysteine		168149	SAFC	6.3.4.1
Glutathione, reduced		G4251	SAFC	6.3.4.1
Cell culture 96-well microplate	Fluorescence immunoassay 96-well microplate, black polystyrene, clear polystyrene bottom, tissue culture treated	165305	Nunc	6.3.4.2
IMDM without phenol red	Isocove's modified Dulbecco's modified Eagle's medium, no phenol red	21056-023	Invitrogen	6.3.4.2
DMEM without phenol red	Dulbecco's modified Eagle's medium, 4.5g/L glucose, no phenol red	21063-029	Invitrogen	6.3.4.2
PMA	Phorbol 12-myristate 13-acetate	79346	SAFC	6.3.4.2
LPS	Lipopolysaccharides from *Escherichia coli* 026:B6	L8274	SAFC	6.3.4.2
NaN_3	Sodium azide	1953	Mallinckrodt	6.3.4.2

Table 8: (continued)

Material	Item	Part number	Supplier	Used in section(s)
Coverslip slides for cell microscopy	LabTek-II, 8-well	155409	Nunc	6.3.4.2

APPENDIX B

OPTICAL LAYOUT SPECIFICATIONS

B.1 Lens layout for widefield imaging head

The widefield imaging head has three video channels, as configured. All three channels share the same main objective lens, field lens group, and collimating lens. The channels differ in the final focusing lens used to form the image on the camera sensors. The anatomic or color camera uses one layout; the laser and near-infrared (NIR) probe channels use a second layout. Both layouts are described *infra*. More information on the parts used appears in Appendix A, specifically Table 8 on page 140.

Table 9: Optical layout, visible light path

Surface	Radius (mm)	Thickness (mm)	Aperture radius (mm)	Glass	Part (Source)
Object	–	609.00	50.00	AIR	
Common objective	–	–	7.50	*	Xenoplan lens (Schneider)
2	–	19.00	1.81	AIR	
3	30.90	4.70	11.43	BK7	LA1134 (Thorlabs)
4	–		11.43	AIR	
5	32.10	3.60	11.43	BK7	LE1234 (Thorlabs)
6	82.20		11.43	AIR	
7	–	6.55	2.31	AIR	
8	-52.00	3.00	11.43	N-BK7	LC1715 (Thorlabs)
9	52.00	–	11.43	AIR	
10	–	31.00	2.28	AIR	
11	127.06	1.60	11.43	SFL6	AC254-045-B (Thorlabs)
12	25.05	7.00	11.43	LAKN22	
13	-29.38	–	11.43	AIR	
14	–	127.00	7.78	AIR	
15	31.24	7.00	11.43	BAFN10	AC254-045-A (Thorlabs)
16	-25.94	2.00	11.43	SFL6	
17	-130.62	–	11.43	AIR	
18	–	46.79	4.60	AIR	
Image	–	–	1.81	*	F-038C camera (AVT)

Table 10: Optical layout, NIR light paths

Surface	Radius (mm)	Thickness (mm)	Aperture radius (mm)	Glass	Part (Source)
Object	–	609.00	50.00	AIR	
Common objective	–	–	7.50	*	Xenoplan lens (Schneider)
2	–	19.00	1.81	AIR	
3	30.90	4.70	11.43	BK7	LA1134 (Thorlabs)
4	–		11.43	AIR	
5	32.10	3.60	11.43	BK7	LE1234 (Thorlabs)
6	82.20		11.43	AIR	
7	–	6.55	2.31	AIR	
8	-52.00	3.00	11.43	N-BK7	LC1715 (Thorlabs)
9	52.00	–	11.43	AIR	
10	–	31.00	2.28	AIR	
11	127.06	1.60	11.43	SFL6	AC254-045-B (Thorlabs)
12	25.05	7.00	11.43	LAKN22	
13	-29.38	–	11.43	AIR	
14	–	127.00	7.78	AIR	
15	29.38	7.00	11.43	BAFN10	AC254-045-A (Thorlabs)
16	-25.05	1.60	11.43	SFL6	
17	-127.06	–	11.43	AIR	
18	–	46.79	4.60	AIR	
Image	–	–	1.81	*	F-038B/NIR camera (AVT)

APPENDIX C

PSEUDOCODE FOR SOFTWARE DEVELOPED

C.1 Widefield imaging system software

The widefield imaging system software was implemented in C-sharp using a application programming interface provided by the camera vendor to handle the camera input/output and display routines. Each camera captures video on an independent processing thread and processes the video on the same independent thread. The composite video display, which is the main video window the user interacts with, is handled in the color video thread. The main event loop allows the user to alter the software settings as needed.

C.1.1 Main event loop

```
initialize cameras
initialize user interface
set software options to good default values

begin video capture:
  thread nir video capture
  thread laser video capture
  thread color video capture

thread main event loop:
  display composite video
  do user ui interaction:
    set metadata:
      user name
      lab name
      experiment name
      experiment date
      subject information
      contrast agent information
    set camera options:
      gain
      color balance
    set display options:
```

```
      overlay threshold nir
      overlay threshold laser
      overlay nir
      overlay threshold
      virtual phosphorescence display mode
      virtual phosphorescence decay time
    do store single composite video frame
    do store composite video frames
```

C.1.2 Laser video channel thread

```
thread laser video capture:
  get one video frame
  do apply laser threshold:
    find all points in frame above threshold (area)
    calculate centroid of threshold area
    calculate circle radius with area equal to threshold area
  do calculate circle with centroid, area:
    store center, radius
```

C.1.3 NIR video channel thread

```
thread nir video capture:
  get one nir video frame
  do apply nir threshold:
    find all points in frame above threshold (nir mask)
    store nir mask frame
  do if apply nir virtual phosphorescence:
    do function virtual phosphorescence:
      get vp mask frame
```

C.1.4 Color and composite video channel thread

```
thread color video capture:
  get one color frame
  do apply laser overlay (if set):
   (from thread laser video capture):
  get center, radius
    draw circle with center, radius with false color red
  do apply nir overlay (if set):
```

```
    (from thread nir video capture):
      get nir mask frame
    draw nir mask with false color cyan
  do apply nir virtual phosphorescence (if set):
    (from thread nir video capture):
      get vp mask frame
    draw vp mask with false color cyan
  store composite video frame
```

C.1.5 Virtual phosphorescence display function

```
function virtual phosphorescence:
  do calculate decay constant:
    decay_const = -log(1/max_nir_camera_intensity)/decay_time
  do apply decay to accumulation buffer:
    new_buffer = old_buffer*exp(-decay_const*framerate)
  (from thread nir video capture):
    do add nir mask frame to new_buffer
  store new_buffer as vp mask frame
```

REFERENCES

[1] Abraham, S. C., Fox, K., Fraker, D., Solin, L., and Reynolds, C., "Sampling of grossly benign breast reexcisions: a multidisciplinary approach to assessing adequacy," *Am J Surg Pathol*, vol. 23, pp. 316–322, Mar 1999.

[2] Adam, L., Fabian, I., Suzuki, K., and Gordon, G., "Hypochlorous acid decomposition in the pH 5-8 region," *Inorg Chem*, vol. 31, pp. 3534–3541, Jan 1992.

[3] Agar, N. S., Sadrzadeh, S. M., Hallaway, P. E., and Eaton, J. W., "Erythrocyte catalase. a somatic oxidant defense?," *J Clin Invest*, vol. 77, pp. 319–321, Jan 1986.

[4] Al-Jamal, W. T., Al-Jamal, K. T., Cakebread, A., Halket, J. M., and Kostarelos, K., "Blood circulation and tissue biodistribution of lipid-quantum dot (L-QD) hybrid vesicles intravenously administered in mice," *Bioconjug Chem*, vol. 20, pp. 1696–1702, Sep 2009.

[5] Albelda, S. M., Mette, S. A., Elder, D. E., Stewart, R., Damjanovich, L., Herlyn, M., and Buck, C. A., "Integrin distribution in malignant melanoma: association of the beta 3 subunit with tumor progression," *Cancer Res*, vol. 50, pp. 6757–6764, Oct 1990.

[6] Albrecht, M. and Creighton, J., "Anomalously intense raman spectra of pyridine at a silver electrode," *J Am Chem Soc*, vol. 99, no. 15, pp. 5215–5217, 1977.

[7] Aldana, J., Wang, Y., and Peng, X., "Photochemical instability of cdse nanocrystals coated by hydrophilic thiols," *J Am Chem Soc*, vol. 123, no. 36, pp. 8844–8850, 2001.

[8] American Academy of Opthamology, "Indocyanine green angiography," *Ophthalmology*, vol. 105, pp. 1564–1569, Aug 1998.

[9] Anderson, R. E. and Chan, W. C. W., "Systematic investigation of preparing biocompatible, single, and small ZnS-capped CdSe quantum dots with amphiphilic polymers," *ACS Nano*, vol. 2, pp. 1341–1352, Jul 2008.

[10] Argon, A. M., Duygun, U., Acar, E., Daglioz, G., Yenjay, L., Zekioglu, O., and Kapkac, M., "The use of periareolar intradermal Tc-99m tin colloid and peritumoral intraparenchymal isosulfan blue dye injections for determination of the sentinel lymph node," *Clin Nucl Med*, vol. 31, pp. 795–800, Dec 2006.

[11] Ashkenazi, A. and Dixit, V. M., "Death receptors: signaling and modulation," *Science*, vol. 281, pp. 1305–1308, Aug 1998.

[12] Ballou, B., Ernst, L. A., Andreko, S., Harper, T., Fitzpatrick, J. A. J., Waggoner, A. S., and Bruchez, M. P., "Sentinel lymph node imaging using quantum dots in mouse tumor models," *Bioconjug Chem*, vol. 18, pp. 389–396, Jan 2007.

[13] Ballou, B., Lagerholm, B. C., Ernst, L. A., Bruchez, M. P., and Waggoner, A. S., "Noninvasive imaging of quantum dots in mice," *Bioconjug Chem*, vol. 15, pp. 79–86, Jan 2004.

[14] Barbier, O., Jacquillet, G., Tauc, M., Cougnon, M., and Poujeol, P., "Effect of heavy metals on, and handling by, the kidney," *Nephron Physiol*, vol. 99, pp. 105–110, Jan 2005.

[15] Bawendi, M., Steigerwald, M., and Brus, L., "The quantum-mechanics of larger semiconductor clusters (quantum dots)," *Ann Rev Phys Chem*, vol. 41, pp. 477–496, Jan 1990.

[16] Beckman, J. S., Beckman, T. W., Chen, J., Marshall, P. A., and Freeman, B. A., "Apparent hydroxyl radical production by peroxynitrite: implications for endothelial injury from nitric oxide and superoxide," *Proc Natl Acad Sci USA*, vol. 87, pp. 1620–1624, Feb 1990.

[17] Benya, R., Quintana, J., and Brundage, B., "Adverse reactions to indocyanine green: a case report and a review of the literature," *Cathet Cardiovasc Diagn*, vol. 17, pp. 231–233, Aug 1989.

[18] Bertout, J. A., Patel, S. A., and Simon, M. C., "The impact of O_2 availability on human cancer," *Nat Rev Cancer*, vol. 8, pp. 967–975, Dec 2008.

[19] Berveiller, P., Mir, O., Veyrie, N., and Barranger, E., "The sentinel-node concept: a dramatic improvement in breast-cancer surgery," *Lancet Oncol*, vol. 11, p. 906, Sep 2010.

[20] Black, W. C. and Welch, H. G., "Advances in diagnostic imaging and overestimations of disease prevalence and the benefits of therapy," *N Engl J Med*, vol. 328, pp. 1237–1243, Apr 1993.

[21] Brown, K. E., Brunt, E. M., and Heinecke, J. W., "Immunohistochemical detection of myeloperoxidase and its oxidation products in kupffer cells of human liver," *Am J Pathol*, vol. 159, pp. 2081–2088, Dec 2001.

[22] Bruchez, M., Moronne, M., Gin, P., Weiss, S., and Alivisatos, A., "Semiconductor nanocrystals as fluorescent biological labels," *Science*, vol. 281, pp. 2013–2016, Jan 1998.

[23] Brus, L., "A simple model for the ionization potential, electron affinity, and aqueous redox potentials of small semiconductor crystallites," *J Chem Phys*, vol. 79, pp. 5566–5571, Jan 1983.

[24] Brus, L. E., "Electron electron and electron-hole interactions in small semiconductor crystallites: The size dependence of the lowest excited electronic state," *J Chem Phys*, vol. 80, pp. 4403–4409, Jan 1984.

[25] Brust, M., Walker, M., Bethell, D., Schiffrin, D. J., and Whyman, R., "Synthesis of thiol-derivatised gold nanoparticles in a two-phase liquid–liquid system," *Chem Commun*, pp. 801–802, Jan 1994.

[26] Burseck, P. R., Tsipursky, S. J., and Httich, R., "Fullerenes from the geological environment," *Science*, vol. 257, pp. 215–217, Jan 1992.

[27] Cao, G. and Prior, R. L., "Comparison of different analytical methods for assessing total antioxidant capacity of human serum," *Clin Chem*, vol. 44, pp. 1309–1315, Jun 1998.

[28] Cao, G. and Prior, R. L., "Measurement of oxygen radical absorbance capacity in biological samples," *Meth Enzymol*, vol. 299, pp. 50–62, Jan 1999.

[29] Carrabba, M., Robblee, L., and Rauh, R. D., "Prospect of utilizing surface-enhanced raman spectroscopy for bio-and biomedical sensing," *Proc SPIE*, vol. 1201, pp. 438–445, Jan 1990.

[30] Carrabba, M., Spencer, K., and Rauh, R. D., "Compact raman instrumentation for process and environmental monitoring," *Proc SPIE*, vol. 1434, pp. 127–134, Jan 1991.

[31] Chalupa, D., Morrow, P., Oberdörster, G., Utell, M. J., and Frampton, M. W., "Ultrafine particle deposition in subjects with asthma.," *Environ Health Persp*, vol. 112, pp. 879–882, Jan 2004.

[32] Chambers, A. F. and Matrisian, L. M., "Changing views of the role of matrix metalloproteinases in metastasis," *J Natl Cancer Inst*, vol. 89, pp. 1260–1270, Sep 1997.

[33] Chan, W. and Nie, S., "Quantum dot bioconjugates for ultrasensitive nonisotopic detection," *Science*, vol. 281, pp. 2016–2018, Jan 1998.

[34] Chance, B., "Optical method," *Ann Rev Biophys Biophys Chem*, vol. 20, no. 1, pp. 1–30, 1991.

[35] Chatterjee, K., Parker, D., Wurz, P., Lykke, K. R., Gruen, D. M., and Stock, L. M., "Fast one-step separation and purification of buckminsterfullerene, C_{60}, from carbon soot," *J Org Chem*, vol. 57, pp. 3253–3254, Jan 1992.

[36] Cheng, G., Kurita, S., Torigian, D. A., and Alavi, A., "Current status of sentinel lymph-node biopsy in patients with breast cancer," *Eur J Nucl Med Mol Imaging*, vol. 38, pp. 562–575, Aug 2010.

[37] Cherrick, G., Davidson, C., Leevy, C., and Stein, S., "Indocyanine green: observations on its physical properties, plasma decay, and hepatic extraction," *J Clin Invest*, vol. 39, pp. 592–600, Apr 1960.

[38] Cho, W.-S., Cho, M., Jeong, J., Choi, M., Han, B. S., Shin, H.-S., Hong, J., Chung, B. H., Jeong, J., and Cho, M.-H., "Size-dependent tissue kinetics of PEG-coated gold nanoparticles," *Toxicology and Applied Pharmacology*, vol. 245, pp. 116–123, May 2010.

[39] Choi, H., Ipe, B., Misra, P., Lee, J., Bawendi, M., and Frangioni, J., "Tissue- and organ-selective biodistribution of NIR fluorescent quantum dots," *Nano Lett*, vol. 9, pp. 2354–2359, May 2009.

[40] Choi, H. S., Liu, W., Misra, P., Tanaka, E., Zimmer, J. P., Ipe, B. I., Bawendi, M. G., and Frangioni, J. V., "Renal clearance of quantum dots," *Nat Biotechnol*, vol. 25, pp. 1165–1170, Oct 2007.

[41] Chou, L., Fischer, H., Perrault, S., and Chan, W., "Visualizing quantum dots in biological samples using silver staining," *Anal Chem*, vol. 81, pp. 4560–4565, May 2009.

[42] Clark, R. M., Whelan, T., Levine, M., Roberts, R., Willan, A., McCulloch, P., Lipa, M., Wilkinson, R. H., and Mahoney, L. J., "Randomized clinical trial of breast irradiation following lumpectomy and axillary dissection for node-negative breast cancer: an update," *J Natl Cancer Inst*, vol. 88, pp. 1659–1664, Nov 1996.

[43] Collins, S. J., "The HL-60 promyelocytic leukemia cell line: proliferation, differentiation, and cellular oncogene expression," *Blood*, vol. 70, pp. 1233–1244, Nov 1987.

[44] Collins, S. J., Ruscetti, F. W., Gallagher, R. E., and Gallo, R. C., "Terminal differentiation of human promyelocytic leukemia cells induced by dimethyl sulfoxide and other polar compounds," *Proc Natl Acad Sci USA*, vol. 75, pp. 2458–2462, May 1978.

[45] Collins, S. J., Ruscetti, F. W., Gallagher, R. E., and Gallo, R. C., "Normal functional characteristics of cultured human promyelocytic leukemia cells (HL-60) after induction of differentiation by dimethylsulfoxide," *J Exp Med*, vol. 149, pp. 969–974, Apr 1979.

[46] Counter, C. M., Avilion, A. A., LeFeuvre, C. E., Stewart, N. G., Greider, C. W., Harley, C. B., and Bacchetti, S., "Telomere shortening associated with chromosome instability is arrested in immortal cells which express telomerase activity," *EMBO J*, vol. 11, pp. 1921–1929, May 1992.

[47] Courty, S., Luccardini, C., Bellaiche, Y., Cappello, G., and Dahan, M., "Tracking individual kinesin motors in living cells using single quantum-dot imaging," *Nano Lett*, vol. 6, pp. 1491–1495, Jul 2006.

[48] Dahan, M., Lévi, S., Luccardini, C., Rostaing, P., Riveau, B., and Triller, A., "Diffusion dynamics of glycine receptors revealed by single-quantum dot tracking," *Science*, vol. 302, pp. 442–445, Oct 2003.

[49] Daniel, M.-C. and Astruc, D., "Gold nanoparticles: assembly, supramolecular chemistry, quantum-size-related properties, and applications toward biology, catalysis, and nanotechnology," *Chem Rev*, vol. 104, pp. 293–346, Jan 2004.

[50] Daugherty, A., Dunn, J. L., Rateri, D. L., and Heinecke, J. W., "Myeloperoxidase, a catalyst for lipoprotein oxidation, is expressed in human atherosclerotic lesions," *J Clin Invest*, vol. 94, pp. 437–444, Jul 1994.

[51] de González, A. B., Mahesh, M., Kim, K.-P., Bhargavan, M., Lewis, R., Mettler, F., and Land, C., "Projected cancer risks from computed tomographic scans performed in the United States in 2007," *Arch Int Med*, vol. 169, pp. 2071–2077, Dec 2009.

[52] De Grand, A. M. and Frangioni, J. V., "An operational near-infrared fluorescence imaging system prototype for large animal surgery," *Technol Cancer Res Treat*, vol. 2, pp. 553–562, Dec 2003.

[53] De Jong, W. H., Hagens, W. I., Krystek, P., Burger, M. C., Sips, A. J., and Geertsma, R. E., "Particle size-dependent organ distribution of gold nanoparticles after intravenous administration," *Biomaterials*, vol. 29, pp. 1912–1919, Apr 2008.

[54] de Wit, A., "Surface reactions at p-type and n-type ZnSe in aqueous solutions," *J Electroanal Chem*, vol. 366, pp. 163–170, Mar 1994.

[55] de Wit, A. and Kelley, J. J., "Surface-reactions of CdS in hypochlorite solutions," *J Electroanal Chem*, vol. 336, pp. 125–135, Jan 1992.

[56] Derfus, A., Chan, W., and Bhatia, S., "Probing the cytotoxicity of semiconductor quantum dots," *Nano Lett*, vol. 4, pp. 11–18, Jan 2004.

[57] Desser, R. K., Himmelhoch, S. R., Evans, W. H., Januska, M., Mage, M., and Shelton, E., "Guinea pig heterophil and eosinophil peroxidase," *Arch Biochem Biophys*, vol. 148, pp. 452–465, Feb 1972.

[58] Dexter, D. L., Kowalski, H. M., Blazar, B. A., Fligiel, Z., Vogel, R., and Heppner, G. H., "Heterogeneity of tumor cells from a single mouse mammary tumor," *Cancer Res*, vol. 38, pp. 3174–3181, Oct 1978.

[59] Diamond, G. L. and Zalups, R. K., "Understanding renal toxicity of heavy metals," *Toxicol Pathway*, vol. 26, pp. 92–103, Jan 1998.

[60] Dobrovolskaia, M. A., Aggarwal, P., Hall, J. B., and McNeil, S. E., "Preclinical studies to understand nanoparticle interaction with the immune system and its potential effects on nanoparticle biodistribution," *Mol Pharm*, vol. 5, pp. 487–495, Jan 2008.

[61] Donaldson, K., Stone, V., Tran, C. L., Kreyling, W., and Borm, P. J. A., "Nanotoxicology," *Occup Environ Med*, vol. 61, pp. 727–728, Sep 2004.

[62] Duan, H. and Nie, S., "Cell-penetrating quantum dots based on multivalent and endosome-disrupting surface coatings," *J Am Chem Soc*, vol. 129, pp. 3333–3338, Mar 2007.

[63] Dubertret, B., Skourides, P., Norris, D., Noireaux, V., Brivanlou, A., and Libchaber, A., "In vivo imaging of quantum dots encapsulated in phospholipid micelles," *Science*, vol. 298, pp. 1759–1762, Jan 2002.

[64] Efros, A. and Efros, A., "Interband absorption of light in a semiconductor sphere," *Sov Phys Semi*, vol. 16, pp. 772–775, 1982.

[65] Ekimov, A. I. and Onushchenko, A., "Quantum size effect in three-dimensional microscopic semiconductor crystals," *Pis'ma Zh. Eksp. Teor. Fiz*, vol. 34, no. 6, pp. 363–366, 1981.

[66] El-Sayed, I., Huang, X., and El-Sayed, M. A., "Surface plasmon resonance scattering and absorption of anti-EGFR antibody conjugated gold nanoparticles in cancer diagnostics: applications in oral cancer," *Nano Lett*, vol. 5, pp. 829–834, Jan 2005.

[67] El-Sayed, I., Huang, X., and El-Sayed, M. A., "Selective laser photo-thermal therapy of epithelial carcinoma using anti-EGFR antibody conjugated gold nanoparticles," *Cancer Lett*, vol. 239, pp. 129–135, Jan 2006.

[68] El-Sayed, M., "Small is different: Shape-, size-, and composition-dependent properties of some colloidal semiconductor nanocrystals," *Acc Chem Res*, vol. 37, pp. 326–333, Jan 2004.

[69] Elder, A., Gelein, R., Silva, V., Feikert, T., Opanashuk, L., Carter, J., Potter, R., Maynard, A., Ito, Y., Finkelstein, J., and Oberdörster, G., "Translocation of inhaled ultrafine manganese oxide particles to the central nervous system," *Environ Health Persp*, vol. 114, pp. 1172–1178, Jan 2006.

[70] Eng, J., "Receiver operating characteristic analysis: a primer," *Acad Radiol*, vol. 12, pp. 909–916, Jul 2005.

[71] Fang, J. Y. and Richardson, B. C., "The MAPK signalling pathways and colorectal cancer," *Lancet Oncol*, vol. 6, pp. 322–327, May 2005.

[72] Faraday, M., "The bakerian lecture: experimental relations of gold (and other metals) to light," *Phil Trans R Soc London*, vol. 147, pp. 145–181, 1857.

[73] Fernández-Suárez, M. and Ting, A. Y., "Fluorescent probes for super-resolution imaging in living cells," *Nat Rev Mol Cell Biol*, vol. 9, pp. 929–943, Dec 2008.

[74] Feynman, R. P., *The Pleasure of Finding Things Out*. Cambridge, MA: Perseus Books, 1999.

[75] Fischer, H. C. and Chan, W. C. W., "Nanotoxicity: the growing need for in vivo study," *Curr Opin Biotech*, vol. 18, pp. 565–571, Dec 2007.

[76] Fischer, H. C., Liu, L., Pang, K. S., and Chan, W. C. W., "Pharmacokinetics of nanoscale quantum dots: In vivo distribution, sequestration, and clearance in the rat," *Adv Funct Mater*, vol. 16, pp. 1299–1305, Jan 2006.

[77] Fitzpatrick, J. A. J., Andreko, S. K., Ernst, L. A., Waggoner, A. S., Ballou, B., and Bruchez, M. P., "Long-term persistence and spectral blue shifting of quantum dots in vivo," *Nano Lett*, vol. 9, pp. 2736–2741, Jul 2009.

[78] Fleischmann, M., Hendra, P. J., and McQuillan, A. J., "Raman spectra of pyridine adsorbed at a silver electrode," *Chem Phys Lett*, vol. 26, pp. 163–166, Jan 1974.

[79] Fojtik, A., Weller, H., and Henglein, A., "Photochemistry of semiconductor colloids. size quantization effects in q-cadmium arsenide," *Chem Phys Lett*, vol. 120, no. 6, pp. 552–554, 1985.

[80] Folkman, J., "Tumor angiogenesis: therapeutic implications," *N Engl J Med*, vol. 285, pp. 1182–1186, Nov 1971.

[81] Folkman, J., "Angiogenesis," *Ann Rev Med*, vol. 57, pp. 1–18, Jan 2006.

[82] Folkman, J. and Kalluri, R., "Cancer without disease," *Nature*, vol. 427, p. 787, Feb 2004.

[83] Frangioni, J. V., "The problem is background, not signal," *Mol Imaging*, vol. 8, pp. 303–304, Dec 2009.

[84] Frens, G., "Controlled nucleation for regulation of particle-size in monodisperse gold suspensions," *Nature Phys Sci*, vol. 241, pp. 20–22, Jan 1973.

[85] Fukumura, D. and Jain, R. K., "Tumor microvasculature and microenvironment: targets for anti-angiogenesis and normalization," *Microvasc Res*, vol. 74, pp. 72–84, Jan 2007.

[86] Gao, X., Cui, Y., Levenson, R. M., Chung, L. W. K., and Nie, S., "In vivo cancer targeting and imaging with semiconductor quantum dots," *Nat Biotechnol*, vol. 22, pp. 969–976, Aug 2004.

[87] Gimbrone, M. A., Leapman, S. B., Cotran, R. S., and Folkman, J., "Tumor dormancy in vivo by prevention of neovascularization," *J Exp Med*, vol. 136, pp. 261–276, Aug 1972.

[88] Gioux, S., Kianzad, V., Ciocan, R., Gupta, S., Oketokoun, R., and Frangioni, J. V., "High-power, computer-controlled, light-emitting diode-based light sources for fluorescence imaging and image-guided surgery," *Mol Imaging*, vol. 8, pp. 156–165, Jan 2009.

[89] Glaus, C., Rossin, R., and Welch..., M., "In vivo evaluation of ^{64}Cu-labeled magnetic nanoparticles as a dual-modality PET/MR imaging agent," *Bioconjug Chem*, vol. 21, pp. 715–722, Jan 2010.

[90] Gordon, I., Paoloni, M., Mazcko, C., and Khanna, C., "The Comparative Oncology Trials Consortium: using spontaneously occurring cancers in dogs to inform the cancer drug development pathway," *PLoS Med*, vol. 6, p. e1000161, Oct 2009.

[91] Haiss, W., Thanh, N. T. K., Aveyard, J., and Fernig, D. G., "Determination of size and concentration of gold nanoparticles from UV-vis spectra," *Anal Chem*, vol. 79, pp. 4215–4221, Jun 2007.

[92] Hampton, M. B., Kettle, A. J., and Winterbourn, C. C., "Inside the neutrophil phagosome: oxidants, myeloperoxidase, and bacterial killing," *Blood*, vol. 92, pp. 3007–3017, Nov 1998.

[93] Han, M., Gao, X., Su, J. Z., and Nie, S., "Quantum-dot-tagged microbeads for multiplexed optical coding of biomolecules," *Nat Biotechnol*, vol. 19, pp. 631–635, Jul 2001.

[94] Hanahan, D. and Weinberg, R. A., "The hallmarks of cancer," *Cell*, vol. 100, pp. 57–70, Jan 2000.

[95] Hardman, R., "A toxicologic review of quantum dots: toxicity depends on physicochemical and environmental factors," *Environ Health Persp*, vol. 114, pp. 165–172, Feb 2006.

[96] Hauck, T., Anderson, R., Fischer, H., Newbigging, S., and Chan, W., "In vivo quantum-dot toxicity assessment," *Small*, vol. 6, pp. 138–144, Sep 2009.

[97] Hawkins, M. J., Soon-Shiong, P., and Desai, N., "Protein nanoparticles as drug carriers in clinical medicine," *Adv Drug Deliv Rev*, vol. 60, pp. 876–885, May 2008.

[98] Hay, E. and Zuk, A., "Transformations between epithelium and mesenchyme: Normal, pathological, and experimentally induced," *Am J Kidney Dis*, vol. 26, pp. 678–690, Oct 1995.

[99] Hayflick, L., "The illusion of cell immortality," *Br J Cancer*, vol. 83, pp. 841–846, Oct 2000.

[100] Hayflick, L. and Moorhead, P. S., "The serial cultivation of human diploid cell strains," *Exp Cell Res*, vol. 25, pp. 585–621, Dec 1961.

[101] Heimberger, A. B., Hlatky, R., Suki, D., Yang, D., Weinberg, J., Gilbert, M., Sawaya, R., and Aldape, K., "Prognostic effect of epidermal growth factor receptor and EGFRvIII in glioblastoma multiforme patients," *Clin Cancer Res*, vol. 11, pp. 1462–1466, Feb 2005.

[102] Heldin, C.-H., Rubin, K., Pietras, K., and Ostman, A., "High interstitial fluid pressure—an obstacle in cancer therapy," *Nat Rev Cancer*, vol. 4, pp. 806–813, Oct 2004.

[103] Heller, A., "Conversion of sunlight into electrical power and photoassisted electrolysis of water in photoelectrochemical cells," *Acc Chem Res*, vol. 14, no. 5, pp. 154–162, 1981.

[104] Henglein, A., "Photochemistry of colloidal cadmium sulfide. 2. Effects of adsorbed methyl viologen and of colloidal platinum.," *J Phys Chem*, vol. 86, pp. 2291–2293, Jan 1982.

[105] Hilger, I., Hergt, R., and Kaiser, W. A., "Use of magnetic nanoparticle heating in the treatment of breast cancer," *IEEE Proc Nanobiotechnol*, vol. 152, pp. 33–39, Jan 2005.

[106] Hillyer, J. and Albrecht, R. M., "Gastrointestinal persorption and tissue distribution of differently sized colloidal gold nanoparticles," *J Pharm Sci*, vol. 90, pp. 1927–1936, Jan 2001.

[107] Hines, M. and Guyot-Sionnest, P., "Synthesis and characterization of strongly luminescing zns-capped cdse nanocrystals," *J Phys Chem*, vol. 100, no. 2, pp. 468–471, 1996.

[108] Hisamuddin, I. M. and Yang, V. W., "Genetics of colorectal cancer," *Medscape Gen Med*, vol. 6, p. 13, Jan 2004.

[109] Hollstein, M., Sidransky, D., Vogelstein, B., and Harris, C. C., "p53 mutations in human cancers," *Science*, vol. 253, pp. 49–53, Jul 1991.

[110] Holty, J.-E. C. and Gould, M. K., "When in doubt should we cut it out? The role of surgery in non-small cell lung cancer," *Thorax*, vol. 61, pp. 554–556, Jul 2006.

[111] Hoyer, P., Staudt, T., Engelhardt, J., and Hell, S. W., "Quantum dot blueing and blinking enables fluorescence nanoscopy," *Nano lett*, vol. 11, pp. 245–250, Jan 2011.

[112] Huang, D., Ou, B., Hampsch-Woodill, M., Flanagan, J. A., and Prior, R. L., "High-throughput assay of oxygen radical absorbance capacity (ORAC) using a multichannel liquid handling system coupled with a microplate fluorescence reader in 96-well format," *J Agr Food Chem*, vol. 50, pp. 4437–4444, Jul 2002.

[113] Huang, X., Jain, P., El-Sayed, I. H., and El-Sayed, M. A., "Determination of the minimum temperature required for selective photothermal destruction of cancer cells with the use of immunotargeted gold nanoparticles," *Photochem Photobiol*, vol. 82, pp. 412–417, Jan 2006.

[114] Hughes, M. and Nicklin, H., "The chemistry of pernitrites. Part I. Kinetics of decomposition of pernitrous acid," *J Chem Soc A*, vol. 1968, pp. 450–452, 1968.

[115] Iyer, S. S., Accardi, C. J., Ziegler, T. R., Blanco, R. A., Ritzenthaler, J. D., Rojas, M., Roman, J., and Jones, D. P., "Cysteine redox potential determines pro-inflammatory IL-1beta levels," *PLoS ONE*, vol. 4, p. e5017, Jan 2009.

[116] Jain, P. K., Huang, X., El-Sayed, I. H., and El-Sayed, M. A., "Noble metals on the nanoscale: optical and photothermal properties and some applications in imaging, sensing, biology, and medicine," *Acc Chem Res*, vol. 41, pp. 1578–1586, Dec 2008.

[117] Jain, R. K., "Transport of molecules in the tumor interstitium: a review," *Cancer Res*, vol. 47, pp. 3039–3051, Jun 1987.

[118] Jain, R. K., "Transport of molecules, particles, and cells in solid tumors," *Ann Rev Biomed Eng*, vol. 1, pp. 241–263, Jan 1999.

[119] Jain, R. K., "Delivery of molecular and cellular medicine to solid tumors," *Adv Drug Deliv Rev*, vol. 46, pp. 149–168, Mar 2001.

[120] Jeanmaire, D. L. and van Duyne, R. P., "Surface raman spectroelectrochemistry. part 1. heterocyclic, aromatic, and aliphatic amines adsorbed on the anodized silver electrode," *J Electroanal Chem*, vol. 84, pp. 1–20, Jan 1977.

[121] Jemal, A., Siegel, R., Xu, J., and Ward, E., "Cancer statistics, 2010," *CA: A Cancer Journal for Clinicians*, vol. 60, pp. 277–300, Jan 2010.

[122] Jiang, W., Kim, B. Y. S., Rutka, J. T., and Chan, W. C. W., "Nanoparticle-mediated cellular response is size-dependent," *Nat Nanotechnol*, vol. 3, pp. 145–150, Mar 2008.

[123] Johnson, B. E. and Rabin, M. S., "Patient subsets benefiting from adjuvant therapy following surgical resection of non-small cell lung cancer," *Clin Cancer Res*, vol. 11, pp. 5022s–5026s, Jul 2005.

[124] Josephson, L., Kircher, M. F., Mahmood, U., Tang, Y., and Weissleder, R., "Near-infrared fluorescent nanoparticles as combined MR/optical imaging probes," *Bioconjug Chem*, vol. 13, pp. 554–560, Jan 2002.

[125] Kairdolf, B. A., Smith, A. M., and Nie, S., "One-pot synthesis, encapsulation, and solubilization of size-tuned quantum dots with amphiphilic multidentate ligands," *J Am Chem Soc*, vol. 130, pp. 12866–12867, Oct 2008.

[126] Kanaya, N., Iwasaki, H., and Namiki, A., "Noninvasive icg clearance test for estimating hepatic blood flow during halothane and isoflurane anaesthesia," *Can J Anaesth*, vol. 42, pp. 209–212, Mar 1995.

[127] Katari, J., Colvin, V., and Alivisatos, A., "X-ray photoelectron-spectroscopy of CdSe nanocrystals with applications to studies of the nanocrystal surface," *J Phys Chem*, vol. 98, pp. 4109–4117, Jan 1994.

[128] Kelland, L. R., "Of mice and men: values and liabilities of the athymic nude mouse model in anticancer drug development," *Eur J Cancer*, vol. 40, pp. 827–836, Apr 2004.

[129] Kettle, A. J., Gedye, C. A., and Winterbourn, C. C., "Mechanism of inactivation of myeloperoxidase by 4-aminobenzoic acid hydrazide," *Biochem J*, vol. 321 (Pt. 2), pp. 503–508, Jan 1997.

[130] Kircher, M. F., Mahmood, U., King, R. S., Weissleder, R., and Josephson, L., "A multimodal nanoparticle for preoperative magnetic resonance imaging and intraoperative optical brain tumor delineation," *Cancer Res*, vol. 63, pp. 8122–8125, Dec 2003.

[131] Klebanoff, S. J., "Myeloperoxidase: friend and foe," *J Leuko Biol*, vol. 77, pp. 598–625, May 2005.

[132] Kobayashi, H., Ogawa, M., Alford, R., Choyke, P. L., and Urano, Y., "New strategies for fluorescent probe design in medical diagnostic imaging," *Chem Rev*, vol. 110, pp. 2620–2640, Dec 2009.

[133] Kobayashi, H., Ogawa, M., Kosaka, N., Choyke, P. L., and Urano, Y., "Multicolor imaging of lymphatic function with two nanomaterials: quantum dot-labeled cancer cells and dendrimer-based optical agents," *Nanomedicine (Lond)*, vol. 4, pp. 411–419, Jun 2009.

[134] Koch, U., Fojtik, A., Weller, H., and Henglein, A., "Photochemistry of semiconductor colloids. preparation of extremely small zno particles, fluorescence phenomena and size quantization effects* 1," *Chem Phys Lett*, vol. 122, no. 5, pp. 507–510, 1985.

[135] Krag, D. N., Anderson, S. J., Julian, T. B., Brown, A. M., Harlow, S. P., Ashikaga, T., Weaver, D. L., Miller, B. J., Jalovec, L. M., Frazier, T. G., Noyes, R. D., Robidoux, A., Scarth, H. M. C., Mammolito, D. M., McCready, D. R., Mamounas, E. P., Costantino, J. P., Wolmark, N., Breast, N. S. A., and Project, B., "Technical outcomes of sentinel-lymph-node resection and conventional axillary-lymph-node dissection in patients with clinically node-negative breast cancer: results from the NSABP B-32 randomised phase III trial," *Lancet Oncol*, vol. 8, pp. 881–888, Oct 2007.

[136] Kreyling, W. G., Semmler, M., and Möller, W., "Dosimetry and toxicology of ultrafine particles," *J Aerosol Med*, vol. 17, pp. 140–152, Aug 2004.

[137] Lee, H., Leavens, T., Mason, S., Monteiro-Riviere, N., and Riviere, J., "Comparison of quantum dot biodistribution with a blood-flow-limited physiologically based pharmacokinetic model," *Nano Lett*, vol. 9, pp. 794–799, Jan 2009.

[138] Li, S.-D. and Huang, L., "Pharmacokinetics and biodistribution of nanoparticles," *Mol Pharm*, vol. 5, pp. 496–504, Jan 2008.

[139] Lidke, K., Rieger, B., Jovin, T., and Heintzmann, R., "Superresolution by localization of quantum dots using blinking statistics," *Optics Exp*, vol. 13, pp. 7052–7062, Jan 2005.

[140] Lim, M. D., Dickherber, A., and Compton, C. C., "Before you analyze a human specimen, think quality, variability, and bias," *Anal Chem*, vol. 83, pp. 8–13, Jan 2011.

[141] Lin, P., Chen, J.-W., Chang, L. W., Wu, J.-P., Redding, L., Chang, H., Yeh, T.-K., Yang, C. S., Tsai, M.-H., Wang, H.-J., Kuo, Y.-C., and Yang, R. S. H., "Computational and ultrastructural toxicology of a nanoparticle, quantum dot 705, in mice," *Environ Sci Technol*, vol. 42, pp. 6264–6270, Jan 2008.

[142] Lin, S., Xie, X., Patel, M. R., Yang, Y.-H., Li, Z., Cao, F., Gheysens, O., Zhang, Y., Gambhir, S. S., Rao, J. H., and Wu, J. C., "Quantum dot imaging for embryonic stem cells," *BMC Biotechnol*, vol. 7, p. 67, Jan 2007.

[143] Lipert, R., Dawson, G., and Porter, M., "Immunoassay readout method using extrinsic Raman labels adsorbed on immunogold colloids," *Anal Chem*, vol. 71, pp. 4903–4908, Jan 1999.

[144] Liu, J., Lau, S. K., Varma, V. A., Moffitt, R. A., Caldwell, M., Liu, T., Young, A. N., Petros, J. A., Osunkoya, A. O., Krogstad, T., Leyland-Jones, B., Wang, M. D., and Nie, S., "Molecular mapping of tumor heterogeneity on clinical tissue specimens with multiplexed quantum dots," *ACS Nano*, vol. 4, pp. 2755–2765, May 2010.

[145] López-Otín, C. and Matrisian, L. M., "Emerging roles of proteases in tumour suppression," *Nat Rev Cancer*, vol. 7, pp. 800–808, Oct 2007.

[146] Lusted, L. B., "Signal detectability and medical decision-making," *Science*, vol. 171, pp. 1217–1219, Mar 1971.

[147] Ma, J., Chen, J.-Y., Zhang, Y., Wang, P.-N., Guo, J., Yang, W.-L., and Wang, C.-C., "Photochemical instability of thiol-capped CdTe quantum dots in aqueous solution and living cells: Process and mechanism," *J Phys Chem B*, vol. 111, pp. 12012–12016, Jan 2007.

[148] Mancini, M. C., Kairdolf, B. A., Smith, A. M., and Nie, S., "Oxidative quenching and degradation of polymer-encapsulated quantum dots: new insights into the long-term fate and toxicity of nanocrystals in vivo," *J Am Chem Soc*, vol. 130, pp. 10836–10837, Aug 2008.

[149] Manna, L., Scher, E. C., Li, L.-S., and Alivisatos, A. P., "Epitaxial growth and photochemical annealing of graded CdS/ZnS shells on colloidal CdSe nanorods nanorods," *J Am Chem Soc*, vol. 124, pp. 7136–7145, Jun 2002.

[150] Manoharan, R., Wang, Y., and Feld, M., "Histochemical analysis of biological tissues using Raman spectroscopy," *Spectrochim Acta A*, vol. 52, pp. 215–249, Jan 1996.

[151] Martelli, G., Miceli, R., Daidone, M. G., Vetrella, G., Cerrotta, A. M., Piromalli, D., and Agresti, R., "Axillary dissection versus no axillary dissection in elderly patients with breast cancer and no palpable axillary nodes: results after 15 years of follow-up," *Ann Surg Oncol*, vol. 18, pp. 125–133, Jan 2011.

[152] Matsumura, Y. and Maeda, H., "A new concept for macromolecular therapeutics in cancer chemotherapy: mechanism of tumoritropic accumulation of proteins and the antitumor agent smancs," *Cancer Res*, vol. 46, pp. 6387–6392, Dec 1986.

[153] Mattoussi, H., Mauro, J., Goldman, E., Anderson, G., Sundar, V., Mikulec, F., and Bawendi, M., "Self-assembly of CdSe-ZnS quantum dot bioconjugates using an engineered recombinant protein," *J Am Chem Soc*, vol. 122, no. 49, pp. 12142–12150, 2000.

[154] Mayeno, A. N., Curran, A. J., Roberts, R. L., and Foote, C. S., "Eosinophils preferentially use bromide to generate halogenating agents," *J Biol Chem*, vol. 264, pp. 5660–5668, Apr 1989.

[155] McCarthy, J. R. and Weissleder, R., "Multifunctional magnetic nanoparticles for targeted imaging and therapy," *Adv Drug Deliv Rev*, vol. 60, pp. 1241–1251, Jan 2008.

[156] Mcneil, S. E., "Nanotechnology for the biologist," *J Leuko Biol*, vol. 78, pp. 585–594, May 2005.

[157] McPherson, R. A. and Pincus, M. R., *Henry's Clinical Diagnosis and Management by Laboratory Methods*. Philidelphia, PA: Saunders/Elsevier, 2007.

[158] McQuarrie, D. A., *Quantum Chemistry*. Sausalito, CA: University Science Books, 1983.

[159] Medintz, I. L., Uyeda, H. T., Goldman, E. R., and Mattoussi, H., "Quantum dot bioconjugates for imaging, labelling and sensing," *Nat Mater*, vol. 4, pp. 435–446, Jun 2005. 47 77.

[160] Michalet, X., Pinaud, F. F., Bentolila, L. A., Tsay, J. M., Doose, S., Li, J. J., Sundaresan, G., Wu, A. M., Gambhir, S. S., and Weiss, S., "Quantum dots for live cells, in vivo imaging, and diagnostics," *Science*, vol. 307, pp. 538–544, Jan 2005.

[161] Mie, G., "Contributions to the optics of turbid media, particularly of colloidal metal solutions," *Annalen der Physik*, vol. 25, no. 3, pp. 377–445, 1908.

[162] Miyaura, C., Abe, E., Suda, T., and Kuroki, T., "Alternative differentiation of human promyelocytic leukemia cells (HL-60) induced selectively by retinoic acid and 1-alpha,25-dihydroxyvitamin D3," *Cancer Res*, vol. 45, pp. 4244–4248, Sep 1985.

[163] Moghimi, S., Hunter, A., and Murray, J., "Long-circulating and target-specific nanoparticles: Theory to practice," *Pharmacol Rev*, vol. 53, pp. 283–318, Jun 2001.

[164] Moghimi, S. M. and Davis, S. S., "Innovations in avoiding particle clearance from blood by kupffer cells: cause for reflection," *Crit Rev Ther Drug Carrier Syst*, vol. 11, pp. 31–59, Jan 1994.

[165] Mohs, A., Duan, H., Kairdolf, B., Smith, A. M., and Nie, S., "Proton-resistant quantum dots: Stability in gastrointestinal fluids and implications for oral delivery of nanoparticle agents," *Nano Res*, vol. 2, pp. 500–508, Jan 2009.

[166] Mohs, A. M., Mancini, M. C., Singhal, S., Provenzale, J. M., Leyland-Jones, B., Wang, M. D., and Nie, S., "Hand-held spectroscopic device for in vivo and intraoperative tumor detection: Contrast enhancement, detection sensitivity, and tissue penetration," *Anal Chem*, vol. 82, pp. 9058–9065, Oct 2010.

[167] Monteiro-Riviere, L., "Assessment of quantum dot penetration into intact, tape-stripped, abraded and flexed rat skin," *Skin Pharmacol Physiol*, vol. 21, pp. 166–180, Jan 2008.

[168] Moriarty-Craige, S. E. and Jones, D. P., "Extracellular thiols and thiol/disulfide redox in metabolism," *Annu Rev Nutr*, vol. 24, pp. 481–509, Jan 2004.

[169] Morris, J. C., "Acid ionization constant of HOCl from 5 to 35 degrees," *J Phys Chem*, vol. 70, pp. 3798–3805, Jan 1966.

[170] Motz, J. T., Fitzmaurice, M., Miller, A., Gandhi, S. J., Haka, A. S., Galindo, L. H., Dasari, R. R., Kramer, J. R., and Feld, M. S., "In vivo Raman spectral pathology of human atherosclerosis and vulnerable plaque," *J Biomed Opt*, vol. 11, p. 021003, Jan 2006.

[171] Motz, J. T., Gandhi, S. J., Scepanovic, O. R., Haka, A. S., Kramer, J. R., Dasari, R. R., and Feld, M. S., "Real-time Raman system for in vivo disease diagnosis," *J Biomed Opt*, vol. 10, p. 031113, Jan 2005.

[172] Murphy, C. J., Gole, A. M., Stone, J. W., Sisco, P. N., Alkilany, A. M., Goldsmith, E. C., and Baxter, S. C., "Gold nanoparticles in biology: beyond toxicity to cellular imaging," *Acc Chem Res*, vol. 41, pp. 1721–1730, Dec 2008.

[173] Murray, C., Norris, D., and Bawendi, M., "Synthesis and characterization of nearly monodisperse CdE (E = sulfur, selenium, tellurium) semiconductor nanocrystallites," *J Am Chem Soc*, vol. 115, no. 19, pp. 8706–8715, 1993.

[174] Naito, M., Hasegawa, G., and Takahashi, K., "Development, differentiation, and maturation of Kupffer cells," *Microsc Res Tech*, vol. 39, pp. 350–364, Nov 1997.

[175] Narui, K., Ishikawa, T., Kito, A., Shimizu, D., Chishima, T., Momiyama, N., Ichikawa, Y., Sasaki, T., Nozawa, A., Inayama, Y., Shimada, H., and Endo, I., "Observational study of blue dye-assisted four-node sampling for axillary staging in early breast cancer," *Eur J Surg Oncol*, vol. 36, pp. 731–736, Aug 2010.

[176] National Center for Health Statistics, with Chartbook, "Health, United States, 2008," Hyattsville, MD, 2009.

[177] National Nanotechnology Initiative, "What is nanotechnology." Internet, http://www.nano.gov/html/facts/whatIsNano.html, Feb 2011.

[178] Nauseef, W. M., Metcalf, J. A., and Root, R. K., "Role of myeloperoxidase in the respiratory burst of human neutrophils," *Blood*, vol. 61, pp. 483–492, Mar 1983.

[179] Ngô, C., Pollet, A. G., Laperrelle, J., Ackerman, G., Gomme, S., Thibault, F., Fourchotte, V., and Salmon, R. J., "Intraoperative ultrasound localization of nonpalpable breast cancers," *Ann Surg Oncol*, vol. 14, pp. 2485–2489, Sep 2007.

[180] Nguyen, Q. T., Olson, E. S., Aguilera, T. A., Jiang, T., Scadeng, M., Ellies, L. G., and Tsien, R. Y., "Surgery with molecular fluorescence imaging using activatable cell-penetrating peptides decreases residual cancer and improves survival," *Proc Natl Acad Sci USA*, vol. 107, pp. 4317–4322, Mar 2010.

[181] Nicholls, S. J. and Hazen, S. L., "Myeloperoxidase and cardiovascular disease," *Arterioscl Throm Vas*, vol. 25, pp. 1102–1111, Jun 2005.

[182] Nie, S. and Emory, S., "Probing single molecules and single nanoparticles by surface-enhanced raman scattering," *Science*, vol. 275, no. 5303, pp. 1102–1106, 1997.

[183] Nirmal, M. and Brus, L., "Luminescence photophysics in semiconductor nanocrystals," *Acc Chem Res*, vol. 32, pp. 407–414, Jan 1999.

[184] Ntziachristos, V., Ripoll, J., and Weissleder, R., "Would near-infrared fluorescence signals propagate through large human organs for clinical studies? errata," *Optics Lett*, vol. 27, pp. 333–335, Sep 2002.

[185] Oberdörster, G., Oberdörster, E., and Oberdörster, J., "Nanotoxicology: An emerging discipline evolving from studies of ultrafine particles," *Environ Health Persp*, vol. 113, pp. 823–839, Jan 2005.

[186] Oberdörster, G., Sharp, Z., Atudorei, V., Elder, A., Gelein, R., Kreyling, W., and Cox, C., "Translocation of inhaled ultrafine particles to the brain," *Inhal Toxicol*, vol. 16, pp. 437–445, Jan 2004.

[187] Obuchowski, N. A., "Roc analysis," *Am J Roentgenol*, vol. 184, pp. 364–372, Feb 2005.

[188] Oh, A. S., Lorant, L. A., Holloway, J. N., Miller, D. L., Kern, F. G., and El-Ashry, D., "Hyperactivation of MAPK induces loss of ER-alpha expression in breast cancer cells," *Mol Endocrinol*, vol. 15, pp. 1344–1359, Aug 2001.

[189] O'Neal, D., Hirsch, L., Halas, N., Payne, J. D., and West, J. L., "Photo-thermal tumor ablation in mice using near infrared-absorbing nanoparticles," *Cancer Lett*, vol. 209, pp. 171–176, Jan 2004.

[190] O'Neal, D. P., Hirsch, L., Halas, N., Payne, J., and West, J., "Photothermal cancer therapy using intravenously injected near-infrared-absorbing nanoparticles," *Proc SPIE*, vol. 149, Jan 2005.

[191] Pan, Y., Neuss, S., Leifert, A., Fischler, M., Wen, F., Simon, U., Schmid, G., Brandau, W., and Jahnen-Dechent, W., "Size-dependent cytotoxicity of gold nanoparticles," *Small*, vol. 3, pp. 1941–1949, Nov 2007.

[192] Paoloni, M. and Khanna, C., "Translation of new cancer treatments from pet dogs to humans," *Nat Rev Cancer*, vol. 8, pp. 147–56, Feb 2008.

[193] Parry, M. F., Root, R. K., Metcalf, J. A., Delaney, K. K., Kaplow, L. S., and Richar, W. J., "Myeloperoxidase deficiency: prevalence and clinical significance," *Ann Intern Med*, vol. 95, pp. 293–301, Sep 1981.

[194] Pathak, S., Choi, S., Arnheim, N., and Thompson, M., "Hydroxylated quantum dots as luminescent probes for in situ hybridization," *J Am Chem Soc*, vol. 123, no. 17, pp. 4103–4104, 2001.

[195] Patterson, M. S., Chance, B., and Wilson, B. C., "Time resolved reflectance and transmittance for the non-invasive measurement of tissue optical properties," *Appl Opt*, vol. 28, pp. 2331–2336, Jun 1989.

[196] Pattison, D. I. and Davies, M. J., "Absolute rate constants for the reaction of hypochlorous acid with protein side chains and peptide bonds," *Chem Res Toxicol*, vol. 14, pp. 1453–1464, Oct 2001.

[197] Peng, X., Schlamp, M., Kadavanich, A., and Alivisatos, A., "Epitaxial growth of highly luminescent CdSe/CdS core/shell nanocrystals with photostability and electronic accessibility," *J Am Chem Soc*, vol. 119, pp. 7019–7029, Jan 1997.

[198] Philip, R., Penzkofer, A., Baumler, W., Szeimies, R., and Abels, C., "Absorption and fluorescence spectroscopic investigation of indocyanine green," *J Photochem Photobiol A*, vol. 96, pp. 137–148, Jan 1996.

[199] Pic, E., Pons, T., Bezdetnaya, L., Leroux, A., Guillemin, F., Dubertret, B., and Marchal, F., "Fluorescence imaging and whole-body biodistribution of near-infrared-emitting quantum dots after subcutaneous injection for regional lymph node mapping in mice," *Mol Imaging Biol*, vol. 12, pp. 394–405, Nov 2009.

[200] Pradhan, N., Goorskey, D., Thessing, J., and Peng, X., "An alternative of CdSe nanocrystal emitters: pure and tunable impurity emissions in znse nanocrystals nanocrystal emitters: pure and tunable impurity emissions in ZnSe nanocrystals," *J Am Chem Soc*, vol. 127, pp. 17586–17587, Jan 2005.

[201] Provenzale, J. M., "Nephrogenic systemic fibrosis: some considerations on the debate regarding its cause," *Am J Roentgenol*, vol. 191, pp. 1867–1869, Dec 2008.

[202] Qian, X., Peng, X.-H., Ansari, D. O., Yin-Goen, Q., Chen, G. Z., Shin, D. M., Yang, L., Young, A. N., Wang, M. D., and Nie, S., "In vivo tumor targeting and spectroscopic detection with surface-enhanced Raman nanoparticle tags," *Nat Biotechnol*, vol. 26, pp. 83–90, Jan 2008.

[203] Raman, C. V. and Krishnan, K. S., "A new type of secondary radiation," *Nature*, vol. 121, pp. 501–502, Jan 1928.

[204] Ramina, R., Neto, M. C., Giacomelli, A., Barros, E., Vosgerau, R., Nascimento, A., and Coelho, G., "Optimizing costs of intraoperative magnetic resonance imaging. A series of 29 glioma cases," *Acta Neurochir*, vol. 152, pp. 27–33, Jan 2010.

[205] Renan, M. J., "How many mutations are required for tumorigenesis? Implications from human cancer data," *Mol Carcinog*, vol. 7, pp. 139–146, Jan 1993.

[206] Reynolds, J. S., Troy, T. L., Mayer, R. H., Thompson, A. B., Waters, D. J., Cornell, K. K., Snyder, P. W., and Sevick-Muraca, E. M., "Imaging of spontaneous canine mammary tumors using fluorescent contrast agents," *Photochem Photobiol*, vol. 70, pp. 87–94, Jul 1999.

[207] Rice-Evans, C. and Miller, N. J., "Total antioxidant status in plasma and body fluids," *Meth Enzymol*, vol. 234, pp. 279–293, Jan 1994.

[208] Roche, M., Rondeau, P., Singh, N. R., Tarnus, E., and Bourdon, E., "The antioxidant properties of serum albumin," *FEBS Letters*, vol. 582, pp. 1783–1787, Jan 2008.

[209] Roos, D. and Winterbourn, C. C., "Immunology: Lethal weapons," *Science*, vol. 296, pp. 669–671, Apr 2002.

[210] Rosell, R., Taron, M., Reguart, N., Isla, D., and Moran, T., "Epidermal growth factor receptor activation: how exon 19 and 21 mutations changed our understanding of the pathway," *Clin Cancer Res*, vol. 12, pp. 7222–7231, Dec 2006.

[211] Rosen, A. B., Kelly, D. J., Schuldt, A. J. T., Lu, J., Potapova, I. A., Doronin, S. V., Robichaud, K. J., Robinson, R. B., Rosen, M. R., Brink, P. R., Gaudette, G. R., and Cohen, I. S., "Finding fluorescent needles in the cardiac haystack: tracking human mesenchymal stem cells labeled with quantum dots for quantitative in vivo three-dimensional fluorescence analysis," *Stem Cells*, vol. 25, pp. 2128–2138, Aug 2007.

[212] Rosen, H. and Klebanoff, S. J., "Chemiluminescence and superoxide production by myeloperoxidase-deficient leukocytes," *J Clin Invest*, vol. 58, pp. 50–60, Jul 1976.

[213] Rossetti, R. and Brus, L., "Electron-hole recombination emission as a probe of surface chemistry in aqueous cadmium sulfide colloids," *J Phys Chem*, vol. 86, pp. 4470–4472, Nov 1982.

[214] Ryman-Rasmussen, J., Riviere, J., and Monteiro-Riviere, N. A., "Penetration of intact skin by quantum dots with diverse physicochemical properties," *Toxicol Sci*, vol. 91, pp. 159–165, Jan 2006.

[215] Ryman-Rasmussen, J. P., Riviere, J. E., and Monteiro-Riviere, N. A., "Surface coatings determine cytotoxicity and irritation potential of quantum dot nanoparticles in epidermal keratinocytes," *J Invest Dermatol*, vol. 127, pp. 143–153, Jan 2007.

[216] Sadauskas, E., Danscher, G., Stoltenberg, M., Vogel, U., Larsen, A., and Wallin, H., "Protracted elimination of gold nanoparticles from mouse liver," *Nanomedicine*, vol. 5, pp. 162–169, Jun 2009.

[217] Saint-Michel, E., Giannone, G., Choquet, D., and Thoumine, O., "Neurexin/neuroligin interaction kinetics characterized by counting single cell-surface attached quantum dots," *Biophys J*, vol. 97, pp. 480–489, Jul 2009.

[218] Santibáñez-Koref, M. F., Birch, J. M., Hartley, A. L., Jones, P. H., Craft, A. W., Eden, T., Crowther, D., Kelsey, A. M., and Harris, M., "p53 germline mutations in Li-Fraumeni syndrome," *Lancet*, vol. 338, pp. 1490–1491, Dec 1991.

[219] Sausville, E. A. and Feigal, E., "Evolving approaches to cancer drug discovery and development at the National Cancer Institute, USA," *Ann Oncol*, vol. 10, pp. 1287–1291, Nov 1999.

[220] Sausville, E. A. and Burger, A. M., "Contributions of human tumor xenografts to anticancer drug development," *Cancer Res*, vol. 66, pp. 3351–3354, Apr 2006.

[221] Schipper, M. L., Iyer, G., Koh, A. L., Cheng, Z., Ebenstein, Y., Aharoni, A., Keren, S., Bentolila, L. A., Li, J., Rao, J., Chen, X., Banin, U., Wu, A. M., Sinclair, R., Weiss, S., and Gambhir, S. S., "Particle size, surface coating, and PEGylation influence the biodistribution of quantum dots in living mice," *Small*, vol. 5, pp. 126–134, Jan 2009.

[222] Schirrmeister, H., Kotzerke, J., Vogl, F., Buck, A., Czech, N., Koretz, K., Helm, G., Kreienberg, R., and Kühn, T., "Prospective evaluation of factors influencing success rates of sentinel node biopsy in 814 breast cancer patients," *Cancer Biother Radiopharm*, vol. 19, pp. 784–790, Dec 2004.

[223] Schmidt, H. and Weller, H., "Quantum size effects in semiconductor crystallites: calculation of the energy spectrum for the confined exciton," *Chem Phys Lett*, vol. 129, no. 6, pp. 615–618, 1986.

[224] Sevick-Muraca, E. M., Houston, J. P., and Gurfinkel, M., "Fluorescence-enhanced, near infrared diagnostic imaging with contrast agents," *Curr Opin Chem Biol*, vol. 6, pp. 642–650, Oct 2002.

[225] Sevick-Muraca, E. M., Sharma, R., Rasmussen, J. C., Marshall, M. V., Wendt, J. A., Pham, H. Q., Bonefas, E., Houston, J. P., Sampath, L., Adams, K. E., Blanchard, D. K., Fisher, R. E., Chiang, S. B., Elledge, R., and Mawad, M. E., "Imaging of lymph flow in breast cancer patients after microdose administration of a near-infrared fluorophore: feasibility study," *Radiology*, vol. 246, pp. 734–741, Mar 2008.

[226] Shiohara, A., Hoshino, A., Hanaki, K., Suzuki, K., and Yamamato, K., "On the cyto-toxicity caused by quantum dots," *Microbiol Immunol*, vol. 48, pp. 669–675, Jan 2004.

[227] Simmons, R. M., Smith, S. M., and Osborne, M. P., "Methylene blue dye as an alternative to isosulfan blue dye for sentinel lymph node localization," *Breast J*, vol. 7, pp. 181–183, Jan 2001.

[228] Singletary, S. E., "Breast cancer management: the road to today," *Cancer*, vol. 113, pp. 1844–1849, Oct 2008.

[229] Smith, A., Duan, H., Rhyner, M., Ruan, G., and Nie, S., "A systematic examination of surface coatings on the optical and chemical properties of semiconductor quantum dots," *Phys Chem Chem Phys*, vol. 8, no. 33, pp. 3895–3903, 2006.

[230] Smith, A., Gao, X., and Nie, S., "Quantum dot nanocrystals for in vivo molecular and cellular imaging," *Photochem Photobiol*, vol. 80, pp. 377–385, Jan 2004.

[231] Smith, A. M., Mancini, M. C., and Nie, S., "Bioimaging: second window for in vivo imaging," *Nature Nanotech*, vol. 4, pp. 710–711, Nov 2009.

[232] Smith, A. M. and Nie, S., "Minimizing the hydrodynamic size of quantum dots with multifunctional multidentate polymer ligands," *J Am Chem Soc*, vol. 130, pp. 11278–11279, Aug 2008.

[233] Smith, A. M. and Nie, S., "Nanocrystal synthesis in an amphibious bath: Spontaneous generation of hydrophilic and hydrophobic surface coatings," *Angew Chem Int Ed Engl*, vol. 47, pp. 9916–9921, Jan 2008.

[234] Smith, A. M. and Nie, S., "Semiconductor nanocrystals: Structure, properties, and band gap engineering," *Acc Chem Res*, vol. 43, pp. 190–200, Oct 2010.

[235] Smith, A. M., Ruan, G., Rhyner, M. N., and Nie, S., "Engineering luminescent quantum dots for in vivo molecular and cellular imaging," *Ann Biomed Eng*, vol. 34, pp. 3–14, Jan 2006.

[236] Sonavane, G., Tomoda, K., and Makino, K., "Biodistribution of colloidal gold nanoparticles after intravenous administration: Effect of particle size," *Coll Surf B*, vol. 66, pp. 274–280, Oct 2008.

[237] Spira, A. and Ettinger, D. S., "Multidisciplinary management of lung cancer," *N Engl J Med*, vol. 350, pp. 379–392, Jan 2004.

[238] Srivastava, S., Zou, Z. Q., Pirollo, K., Blattner, W., and Chang, E. H., "Germline transmission of a mutated p53 gene in a cancer-prone family with Li-Fraumeni syndrome," *Nature*, vol. 348, pp. 747–749, Jan 1990.

[239] Steigerwald, M. L. and Brus, L. E., "Semiconductor crystallites: a class of large molecules," *Acc Chem Res*, vol. 23, pp. 183–188, Jan 1990.

[240] Stern, S. T. and McNeil, S. E., "Nanotechnology safety concerns revisited," *Toxicol Sci*, vol. 101, pp. 4–21, Aug 2007.

[241] Sumimoto, H., Imabayashi, F., Iwata, T., and Kawakami, Y., "The BRAF-MAPK signaling pathway is essential for cancer-immune evasion in human melanoma cells," *J Exp Med*, vol. 203, pp. 1651–1656, Jul 2006.

[242] Swanson, G. P., Rynearson, K., and Symmonds, R., "Significance of margins of excision on breast cancer recurrence," *Am J Clin Oncol*, vol. 25, pp. 438–441, Oct 2002.

[243] Swirski, F. K., Nahrendorf, M., Etzrodt, M., Wildgruber, M., Cortez-Retamozo, V., Panizzi, P., Figueiredo, J.-L., Kohler, R. H., Chudnovskiy, A., Waterman, P., Aikawa, E., Mempel, T. R., Libby, P., Weissleder, R., and Pittet, M. J., "Identification of splenic reservoir monocytes and their deployment to inflammatory sites," *Science*, vol. 325, pp. 612–616, Jul 2009.

[244] Tanaka, E., Choi, H. S., Fujii, H., Bawendi, M. G., and Frangioni, J. V., "Image-guided oncologic surgery using invisible light: completed pre-clinical development for sentinel lymph node mapping," *Ann Surg Oncol*, vol. 13, pp. 1671–1681, Dec 2006.

[245] Tanaka, H., Abe, E., Miyaura, C., Shiina, Y., and Suda, T., "1-alpha,25-dihydroxyvitamin D3 induces differentiation of human promyelocytic leukemia cells (HL-60) into monocyte-macrophages, but not into granulocytes," *Biochem Biophys Res Comm*, vol. 117, pp. 86–92, Nov 1983.

[246] Taton, T. A., Mirkin, C. A., and Letsinger, R. L., "Scanometric DNA array detection with nanoparticle probes," *Science*, vol. 289, pp. 1757–1760, Sep 2000.

[247] Thomas, E. L., "Myeloperoxidase-hydrogen peroxide-chloride antimicrobial system: effect of exogenous amines on antibacterial action against escherichia coli," *Infect Immun*, vol. 25, pp. 110–116, Jul 1979.

[248] Thomas, E. L., "Myeloperoxidase, hydrogen peroxide, chloride antimicrobial system: nitrogen-chlorine derivatives of bacterial components in bactericidal action against escherichia coli," *Infect Immun*, vol. 23, pp. 522–531, Feb 1979.

[249] Thompson, E. W., Newgreen, D. F., and Tarin, D., "Carcinoma invasion and metastasis: a role for epithelial-mesenchymal transition?," *Cancer Res*, vol. 65, pp. 5991–5995, Jul 2005.

[250] Torchilin, V., "Liposomes as targetable drug carriers," *Crit Rev Ther Drug Carrier Syst*, vol. 2, pp. 65–115, Jan 1985.

[251] Torchilin, V., "Drug targeting," *Eu J Pharm Sci*, vol. 11, pp. S81–S91, Jan 2000.

[252] Troyan, S. L., Kianzad, V., Gibbs-Strauss, S. L., Gioux, S., Matsui, A., Oketokoun, R., Ngo, L., Khamene, A., Azar, F., and Frangioni, J. V., "The FLARE intraoperative near-infrared fluorescence imaging system: a first-in-human clinical trial in breast cancer sentinel lymph node mapping," *Ann Surg Oncol*, vol. 16, pp. 2943–2952, Oct 2009.

[253] Turkevich, J., Stevenson, P. C., and Hillier, J., "A study of the nucleation and growth processes in the synthesis of colloidal gold," *Disc Faraday Soc*, vol. 11, pp. 55–75, Jan 1951.

[254] U.S. Department of Energy Office of Basic Energy Sciences, "The scale of things." Internet, http://www.science.doe.gov/bes/scale_of_things.html, Jan 2011.

[255] van Dalen, C. J. and Kettle, A. J., "Substrates and products of eosinophil peroxidase," *Biochem J*, vol. 358, pp. 233–239, Aug 2001.

[256] Veronesi, U., Paganelli, G., Viale, G., Luini, A., Zurrida, S., Galimberti, V., Intra, M., Veronesi, P., Maisonneuve, P., Gatti, G., Mazzarol, G., Cicco, C. D., Manfredi, G., and Fernández, J. R., "Sentinel-lymph-node biopsy as a staging procedure in breast cancer: update of a randomised controlled study," *Lancet Oncol*, vol. 7, pp. 983–990, Dec 2006.

[257] Vitai, M. and Góth, L., "Reference ranges of normal blood catalase activity and levels in familial hypocatalasemia in hungary," *Clin Chim Acta*, vol. 261, pp. 35–42, May 1997.

[258] Wagner, E. F. and Nebreda, A. R., "Signal integration by JNK and p38 MAPK pathways in cancer development," *Nat Rev Cancer*, vol. 9, pp. 537–549, Aug 2009.

[259] Wagner, F. E., Haslbeck, S., Stievano, L., Calogero, S., Pankhurst, Q. A., and Martinek, K. P., "Before striking gold in gold-ruby glass," *Nature*, vol. 407, pp. 691–692, Oct 2000.

[260] Walker, N. J. and Bucher, J. R., "A 21st century paradigm for evaluating the health hazards of nanoscale materials?," *Toxicol Sci*, vol. 110, pp. 251–254, Aug 2009.

[261] Weinstein, S., Obuchowski, N. A., and Lieber, M. L., "Clinical evaluation of diagnostic tests," *Am J Roentgenol*, vol. 184, pp. 14–19, Jan 2005.

[262] Weissleder, R., "A clearer vision for in vivo imaging," *Nat Biotechnol*, vol. 19, pp. 316–317, Apr 2001.

[263] Weller, H., Fojtik, A., and Henglein, A., "Photochemistry of semiconductor colloids: Properties of extremely small particles of Cd_3P_2 and Zn_3P_2," *Chem Phys Lett*, vol. 117, no. 5, pp. 485–488, 1985.

[264] Willcox, B. J., Curb, J. D., and Rodriguez, B. L., "Antioxidants in cardiovascular health and disease: key lessons from epidemiologic studies," *Am J Cardiol*, vol. 101, pp. 75D–86D, May 2008.

[265] Winterbourn, C. C. and Metodiewa, D., "Reactivity of biologically important thiol compounds with superoxide and hydrogen peroxide," *Free Radic Biol Med*, vol. 27, pp. 322–328, Aug 1999.

[266] Wright, G., Manser, R. L., Byrnes, G., Hart, D., and Campbell, D. A., "Surgery for non-small cell lung cancer: systematic review and meta-analysis of randomised controlled trials," *Thorax*, vol. 61, pp. 597–603, Jul 2006.

[267] Wu, A. H. B., "Novel biomarkers of cardiovascular disease: myeloperoxidase for acute and/or chronic heart failure?," *Clin Chem*, vol. 55, pp. 12–14, Jan 2009.

[268] Wu, X., Beecher, G. R., Holden, J. M., Haytowitz, D. B., Gebhardt, S. E., and Prior, R. L., "Lipophilic and hydrophilic antioxidant capacities of common foods in the United States," *J Agr Food Chem*, vol. 52, pp. 4026–4037, Jun 2004.

[269] Wu, X., Liu, H., Liu, J., Haley, K., Treadway, J., Larson, J., Ge, N., Peale, F., and Bruchez, M., "Immunofluorescent labeling of cancer marker Her2 and other cellular targets with semiconductor quantum dots," *Nat Biotechnol*, vol. 21, pp. 41–46, Jan 2003.

[270] Xie, R. and Peng, X., "Synthesis of Cu-doped InP nanocrystals (d-dots) with ZnSe diffusion barrier as efficient and color-tunable NIR emitters," *J Am Chem Soc*, vol. 131, pp. 10645–10651, Jul 2009.

[271] Xing, Y., Chaudry, Q., Shen, C., Kong, K. Y., Zhau, H. E., Chung, L. W., Petros, J. A., O'Regan, R. M., Yezhelyev, M. V., Simons, J. W., Wang, M. D., and Nie, S., "Bioconjugated quantum dots for multiplexed and quantitative immunohistochemistry," *Nat Protoc*, vol. 2, pp. 1152–1165, Jan 2007.

[272] Yamashita, S., Tokuishi, K., Anami, K., Miyawaki, M., Moroga, T., Kamei, M., Suehiro, S., Ono, K., Takeno, S., Chujo, M., Yamamoto, S., and Kawahara, K., "Video-assisted thoracoscopic indocyanine green fluorescence imaging system shows sentinel lymph nodes in non-small-cell lung cancer," *J Thorac Cardiovasc Surg*, vol. 141, pp. 141–144, Jan 2011.

[273] Yan, Y., Wang, S., Liu, Z., Wang, H., and Huang, D., "CdSe-ZnS quantum dots for selective and sensitive detection and quantification of hypochlorite," *Anal Chem*, vol. 82, pp. 9775–9981, Dec 2010.

[274] Yang, V. W., "APC as a checkpoint gene: The beginning or the end?," *Gastroenterology*, vol. 123, no. 3, p. 935, 2002.

[275] Yeh, S., Lin, H. K., Kang, H. Y., Thin, T. H., Lin, M. F., and Chang, C., "From Her2/neu signal cascade to androgen receptor and its coactivators: a novel pathway by induction of androgen target genes through map kinase in prostate cancer cells," *Proc Natl Acad Sci USA*, vol. 96, pp. 5458–5463, May 1999.

[276] Yuan, F., Dellian, M., Fukumura, D., Leunig, M., Berk, D. A., Torchilin, V. P., and Jain, R. K., "Vascular permeability in a human tumor xenograft: molecular size dependence and cutoff size," *Cancer Res*, vol. 55, pp. 3752–3756, Sep 1995.

[277] Zhang, L., Gu, F. X., Chan, J. M., Wang, A. Z., Langer, R. S., and Farokhzad, O. C., "Nanoparticles in medicine: therapeutic applications and developments," *Clin Pharmacol Ther*, vol. 83, pp. 761–769, May 2008.

[278] Zhang, Y., Chen, W., Zhang, J., Liu, J., Chen, G., and Pope, C., "In vitro and in vivo toxicity of CdTe nanoparticles," *J Nanosci Nanotech*, vol. 7, pp. 497–503, Jan 2007.

[279] Zhang, Y., He, J., Wang, P.-N., Chen, J.-Y., Lu, Z.-J., Lu, D.-R., Guo, J., Wang, C.-C., and Yang, W.-L., "Time-dependent photoluminescence blue shift of the quantum dots in living cells: Effect of oxidation by singlet oxygen," *J Am Chem Soc*, vol. 128, pp. 13396–13401, Jan 2006.

[280] Zhao, W., Hisamuddin, I. M., Nandan, M. O., Babbin, B. A., Lamb, N. E., and Yang, V. W., "Identification of Krüppel-like factor 4 as a potential tumor suppressor gene in colorectal cancer," *Oncogene*, vol. 23, pp. 395–402, Jan 2004.

[281] Zhu, Y., Terry, N. G., Woosley, J. T., Shaheen, N. J., and Wax, A., "Design and validation of an angle-resolved low-coherence interferometry fiber probe for in vivo clinical measurements of depth-resolved nuclear morphology," *J. Biomed. Opt.*, vol. 16, p. 011003, Jan 2011.

[282] Zolnik, B. S., Gonzalez-Fernandez, A., Sadrieh, N., and Dobrovolskaia, M. A., "Minireview: Nanoparticles and the immune system," *Endocrinology*, vol. 151, pp. 458–465, Feb 2010.

[283] Zorn, G. L. and Nesbitt, J. C., "Surgical management of early stage lung cancer," *Semin Surg Oncol*, vol. 18, pp. 124–136, Mar 2000.

VITA

Michael Christopher Mancini was born on April 19th, 1983 at the Portsmouth Naval Hospital in Portsmouth, Virginia. He is the son of David Mancini, a biology teacher, and Pamela Mancini, a pediatrician. Michael's interest in the sciences and engineering began at an early age, inspired by his parents. He received his bachelor of science, with distinction, in 2005 from the University of Rochester in Rochester, New York. Michael's experiences at Rochester working as an undergraduate research assistant convinced him to pursue a Ph.D in the biomedical engineering program at Georgia Tech and Emory University.